UNIVERSIDADE DE SÃO PAULO
ESCOLA DE ENGENHARIA DE LORENA

ANTONIO LUCAS RIGOTTI MANESCO

# Correlations and topology in hybrid graphene-based devices

Lorena

2021

ANTONIO LUCAS RIGOTTI MANESCO

# Correlations and topology in hybrid graphene-based devices

Thesis presented to the Escola de Engenharia de Lorena at the University of São Paulo to obtain the title of Doctor of Science in the Materials Engineering Graduate Program.

Supervisor: Prof. Dr. Durval Rodrigues Jr.
Cosupervisor: Profa. Dra. Gabrielle Weber

Corrected Version

Lorena

2021

Ficha catalográfica elaborada pelo Sistema Automatizado
da Escola de Engenharia de Lorena,
com os dados fornecidos pelo(a) autor(a)

Manesco, Antonio Lucas Rigotti
Correlations and topology in hybrid graphene based devices / Antonio Lucas Rigotti Manesco; orientador Durval Rodrigues Jr. ; co-orientadora Gabrielle Weber - Versão Corrigida. - Lorena, 2021.
146 p.

Tese (Doutorado em Ciências - Programa de Pós Graduação em Engenharia de Materiais na Área de Materiais Convencionais e Avançados) - Escola de Engenharia de Lorena da Universidade de São Paulo. 2021

1. Grafeno. 2. Correlações eletrônicas. 3. Fases topológicas. 4. Supercondutividade. 5. Reflexões de andreev. I. Título. II. Rodrigues Jr. , Durval, orient. III. Weber, Gabrielle, co-orient.

*To my family.*

# Acknowledgements

I excuse myself to write the next paragraphs below in Portuguese. I thank people from abroad in the last two paragraphs.

*Primeiramente, preciso agradecer à minha família. Sem o amparo dessas pessoas, a jornada que culmina na escrita da presente tese teria sido muito mais difícil, senão impossível. Adianto, inclusive, que o agradecimento que segue certamente é muito aquém do merecido. Aos meus pais, Solange e Wlamir, agradeço por tentar sempre me dar as melhores condições possíveis para que eu fosse capaz de alcançar meus sonhos. Muito além do esforço para me darem uma boa educação, também foram essenciais para a minha formação pessoal. Também agradeço a minha esposa, Marília. Essa companheira que atravessou o Atlântico comigo é o porto seguro que precisava para me manter tranquilo e alegre durante o doutoramento. Ainda preciso deixar aqui um agradecimento especial por assumir várias responsabilidades da nossa vida pessoal para que eu pudesse focar totalmente na escrita dessa tese. Não posso deixar de agradecer ao meu irmão, Felipe. A nossa amizade transcende distâncias e compromissos do dia-a-dia. Não há nada que substitua a diversão de tomar uma cerveja com você. Agradeço também aos parentes um pouco mais distantes, mas que foram essenciais na minha formação, em especial, à minha avó Osnira, e (*in memoriam*), aos meus avós Emília, Antônio e Irineu. Por fim, deixo meus agradecimentos à família "postiça". Em especial, meus sogros: Fátima e Valdair; e meus cunhados: Cecília, Amanda, e Leonardo.*

*Naturalmente, preciso agradecer a duas pessoas sem as quais eu não teria nem começado a fazer um doutorado. À Profa. Gabrielle Weber, que começou como uma amiga que acompanhava nos cafés de fim de tarde no Malerba, e que com o passar do tempo se tornou uma grande colega de trabalho. As suas infindáveis atenção e dedicação foram inspiradoras. Ao Prof. Durval Rodrigues Jr., que tem sido um mentor praticamente desde que coloquei os pés na Universidade de São Paulo. Me ensinou a enfrentar a burocracia da academia e me deu liberdade para me desenvolver como um cientista. Também deixo um agradecimento às respectivas famílias.*

*Obviamente, existem várias outras pessoas importantes cujo convívio foi intermediado pela universidade. Além do conhecimento de sala de aula, tomar cerveja com o Luiz Eleno, com o Carlos Alberto (Sustão), e com o Jefferson me ajudou a derrubar aquela barreira mental que criamos entre nós e os professores. Jogar basquete com o Fábio e com o Eduardo Triboni, além de me fazer me sentir jovem, se tornou a grande diversão dos finais de semana. Compartilhar o almoço com os colegas da pós-graduação [Pérsio, Felipe (Bom-Bril), Diego, Ohana, Bianca, e Tamires] fazia a gente perceber que não estávamos*

*sozinhos.*

*Finalmente, como diriam os* Beatles*: "I get by with a little help from my friends". Começo agradecendo à Ana, que, não importa o tempo e a distância, sempre faz parecer que nunca passamos mais de uma semana sem conversar. Com o final do meu doutorado, também finda a minha jornada na cidade de Lorena. Logo, nada mais justo do que agradecer meus colegas de república e os agregados (Carlos, Luciano, Murilo, Schweiger, Pedro, Victor, e Thiago) por fazer o impossível: tornar Lorena agradável. Também agradeço a dois personagens que não foram parte da república, mas com quem compartilhei a jornada da dependência por cafeína: Eduardo e Arthur (para ser justo, o Murilo, o Paulo, e o Ian também devem ser incluídos aqui). Discutir com o Pedro sobre o que tinha de novo no arXiv, ao mesmo tempo que percebíamos os buracos que tínhamos que tapar na nossa formação tornou o processo muito menos solitário. Durante o começo do meu doutorado, também convivi com pessoas maravilhosas, que conheci pela amizade quase de irmãos com a minha esposa: Ronei, Larissa, Tiago, Ananda, e Diogo. Não podia deixar de manifestar aqui os meus agradecimentos a quem abria a casa toda semana, seja para ensaios da banda, comilanças, bebedeiras, ou simplesmente pra acender uma fogueira: Eduardo Triboni. No meio dessas bagunças, conheci a Thaísa e o Marcos – companheiros de viagens e de ficar sentado sem fazer nada.*

*Me desculpo se esqueci de alguém importante. Mas minha cabeça já não está no ápice do funcionamento, agora que finalizo a escrita da tese.*

Now I continue in English.

First, I cannot thank enough Prof. Anton Akhmerov and Prof. Michael Wimmer for the amazing opportunity of working with you during my internship. I never imagined that I could learn so much in a single year, and that is all your fault: the research environment that I experienced while in Delft is something that I hope I can provide to my future pupils. I also thank all the members of the Quantum Tinkerer group for helpful discussions and all the fun. I cannot forget to acknowledge Prof. Jose Lado, with whom I had the opportunity to learn and collaborate.

I finally thank the Leeghwaterstraat gang for making the pandemic a little less unpleasant. Kostas, Alejandra, Felipe, Diana, and Victor: hope to see y'all again soon!

I ackowledge the São Paulo Research Foundation (FAPESP) by funding this work through grants #2016/10167-8 (Honors Doctorate fellowship) and #2019/07082-9 (Research Internships Abroad - BEPE). I have nothing but respect for FAPESP's strength and resistance during the ongoing dismantling of the Brazilian scientific system.

*And I knew exactly what to do. But in a much more real sense, I had no idea what to do.*
Michael Scott, The Office

# RESUMO

MANESCO, A. L. R. **Correlações e topologia em dispositivos híbridos baseados em grafeno**. 2021. 146 p. Tese (Doutorado em Ciências) - Escola de Engenharia de Lorena, Universidade de São Paulo, Lorena, 2021.

Grafeno é um alotropo do carbono bidimensional com uma estrutura cristalina favo-de-mel em que as excitações eletrônicas se comportam como partículas de Dirac sem massa. A ausência de uma massa efetiva faz do grafeno um material sem *gap* e resulta em propriedades eletrônicas excepcionais. Trabalhos paradigmáticos, como os modelos de Haldane e de Kane-Mele, mostram que certos termos de massa levam a fases topologicamente não-triviais em materiais favo-de-mel. Contudo, tais massas são inexistentes ou desprezíveis em folhas de grafeno isoladas. Nessa tese, nós seguimos outra abordagem: nós investigamos fases topológicas em grafeno resultantes de correlações eletrônicas.

Na primeira parte, nós exploramos a emergência de modos de Majorana com energia zero quando supercondutividade é induzida por efeito de proximidade nos estados de borda com antiferromagnetismo não-colinear. Nós derivamos uma teoria de baixas energias para os estados de Majorana combinando condições de contorno de reflexões normais e de Andreev. A natureza de duas bandas desse sistema nos motivou a extender a classificação de de supercondutores topológicos unidimensionais para sistemas multibandas. Nós finalmente investigamos experimentos no estado-da-arte em grafeno no estado Hall quântico em proximidade com um supercondutor e exploramos os possíveis mecanismospara a propagação de estados de Andreev na interface normal/supercondutor. Nossos resultados mostram que a interferência de estados de Andreev recentemente reportada ocorre por disordem na interface. Além disso, nós apontamos melhoras necessárias para alcançar o regime topológico.

A segunda parte dessa tese é dedicada ao estudo de correlações eletrônicas em superedes de grafeno flambadas. A flambagem acontece por conta da relaxação da estrutura resultante da aplicação de tensão no plano do material. Por uma perspectiva de baixas energias, elétrons "sentem" a aplicação de um campo pseudo-magnético. Esse campo leva a formação de níveis de pseudo-Landau, levando a uma diminuição da largura de banda e aumento da densidade de estados no ponto de neutralidade de carga. Com isso, as interações elétron-elétron aumentam, e fases correlacionadas aparecem. Nós provamos, usando o modelo de Hubbard, a existência de ferrimagnetismo modulado numa superrede e mostramos o controle elétrico das correlações eletrônicas. Ademais, nós desenvolvemos uma teoria de baixas energias para esse sistema e exploramos os efeitos de interações de longo alcance, mostrando uma fase *charge density wave* concorrente. Finalmente, nós mostramos que as

duas fases correlacionadas apresentam regimes de isolante Hall quântico de vale, propondo superredes flambadas de grafeno como plataformas para topologia de vale resultante de correlações eletrônicas.

**Palavras-chave**: grafeno. correlações eletrônicas. fases topológicas. supercondutividade. reflexões de Andreev.

# ABSTRACT

MANESCO, A. L. R. **Correlations and topology in hybrid graphene-based devices**. 2020. 146 p. Thesis (Doctor of Science). Escola de Engenharia de Lorena, Universidade de São Paulo, Lorena, 2021.

Graphene is a two-dimensional carbon allotrope with a honeycomb crystal structure in which electronic excitations behave as massless Dirac particles. The absence of an effective mass makes graphene a gapless material with outstanding electronic properties. Paradigmatic works, such as Haldane and Kane-Mele models, show that certain mass terms in honeycomb materials lead to topologically non-trivial phases. However this masses are inexistent or nearly negligible in free-standing graphene. In this thesis, we follow a different approach: we investigate topological phases in graphene driven by electronic correations.

In the first part, we explore the emergence of Majorana zero modes when superconductivity is induced by proximity effect at the canted-antiferromagnetic quantum Hall edge states. We derive a low-energy theory for the Majorana end states combining bundary conditions for normal and Andreev reflections. The two-band nature of this system motivated us to extend the classification of one-dimensional topological superconductors to multiband systems. We finally investigate the current status of state-of-art experiments on proximitized quantum Hall graphene and explore possible mechanisms for the propagation of Andreev edge states at the normal/superconductor interface. Or results show that the recently reported interference of chiral Andreev edge states is due to disorder at the interface. Furthermore, we point out necessary improvements to achieve the topological regime.

The second part of this thesis is devoted to study electronic correlations in buckled graphene superlattices reported in a recent experiment. The buckling transition occurs when the structure relaxes under in-plane strain. From the low-energy perspective, electrons experience strain similarly to a pseudo-magnetic field. This field leads to the formation of pseudo-Landau levels, resulting in a bandwidth quench and an increase of the density of states at half-filling. Thus, the effects of electron-electron interactions are enhanced, and correlated phases take place. We prove the existence of a modulated ferrimagnetic superlattice from Hubbard calculations and show the possibility of electric tunability of correlations. Moreover, we develop a low-energy theory for this system and explore the effects of long-range interactions, showing the existance of a competing charge density wave phase. Finally, we show that both correlated phases present quantum valley Hall insulator regimes, proposing buckled graphene superlattices as a platform for correlation-driven valley topology.

**Keywords**: graphene. electronic correlations. topological phases. superconductivity. Andreev reflections.

# List of Figures

# List of abbreviations and acronyms

| | |
|---|---|
| 2D | — *two-dimensional* |
| TMDs | — *transition metal dichalcogenides* |
| BCS | — *Bardeen-Cooper-Schriffer* |
| QH | — *quantum Hall* |
| AF | — *antiferromagnetic* |
| CDW | — *charge density wave* |
| CAF | — *canted antiferromagnet* |
| QHCAF | — *quantum Hall/canted antiferromagnet* |
| NS | — *normal/superconductor* |
| KM | — *Kane-Mele* |

# List of symbols

| | |
|---|---|
| $K^{(\prime)}$ | Graphene valleys |
| $G_{NS}$ | Andreev conductance |
| $h$ | Plack's constant |
| $e$ | Electron charge |
| $k$ | Lattice momentum |
| $t$ | Hopping constant |
| $\mu$ | Chemical potential |
| $E_F$ | Fermi energy |
| $\Delta$ | Superconducting order parameter |
| $\sigma_H$ | Hall conductance |
| $\mathcal{T}$ | Time-reversal operator |
| $\mathcal{K}$ | Complex conjugation operator |
| $G_{xx}$ | Downstream conductance |
| $B$ | magnetic or pseudo-magnetic field |
| $\sigma_i$ | Pauli matrices |
| $\tau_i$ | Pauli matrices |
| $s_i$ | Pauli matrices |
| $\rho_i$ | Pauli matrices |

# Contents

# 1 Preface

*When we get to the very, very small world – say circuits of seven atoms – we have a lot of new things that would happen that represent completely new opportunities for design. Atoms on a small scale behave like nothing on a large scale, for they satisfy the laws of quantum mechanics. So, as we go down and fiddle around with the atoms down there, we are working with different laws, and we can expect to do different things. We can manufacture in different ways. We can use, not just circuits, but some system involving the quantized energy levels, or the interactions of quantized spins, etc.*

Richard Philips Feynman

The development of Quantum Mechanics and, more specifically, Solid State Physics, was key to the development of today's technology. Substitution of thermionic tubes and valves by transistors proposed less than 100 years ago[1] made it possible to miniaturize computers up to a point that we can now carry them in our pockets.

The intensively growing technology involved in the fabrication of electronic devices resulted on the observation of an exponential growth of transistors density on computers, known as the Moore's law.[2] The resulting comercial run to keep the law pushed the innovations on miniaturization. Eventually, however, a change of paradigm will be necessary to keep this process going.[3]

Since the first report on the fabrication of graphene devices,[4] the growing field of two-dimensional (2D) materials[5,6] appeared as an alternative way to fabricate electronic devices. Nowadays, the electronic industry rely on top-down techniques. However, the manufacture of 2D devices requires a bottom-up approach, which will definitely impact the miniaturization of electronic devices.

2D materials have since then attracted an extensive interest which cannot be solely credited to advancing the miniaturization of electronic devices, but also to the emergence of new physical phenomena and its possible implications on information processing. Graphene and transition metal dichalcogenides (TMDs) have been shown to be platforms for both valleytronics and spintronics.[7–9] Twisted multilayer 2D materials lead to the field of Moiré physics, showing realizations of electronic correlations and topological phases beyond single-layer free-standing approximation.[10–14] Finally, strain engineering has also been proposed as a promising route for studying correlated and topological matter.[15,16]

There are, however, several limits to the miniaturization.[17,18] A representative example is the dificulty to fabricate smaller transistor channels. Shrinking the size of a

transistor requires decreasing the distance between the source and the drain channels. Since tunneling probability increases exponentially as the distance decreases, off-current becomes increasingly larger, resulting on larger off-state power consumption and a reduction of gate control. Also, heating due to Joule dissipation increases as the volume/surface ratio decreases. Thermal heating also spoils the binary signal discrimination. It is also challenging to develop gate structures capable of creating well-defined electrostatic barriers. These are just a fraction of challenges regarding the miniaturization of electronic devices. The difficulties to keep Moore's law inspired a new computing paradigms, such as spintronics, valleytronics, and quantum computation.

A fundamental problem to build universal quantum computers is decoherence.[19] The amount of errors increase as qubits loose information to the environment. Despite the recent claims on quantum advantage by Google,[20] error correction is still a major challenge and the next milestone in quantum computing.[21]

Another possible solution is to rely on approaches that are inherently free of decoherence such as topological quantum computing.[22] In these systems, discrete symmetries make it impossible to destroy the quantum states with small perturbations.[23,22] Possible platforms for topological quantum computation are provided by systems that host Majorana zero modes.[24,25] These quasiparticles are zero energy excitations in topological superconductors.[26,27] Moreover, the solid state realizations of these quasiparticles are non-abelian anyons, allowing the implementation of logic gates with quasiparticle exchange.[22]

A key problem, however, is that there are no conclusive evidences that Majorana zero modes were already observed in experiments yet. Most experiments so far focus on the observation of the zero bias conductance peak in semiconductor nanowires.[28–35] However, there are multiple phenomena that also lead to a similar zero bias feature, such as weak antilocalization, Kondo effect, and zero-energy Andreev states.[36–39] Therefore, there are no smoking gun evidences of an experimental realization of Majorana physics. Even experiments showing large quantized zero-bias peaks are inconclusive, because it shows a necessary but not sufficient condition to probe.[40] The need to find sufficient conditions motivates the next steps experimental efforts must focus on, *e.g.*, peak-to-dip transition, non-local gate effect, correlation in three-terminal devices, local density of states in T-shape devices, Majorana-Fu teleportation, and topological Kondo effect.[41]

In this thesis, we investigate recent experiments with graphene-based devices.[42,15] We review the emergence of Majorana quasiparticles in quantum Hall graphene combined with a superconducting material.[43,44] To establish a bridge between the theory and experiments, we investigate the chiral Andreev edge states interference in a recent experiment.[42] Our theory suggests that disorder-induced intervalley scattering is the main cause of interference in the experiments.[45] The results also point to future directions on

experiments with similar devices. Second, we study the electronic properties of tunable strained graphene superlattices.[15] The bandwidth quench caused by periodic strain fields enhance Coulomb interactions, therefore leading to spontaneous symmetry breakings.[15,16] We further show that correlations lead to valley topology and make predictions about the system's response to external electric and magnetic fields.

# 2 Thesis organization

*"Ford!" he said, "there's an infinite number of monkeys outside who want to talk to us about this script for Hamlet they've worked out."*

Douglas Adams, The Hitchhiker's Guide to the Galaxy

Our main goal in this thesis is to shed some light on recent experimental results on graphene heterostructures. From Chapter 3 to 6 we set the theoretical minimum for the coming chapters containing the main results. The Part I (chapters 7 to 9) is devoted to studying induced superconductivity on quantum Hall edge states. In Part II (chapters 10 to 11), we investigate the electronic properties of buckled graphene superlattices.

Part I is motivated by recent experiments reporting the effort to induce superconducting correlations on quantum Hall edge states.[46,42,47] One of the main motivations is the possibility of creating Majorana zero modes.[43] A key ingredient for topological superconductivity in this system is the canted-antiferromagnetism in the edge states of the lowest Landau level.[48–52] In Chapter 7, we review the theory of Majorana zero modes in graphene and develop an effective model for the boundaries of quantum Hall graphene with a superconductor. We then proceed to review the topological classification of this one-dimensional system in Chapter 8. We end Part I investigating the origin of chiral Andreev edge states interference in a recent experiment[42] and discuss the implications on the topological phase on Chapter 9.

A route to fabricate high-quality graphene-superconductor interfaces is to stack graphene with other van der Waals materials. Recently, it was shown that ridges created with the tip of a scanning tunneling microscope create strong in-plane strain that leads to the formation of buckled graphene superlattices,[15] that we investigate in Part II. The large superlattice period ($\approx 14\,\mathrm{nm}$) results on nearly flat bands, favoring electronic interactions and leading to the formation of an electrically tunable magnetic superlattice,[16] as we show in Chapter 10. In Chapter 11, we show that long-range interactions leat to a charge density wave phase competing with the magnetic ordering. We further reveal quantum valley Hall phases for both groundstates.

# 3 Graphene physics

*The concept of graphene came along in 1947, but nobody paid much attention to it. I was fascinated because it had a linear E versus k while everything else that people were working on at that time had a quadratic dispersion relationship. I wondered why this was and what was so special about it. That was my fascination.*

Mildred Dresselhaus

## 3.1 Electronic structure and massless Dirac carriers

Graphene is a single-atom-thick carbon allotrope. The atoms are organized on a honeycomb crystal structure, allowed by the $sp^2$ hybridization of electronic orbitals.[53,54] This structure is not a Bravais lattice, but a superposition of two triangular lattices,[55] that we will from now on call sublattices $A$ and $B$. The lattice is spanned by the translational vectors:[54]

$$\mathbf{a}_1 = \frac{a\sqrt{3}}{2}\left(\sqrt{3},\ 1\right) \ , \quad \mathbf{a}_2 = \frac{a\sqrt{3}}{2}\left(\sqrt{3},\ -1\right), \tag{3.1}$$

where $a$ is the lattice constant. The graphene lattice is depicted in Fig. 1 (a). The reciprocal lattice is spanned by the vectors:

$$\mathbf{b}_1 = \frac{2\pi}{3a}\left(1,\ \sqrt{3}\right) \ , \quad \mathbf{b}_2 = \frac{2\pi}{3a}\left(1,\ -\sqrt{3}\right). \tag{3.2}$$

However, it is more convenient to describe the hexagonal Brillouin zone, see Fig. 1 (b), in terms of its nonequivalent vertices at

$$\mathbf{K} = \frac{2\pi}{3a}\left(1,\ \frac{1}{\sqrt{3}}\right) \ , \quad \mathbf{K}' = \frac{2\pi}{3a}\left(1,\ -\frac{1}{\sqrt{3}}\right), \tag{3.3}$$

which will play an essential role in the electronic properties of graphene.

Noting that a system that is made of two identical sublattices is inversion symmetric, and that each carbon atom has three nearest neighbors in the opposite sublattice, the simplest Hamiltonian we can write to describe electrons in graphene is of the following form:[26]

$$\mathcal{H} = \sum_k \begin{pmatrix} c_{Ak}^\dagger & c_{Bk}^\dagger \end{pmatrix} \begin{pmatrix} 0 & h(\mathbf{k}) \\ h(\mathbf{k})^\dagger & 0 \end{pmatrix} \begin{pmatrix} c_{Ak} \\ c_{Bk} \end{pmatrix} \ , \quad h(\mathbf{k}) = -\sum_{i=1}^{3} t_i e^{i\mathbf{k}\cdot\boldsymbol{\delta}_i}. \tag{3.4}$$

Here, $c_{Ak}$ and $c_{Bk}$ denote the annihilation operators of electrons with crystal momentum $\mathbf{k}$ in the sublattice A and B, respectively. The nearest neighbors vectors, see Fig. 1 (a), are:

$$\boldsymbol{\delta}_1 = \frac{a}{2}\left(1, \sqrt{3}\right) \ , \quad \boldsymbol{\delta}_2 = \frac{a}{2}\left(1, -\sqrt{3}\right) \ , \quad \boldsymbol{\delta}_3 = a\left(-1, 0\right). \tag{3.5}$$

Figure 1 – (a) Scheme of graphene's honeycomb crystal structure. The structure consists of a triangular lattice with two sublattices distinguished by the colors red (A) and blue (B). The crystal structure is spanned by the vectors $\mathbf{a}_1$ an $\mathbf{a}_2$. The zigzag and armchair terminations are indicated by arrows. (b) Graphene's first Brillouin zone. We indicate the high-symmetry points $\Gamma$, $K$, $K'$, and $M$ and, in red, the path in the Brillouin zone often used on bandstructure calculations along the text.

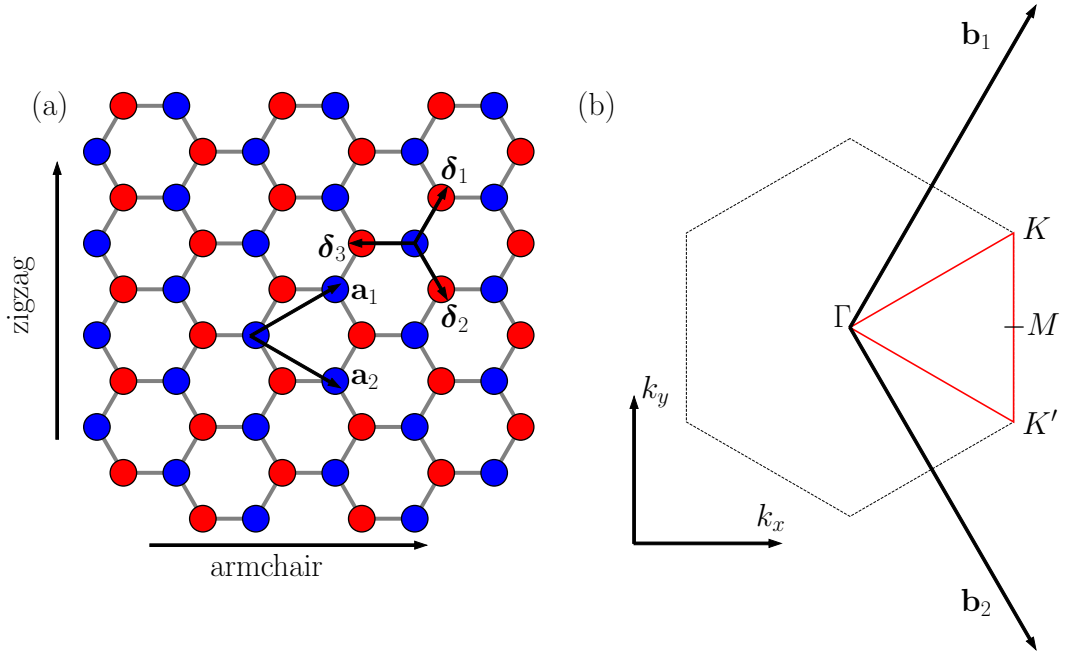


Source: author.

The constants $t_i$, $i = 1, 2, 3$, are the nearest-neighbors hopping energies. In a perfect graphene lattice, crystal symmetry ensures they are all equal, $t_i = t$. It is worth emphasizing that this approximation holds at the vincinity of the Fermi level, but away from it second-nearest neighbor hoopings break the particle-hole symmetry.

The spectrum of Eq. 3.4 is shown in Fig. 2 (a). We see that $h(\mathbf{k})$ vanishes exactly at the points $K$ and $K'$, with an approximate linear dispersion in the vincinity of these points, as shown inf Fig. 2 (b). Thus, we obtain a low-energy theory by expanding the Hamiltonian up to the first-order on $\mathbf{p} = \mathbf{k} - \mathbf{K}^{(\prime)}$:[54,26]

$$\mathcal{H} = \psi_k^\dagger \left(\rho_0 v \otimes \mathbf{p} \cdot \boldsymbol{\sigma}\right) \psi_k, \tag{3.6}$$

in the valley-symmetric representation $\psi = (c_{Ak+}, c_{Bk+}, c_{Bk-}, c_{Ak-})^T$.[56] The subindices $+$ and $-$ indicate the valleys $K$ and $K'$, respectively. We introduced two sets of Pauli matrices $\rho$ and $\sigma$ that act on valley and sublattice spaces, respectively.[a] The Hamiltonian in Eq. 3.6 corresponds to the massless two-dimensional version of the Dirac equation in two

[a] The Pauli matrices are assumed to be in the usual representation and the index 0 corresponds to the two-dimensional identity matrix.

Figure 2 – (a) Spectrum of graphene's tight-binding Hamiltonian in Eq. 3.4. The valence (blue) and conduction (orange) bands touch exactly at the points $K$ and $K'$. (b) Zoom at one of the points where the valence and conduction bands touch, showing a linear dispersion corresponding to the spectrum of the Hamiltonian in Eq. 3.6. Bandstructure of a nanoribbon terminated along the (c) zigzag (c) and (d) armchair direction. The Landau levels in graphene when subjected to an out-of-plane magnetic field. (f) Quantum Hall edge states of a nanoribbon along the zigzag direction. The valley polarization $\mathcal{V}$ shows that opposite edges have opposite valley polarization.

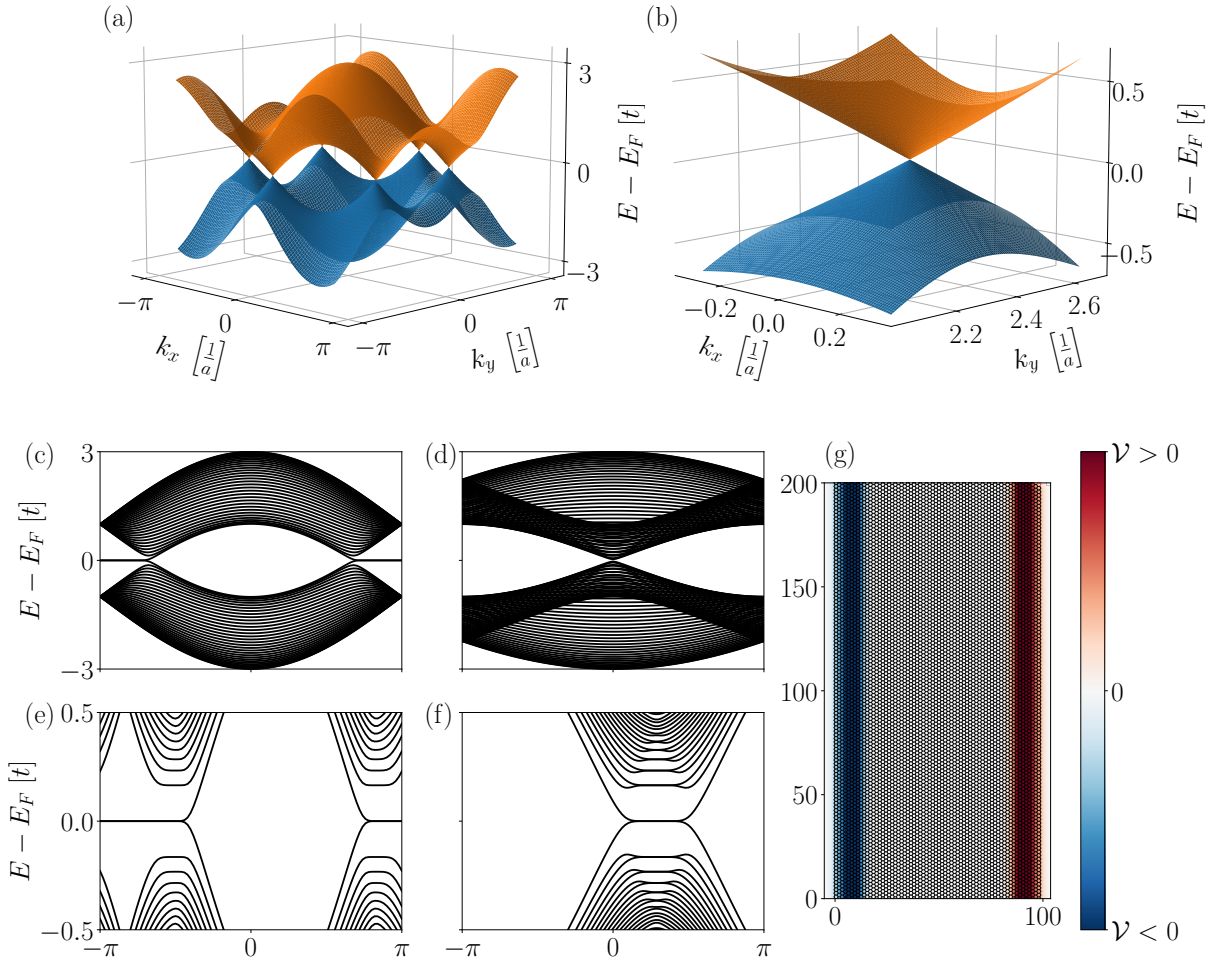


Source: author.

dimensions. Since the points $K$ and $K'$ are mapped into each other by both inversion and time-reversal symmetry, there are two-fold degenerate symmetry-protected Dirac cones at both valleys.

So far, however, we have only considered infinite graphene systems. In finite-size devices, edge states play a significant role. In Fig. 1 (a) we show two most important types of termination: zigzag and armchair. The corresponding bandstructures of nanoribbons with each termination can be seen in Fig. 2 (c, d). Interestingly, it turns out that the

wavefunctions of any terminated graphene lattice are limited to zigzag or armchair boundary conditions.[57,58] While armchair boundary conditions hold for boundaries oriented within angles $\lesssim 0.1$, zigzag boundary conditions hold for *all* other orientations.[58] The reason is that, along zigzag terminations, valleys have a large separation in momentum space. Thus, valley number is approximately conserved if disorder is smooth, since elastic scattering between the two valleys require scattering centers with sizes close to the lattice constant.

## 3.2 Quantum Hall effect

Two-dimensionality, high-electron mobility and low density of states in the vincinity of the Fermi level make graphene a great platform for mesoscopic physics.[4,54] For example, it was shown in graphene early days that quantum Hall effect is accessible even at room temperature.[59]

Conventional two-dimensional electron gases with quadratic low-energy band dispersion, when submitted to an out-of-plane magnetic field $B$, experience the formation of Landau levels, enumerated by $n$, with an spectrum of the form:[60–62]

$$E_n = \hbar\omega_c \left(n + \frac{1}{2}\right) \ , \quad n \in \mathbb{N} \tag{3.7}$$

where $\omega_c = eB/m^*$ is the cyclotron frequency and $m^*$ is the effective mass. In graphene, however, the massless Dirac Hamiltonian leads to a spectrum[63,64,59,48]

$$E_n = \mathrm{sgn}\,(n) v\sqrt{2e\hbar B|n|} \ , \quad n \in \mathbb{Z} \tag{3.8}$$

meaning that the lowest Landau level lies at the Fermi energy ($E_0 = 0$). The spectra for zigzag and armchair nanoribbons under the quantum Hall regime is shown in Fig. 2 (e, f).

Under a confining potential, the Landau levels disperse, forming a series of edge states. The breaking of time-reversal symmetry by the out-of-plane magnetic field ensures that opposite edges have edge states with opposite chirality. Thus, as long as the edges are well-separated, these chiral modes cannot backscatter. Following the Landauer-Buttiker formalism, the total Hall conductance is then expected to be a multiple of the conductance quantum:[65]

$$G = n\frac{e^2}{h} \ , \quad n \in \mathbb{Z}, \tag{3.9}$$

where $n$ denotes the number of edge states. We discuss in chapter 5 the topological origin of $n$, providing an alternative explanation for the robustness of edge states propagation.

Electrons confined in graphene systems experience a sublattice- and valley-dependent potential. As we discussed, at general (zigzag) boundary conditions, valley is a good quantum number.[57,58] Thus, taking into account the sublattice-valley locking of graphene's

lowest Landau level,[48] as shown by Eq. 3.8, we conclude that the quantum Hall edge states are both sublattice and valley polarized,[56] as shown in Fig. 2 (g).

The presence of a Landau level at the Fermi energy leads to a high density of states at charge neutrality, promoting spontaneous symmetry breaking phases, such as charge density wave and canted-antiferromagnetism.[48–52] The latter will be particularly relevant for this thesis, since it is a key phenomena to generate Majorana zero modes in graphene, as we discuss in chapter 7.[43,44]

## 3.3 Strained graphene

By straining a graphene crystal, lattice symmetries are broken. Thus, the nearest-neighbor hoppings are no longer equal, but become modulated by the strain field. Up to the first order, we have:[66]

$$t_i \approx t\left(1 + \frac{\beta}{a^2}\boldsymbol{\delta}_i \cdot \mathbf{u}_i\right), \tag{3.10}$$

where $\mathbf{u}_i$ is the displacement field, and $\beta = -\partial \ln t/\partial \ln a \approx 2$ is the Grüneisen parameter. The resulting low-energy Hamiltonian corresponds to Eq. 3.6 with an extra term that can be interpreted as a valley-dependent gauge field $\mathbf{A}$:

$$\mathcal{H} = \psi_k^\dagger \left[v\left(\rho_0 \otimes \mathbf{p} - \rho_z \otimes \mathbf{A}\right) \cdot \boldsymbol{\sigma}\right] \psi_k. \tag{3.11}$$

Hence, pseudo-Landau levels can also be observed in strained graphene without the need of applying an out-of-plane magnetic field.[b66]

The valley-dependency, however, leads to different eigenstates: instead of sublattice-valley locking, both valley states at the lowest pseudo-Landau have the same sublattice polarization. Combining it with the zigzag boundary conditions, we conclude that both pseudo-Landau level states propagate along the same edge. They are, thus, unprotected from backscattering. One can understand it as a consequence of preserving time-reversal symmetry in the presence of pseudo-magnetic fields.

It turns out that strained graphene also shows spontaneous symmetry breakings.[67,16] However, the sublattice polarization caused by pseudo-magnetic fields lead to a ferrimagnetic groundstate, instead of the antiferromagnetic groundstate that emerges in usual quantum Hall graphene. We will explore this in more detail in chapter 10.

[b] We use *pseudo* here to distinguish between gauge fields originated from *real* magnetic fields and *pseudo* magnetic fields caused by strain.

# 4 Basics of superconductivity

*Richard Feynman has related that at a meeting of the American Physical Society, likely sometime in 1956, he was chatting with Onsager when a wild-eyed young man came up to them and said that he had solved the problem of superconductivity. ... As Feyman relates, he could not understand what the young man was saying and concluded that the fellow was probably crazy. ... Feynman believed that the young man was me. I am not sure whether or not this meeting actually occurred, but it might have.*

Leon Cooper, Remembrance of Superconductivity Past by Leon N. Cooper

Superconductivity was discovered in 1911 by H. Kamerlingh Onnes while measuring the resistance of mercurium at low temperatures. The first sucessful microscopic theory, however, was published only in 1957 by Bardeen, Cooper, and Schrieffer (known today as the BCS theory).[68,17,69] However, it explains only a limited class of materials, and a complete theory is still a major challenge for the Condensed Matter community.

In large scales, superconducting materials are know to, below a critical temperature $T_c$: (i) carry current without dissipation; (ii) expel the magnetic field from the bulk (Meissner effect). Superconducting materials are classified according to their response to external magnetic fields. A type-I material exponentially suppresses an external field from the boundary to the bulk of the system. However, if the external field is above a critical value $H_c$, superconductivity is destroyed. For type-II materials, on the other hand, there are two critical fields: below $H_{c1}$ the material behaves just as a type-I superconductor; between $H_{c1}$ and $H_{c2}$ the magnetic field penetrates in the bulk as vortex lines. Above $H_{c2}$, the vortex density is too high and superconductivity is destroyed.[68,70]

## 4.1 Cooper pairing and BSC theory

The main asumption of BCS theory is the existence of an attractive interaction that pairs electrons.[69] These are known as Cooper pairs, and, in conventional superconductors, they are mediated by electron-phonon iteractions.[71] The existence of an electron-electron pairing mechanism means that the *pair amplitude*

$$F_{ss'}(\mathbf{r}_i, \mathbf{r}_j) = \langle c_{is} c_{js'} \rangle \tag{4.1}$$

becomes finite. We use $s$ to denote the spin projection along the $z$-axis. In conventional superconductors, the pairing is singlet and the pair amplitude is local: $F_{\uparrow\downarrow}(\mathbf{r}) = F_{\downarrow\uparrow}(\mathbf{r})$.

If we integrate out the phonon field, the electronic Hamiltonian is given by

$$\mathcal{H} = \mathcal{H}_0 + \sum_{i,j,k,l} \sum_{s,s',s_1,s_2} \lambda_{ijkl}^{ss's_1s_2} c_{is}^\dagger c_{js'}^\dagger c_{ks_1} c_{ls_2}, \tag{4.2}$$

where $\lambda_{ijkl}^{ss's_1s_2}$ are the electron-electron coupling constants; and $\mathcal{H}_0$ is the single-particle Hamiltonian, *e.g.*, the graphene Hamiltonian in Eq. 3.4. In the weak electron-electron coupling limit, the fluctuations in $c_{is}^{(\dagger)} c_{js'}^{(\dagger)} - F_{ss'}^{(*)}(\mathbf{r}_i, \mathbf{r}_j)$ are negligible. Thus, we approximate the Hamiltonian to its mean-field version:

$$\mathcal{H} \approx \mathcal{H}_0 + \sum_{i,j} \sum_{s,s'} \left[ \Delta_{ij,ss'} c_{is}^\dagger c_{js'}^\dagger + h.c. \right], \tag{4.3}$$

where we defined the superconducting order parameter

$$\Delta_{ij,ss'} := \sum_{s_1,s_2} \sum_{k,l} \lambda_{ijkl}^{ss's_1s_2} \langle c_{ks_1} c_{ls_2} \rangle. \tag{4.4}$$

In this thesis, we often consider the so-called $s$-wave pairing, which consists in local singlet pairing. Hence, the order parameter is:

$$\Delta_{i,s\bar{s}}^s = \sum_j \Delta_{ij,ss'} \delta_{ij} (i s_y)_{ss'} \tag{4.5}$$

where $\bar{s}$ is the opposite of $s$, and $\delta_{\alpha\beta}$ is the Kronecker delta. We also consider $p$-wave superconductivity, which is a non-local triplet pairing with the form

$$\Delta_{ij,ss'}^p = (\mathbf{d}_{ij} \cdot \mathbf{s}\ i s_y)_{ss'} \tag{4.6}$$

with $i \neq j$ and $\mathbf{d} = (d_1, d_2, d_3)_{ij}$.[72] The Pauli matrices $s_i$ act on spin space.

## 4.2 Bogoliubov-de Gennes Hamiltonian

We now introduce the Nambu spinors $\psi_i = (c_{i\uparrow}, c_{i\downarrow}, -c_{i\downarrow}^\dagger, c_{i\uparrow}^\dagger)^T$, which allow us to write Eq. 4.3 in the compact form:

$$\mathcal{H} = \sum_{ij} \psi_j^\dagger \begin{pmatrix} (H_0)_{ij} & \Delta_{ij,ss'}\mathcal{T} \\ \mathcal{T}\Delta_{ij,ss'}^\dagger & -\mathcal{T}(H_0)_{ij}\mathcal{T} \end{pmatrix} \psi_i \tag{4.7}$$

where the diagonal term

$$\mathcal{H}_0 =: \sum_{ij} \psi_j^\dagger \begin{pmatrix} (H_0)_{ij} & 0 \\ 0 & -\mathcal{T}(H_0)_{ij}\mathcal{T} \end{pmatrix} \psi_i \tag{4.8}$$

is the non-superconducting Hamiltonian, $\mathcal{T} = is_y\mathcal{K}$ is the time-reversal symmetry operator, and $\mathcal{K}$ is the complex conjugation operator. We will often use the Pauli matrices $\tau_i$, acting on electron-hole degrees of freedom, to write the matrix in Eq. 4.7 in a compact form. The matrix in Eq. 4.7 is known as Bogoliubov-de Gennes Hamiltonian.[68,70]

The Hamiltonian in Eq. 4.3 is diagonalizible under a *Bogoliubov transformation*:

$$\psi_i \mapsto \Gamma_i = U_i\psi_i \ , \quad (H_{BdG})_{ij} \mapsto U_j(H_{BdG})_{ij}U_j^\dagger \tag{4.9}$$

where $\Gamma_i = (\gamma_{i\uparrow}, \gamma_{i\downarrow}, -\gamma_{i\downarrow}^\dagger, \gamma_{i\uparrow}^\dagger)^T$. We will come back to this quasi-particle representation when we discuss topological superconductivity in Chapter 5.1.

As an example, let us consider a simple Hamiltonian in momentum representation:

$$H_0(\mathbf{k}) = \frac{\hbar k^2}{2m^*}s_0 \ , \quad \text{and} \quad \Delta_{ss'}(\mathbf{k}) = \Delta(is_y)_{ss'}. \tag{4.10}$$

which is the Hamiltonian of a $s$-wave superconductor with parabolic dispersion. Thus, the matrix in Eq. 4.7 takes the form:

$$H_{BdG}(\mathbf{k}) = \tau_z \otimes \frac{\hbar k^2}{2m^*}s_0 + \tau_1 \otimes \Delta s_0. \tag{4.11}$$

Its spectrum

$$E(\mathbf{k}) = \pm\sqrt{\left(\frac{\hbar k^2}{2m^*}\right)^2 + \Delta^2} \tag{4.12}$$

is shown in Fig. 3 (a). The system, thus, has a gap $|\Delta|$, meaning that there cannot be quasiparticle excitations for energies $E < |\Delta|$. In other words, electrons can only enter the system as Cooper pairs.

## 4.3 Andreev reflection

Consider now a system consisting of a junction between a normal and a superconducting material, as illustrated in Fig. 3 (b). If we inject an electron from the normal region to the superconducting region, it cannot enter the superconductor as a single particle state. Thus, there are two possible situations: (i) the electron is reflected back (normal reflection); (ii) as the electron enters the superconductor, it pairs with another electron. To ensure global charge conservation in (ii), the the second electron state leaves a hole. Effectively, we see the incident electron reflect as a hole. This process is called Andreev reflection. To be more precise and general, an incoming quasiparticle is reflected back as its time-reversal partner.[70,73]

Suppose the superconducting region is grounded. The conductance measured between the normal lead and the grounded superconductor is provided by the BTK

Figure 3 – (a) Energy dispersion of the Bogoliubov-de Gennes Hamiltonian in Eq. 4.12. In the superconducting state $|\Delta| > 0$, there is an energy gap. (b) Representation of an Andreev reflection. An incident electron couples with another electron in the superconducting region and a hole is ejected in the normal region for charge conservation. In experiments, there is usually a barrier separating the normal and the superconducting regions. This barrier can be naturally generated by the fabrication process or created with an electrostatic potential (gate voltage). (c) Andreev conductance of a system similar to the scheme in (b). In the normal state ($|\Delta| = 0$), there are two electron channels, resulting in a conductance $2e^2/h$. In the superconducting state, there are two different regimes: the open regime, in which all electrons are Andreev reflected, and the conductance twice as large as the conductance in the normal state; and the tunneling regime, in which Andreev reflection is supressed by a large barrier potential between the normal and the superconducting regions. The tunneling regime is often used to probe the gap size.

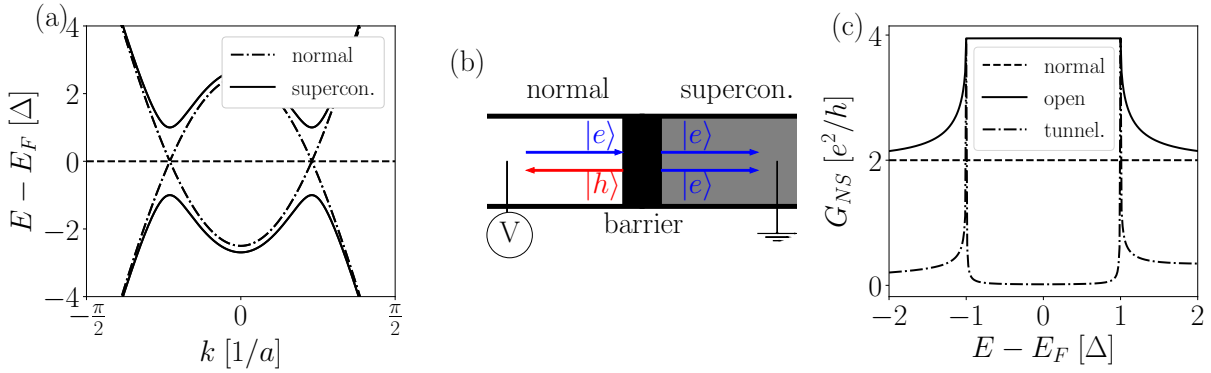


Source: author.

formula:[74]

$$G_{NS} = \frac{e^2}{h}\left(N - R_{ee} + R_{he}\right) \tag{4.13}$$

where $G_{NS}$ is the Andreev conductance, $N$ is the number of electron channels in the normal region, and

$$0 < R_{ee}, R_{he} < N \ , \quad R_{ee} + R_{he} = N, \tag{4.14}$$

are the normal reflection and Andreev reflection coefficients.

The reflection coefficients $R_{ee}$ and $R_{he}$ depend on the normal-superconductor (NS) interface. The device's fabrication produces defects at the interface, creating a barrier, illustrated in Fig. 3 (b). Hence, electrons must propagate through the defect to be Andreev-reflected. Even if there are no defects at the inteface, the competition between normal and Andreev reflections can be controlled by a gate voltage. If electrons feel no scattering potential until they hit the superconductor, $R_{he} = N$, meaning that, within the gap, $G_{NS} = 2Ne^2/h$. This is called the *open regime*. On the other hand, if electrons feel a strong scattering potential before hitting the superconductor, they must tunnel through this scattering region, and Andreev reflection is supressed. This is the tunneling regime,

for which, in the limiting case where Andreev reflection is completely supressed, results in $R_{ee} = N$ and $G_{NS} = 0$. In Fig. 3 (c) we show both the open and the tunneling regimes. It is worth mentioning that, if there is no gate potential at the interface, the Andreev conductance measures the quality of the interface: if the conductance is close to the open regime value, the scattering potential is small. Also, experimentalists often use the peak resonances in the tunneling regime, shown in Fig. 3 (c), to probe the gap size.

# 5 Symmetry protected topological phases

*At this point the power of exact (but not fully understood) mathematical results to sow confusion enters the story!*

Duncan M. Haldane, Nobel Lecture 2016

Here we briefly introduce the concept of topology in condensed matter physics. However, we restrict ourselves to a strict class of systems. Namely, only consider periodic gapped systems in a mean-field level. Thus, for the sake of simplicity, we ignore many-body non-trivial topological orders, as well as gapless and disordered/amorphous systems.

Perhaps the best way to start our discussion is with the canonical joke about topologists: they cannot distinguish between a donut and a mug.[75] To explain the joke, though, lets us start with a simple object, the sphere. One can *smoothly* deform a sphere into a cube, for example. However, since the donut has a handle, it is impossible to continuously deform an sphere into a donut without punctarating it. It is possible, however, to *smoothly* deform a donut into a mug, since they both have one and only one handle. Objects that are *smoothly* connected are called topologically equivalent, and it is often possible to classify them with a number, called topological invariant. In this example, the invariant is the number of handles the object has, a.k.a. the *genus*.[76,22] As a matter of fact, all closed surfaces are topologically equivalent to spheres with some number of handles or crosscaps.[77] Finally, the sphere is usually said to be topologically trivial.[76,22]

First of all, it is important to make it perfectly clear that all periodic gapped systems in a mean-field level have a topological structure. What we then call a *topological* system is actually a topologically non-trivial system. Then, we must define what a topologically trivial system is. Since we are talking about gapped materials, we define as topologically trivial the atomic insulator,[22,26] *i.e.*, the system in which each electron is bounded to a single atom. In even simpler words, it is just a collection of isolated atoms, as depicted in Fig. 4 (a).

Now that we have a definition of what topologically trivial means, we can define what is topologically non-equivalent to it. First, we must fix the system's dimensionality and the set of discrete symmetries obeyed. Then, we say a system is topological (or topologically non-trivial) if there is no smooth map that connects its Hamiltonian with the Hamiltonian of the atomic insulator without closing the system's bulk gap.[22,26] If two non-equivalent regions are connected in space, the gap must close at the boundary. For example, the boundary between a topological system and vacuum has zero-energy edge

Figure 4 – (a) Electron trajectories in an atomic insulator. (b) Electron trajectories in the quantum Hall effect. Differently to an atomic insulator, cyclotron orbits are interrupted and chiral states develop at the system's edges. (c) Helical trajectories in a quantum spin Hall insulator.

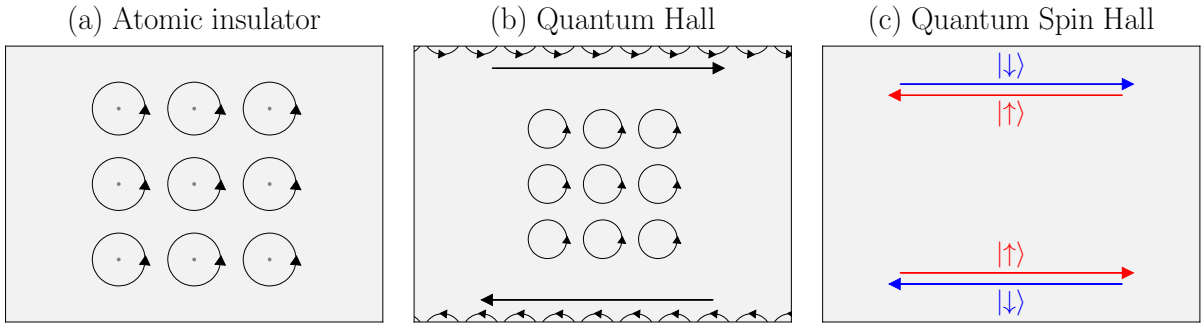


Source: author. Adapted from Nijholt (78).

states, as shown in Fig. 4 (b, c).

Of course, an exhaustive search for all maps that connect two different Hamiltonians is not practical at all. Instead, we check the group structures in the fiber bundle composed by the Brilluin zone (base space), and the Hilbert space (fiber). The presence or absence of time-reversal ($\mathcal{T}$), particle-hole ($\mathcal{C}$), and chiral ($\mathcal{S}$) symmetries for a given dimension restrict the group structures to ten Cartan spaces. This classification is known as the ten-fold way.[79,27,22,27] Once the symmetry class is identified, we then compute the topological invariant and conclude whether or not the system is topologically non-trivial.

## 5.1 Topological superconductivity

The Kitaev chain is the most prominent example of a topological system.[25] We consider a chain of spinless electrons with $N$ sites and denote the creation and annihilation operators acting on the site $n$, $1 \leq n \leq N$ by $c_n^\dagger$ and $c_n$, respectively.

$$c_n^\dagger = \frac{1}{2}(\gamma_n + i\tilde{\gamma}_n) \ , \quad c_n^\dagger = \frac{1}{2}(\gamma_n - i\tilde{\gamma}_n), \tag{5.1}$$

where $\gamma_n$ and $\tilde{\gamma}_n$ are known as Majorana operators, since $\gamma_n = \gamma_n^\dagger$ and $\tilde{\gamma}_n = \tilde{\gamma}_n^\dagger$. For this reason, Majorana particles (and quasi-particles) are known to be their own antiparticles.

We now consider two different Hamiltonians to describe a chain of atoms for which the quasiparticle excitations can be described by Majorana operators. We could, for example, allow onsite interactions both between $\gamma_n$ and $\tilde{\gamma}_n$, leading to

$$H_1 = \frac{i\mu}{2} \sum_{n=1}^{N} \gamma_n \tilde{\gamma}_n. \tag{5.2}$$

Using Eq. 5.1, we find out that we are then describing electrons that cannot move to the neighbor atom. Therefore, it is an atomic insulator [see Fig. 5 (b)]:

$$\mathcal{H}_1 = -\mu \sum_{n=1}^{N} c_n^\dagger c_n. \tag{5.3}$$

We could similarly allow hoppings between Majorana operators in neighbouring positions,

$$\mathcal{H}_2 = it \sum_{n=1}^{N} \gamma_n \tilde{\gamma}_{n+1}. \tag{5.4}$$

It is visible that this Hamiltonian has two zero energy modes at both ends of the chain. We notice that both Hamiltonians from Eqs. 5.4 and 5.2 are special cases of a $p$-wave superconductor:

$$\mathcal{H} = \sum_{n=1}^{N} \left( -\mu c_n^\dagger c_n - t c_{n+1}^\dagger c_n + \Delta c_{n+1}^\dagger c_n^\dagger + h.c \right), \tag{5.5}$$

where $t$ is the hopping constant, $\Delta$ is the superconducting pairing potential, $\mu$ is the chemical potential, and $h.c.$ denotes the hermitian conjugate of all previous terms. Eq. 5.4 is recovered when $\mu = 0$ and $\Delta = t$, while the Eq. 5.2 corresponds to $\Delta = t$. Thus, it is possible to create zero energy Majorana states at the ends of an 1D $p$-wave superconductor.

Figure 5 – (a) Illustration of a chain with $N = 5$. (b) Atomic insulator limit of the Kitaev chain with $t = \Delta = 0$. (c) Topological regime of the Kitaev chain with $\mu = 0$ and $\Delta = t$. (d) Lowest energy wavefunctions of the Kitaev chain with $\mu = 0$ and $\Delta = t$ (blue), $\mu = 1.93t$ and $\Delta = t$ (orange), and $\mu = 1.98t$, $\Delta = 0.2t$ (green).

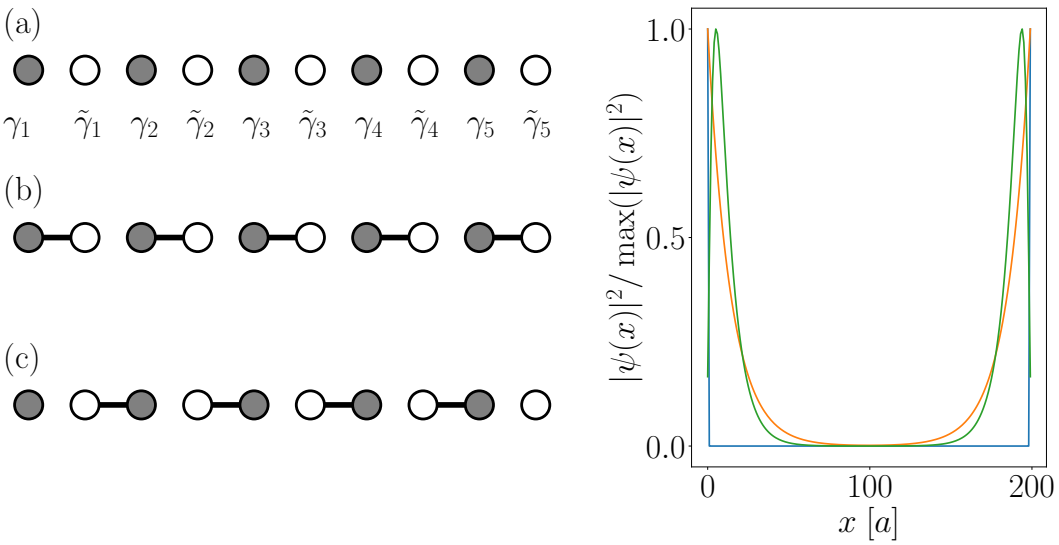


Source: author.

We can further consider whether we really need the conditions $\mu = 0$ and $\Delta = t$ to be exactly satisfied. As a matter of fact, there are well-separated Majorana zero modes

at both ends of the wire, as shown in Fig. 5 (d), for several values of $\mu$, $\Delta$, and $t$. Hence, the existence of Majorana zero modes is much more robust than the aforementioned conditions may have led us to believe. We can verify that Majorana zero modes exist in the regime $|\mu| < 2|t|$. When we close and open it again, we have a system that is topologically equivalent to the atomic insulator described by the Eq. 5.2. The existence of states at the ends of a one-dimensional topological system is often refered to as the *bulk-edge correspondence*.[22,27] The presence or absence of discrete symmetries pin the end states at zero energy, and therefore they are robust to disorder, as long as the bulk gap does not close.

Finally, we do not really need to look at bulk gap or check the presence of zero energy states. Instead, we could simply compute the topological invariant given by:

$$\mathcal{Q} = \operatorname{sgn}\left[\operatorname{Pf}\left(iH(0)\right)\operatorname{Pf}\left(iH(\pi)\right)\right] \tag{5.6}$$

where Pf denotes the Pfaffian, and $H(k)$ is the Hamiltonian of Eq. 5.5 in the Bloch representation. Whenever $\mathcal{Q} = 1$ the system is topologically equivalent to an atomic insulator. When $\mathcal{Q} = -1$, we call it a topological superconductor.

## 5.2 Quantum Hall effect revisited

As previously discussed, the quantum Hall conductance arises due to the propagation of one-dimensional edge states along the boundaries of the system. Breaking a discrete symmetry, such as the time-reversal symmetry, allows the existence of chiral edge states.[65,22,27] Therefore, backscattering is prohibited, and the conductance of quantum Hall systems can be measured with a impressive precision, even in the presence of strong disorder at the boundaries of the system.[62,60] Indeed, this is a manifestation of the bulk-edge correspondence.

In fact, we can compute a topological invariant, called Chern number, given by

$$\mathcal{C} = \sum_{E_n<E_F} \int_{\mathrm{BZ}} \frac{d^2\mathbf{k}}{2\pi} \cdot \boldsymbol{\Omega}_n(\mathbf{k}), \tag{5.7}$$

where the integration is over the Brillouin Zone, $\boldsymbol{\Omega}_n(\mathbf{k}) = \nabla \times \boldsymbol{\mathcal{A}}(\mathbf{k})$ is the so-called Berry curvature, and

$$\boldsymbol{\mathcal{A}}(\mathbf{k}) = i \left\langle \psi_n \right| \partial_{\mathbf{k}} \left| \psi_n \right\rangle \tag{5.8}$$

is the Berry connection.[80] Intuitively, one could interpret the Berry connection as the generator of infinitesimal transformation in the wavefunctions' phase. Therefore, nontrivial topological structures in this fiber bundle results on finite Chern number.

Finally, there is a direct relation between the Chern number and the Hall conductivity,[81]

$$\sigma_H = \frac{e^2}{h}\mathcal{C}. \tag{5.9}$$

Hence, measuring the Hall conductance is a direct way to measure the Chern number in quantum Hall systems. The correspondence between the Chern number and the Hall conductance explains the strong robustness to disorder: since smooth deformations in the Hamiltonian cannot change the Chern number, a change in conductance cannot happen without a topological phase transition. Thus, small perturbations have no effect in the Hall conductance.

## 5.3 Quantum spin Hall insulators

Next, we consider whether it is possible to have topologically protected Hall conductance without an external magnetic field. As we have already discussed, time-reversal symmetry breaking is a necessary condition for having chiral edge states. However, we can combine two copies of a quantum Hall system, related by time-reversal symmetry. In other words, it would consist of a clockwise and a counter-clockwise moving edge states states with opposite spin orientation (helical edge states), as depicted in Fig. 4 (c). This phenomenon is called quantum spin Hall effect.[82,23]

Naturally, if spin-up and spin-down states propagate on opposite directions, the net edge current is zero. However, the spin current

$$\mathbf{J}_s^{\text{edge}} = \mathbf{J}_\uparrow^{\text{edge}} - \mathbf{J}_\downarrow^{\text{edge}} \tag{5.10}$$

is nonzero. Similarly, the Chern number is also zero, but the spin Chern number

$$\mathcal{C}_s = \mathcal{C}_\uparrow - \mathcal{C}_\downarrow \tag{5.11}$$

is finite.[83]

In fact, the first model of a quantum spin Hall insulating phase was proposed to occur in graphene-like (honeycomb) materials and is known today as the Kane-Mele model.[82] The only possible ways to open a gap in graphene without breaking time-reversal symmetry is with the addition of terms proportional to $\sigma_z$ (sublattice imbalance) and $\rho_z \otimes \sigma_z \otimes s_z$ (spin-orbit coupling) to Eq. 3.6. Sublattice imbalance is add at the tight-binding level as an staggered sublattice potential

$$\mathcal{H}_{\text{stagg}} = m \sum_i \sum_{s,\tau} (\sigma_z)_{ii} c_{is\tau}^\dagger c_{is\tau} \tag{5.12}$$

while the spin-orbit coupling term is a consequence of second-nearest-neighbors hoppings

$$\mathcal{H}_{SOC} = i\lambda \sum_s \sum_{\langle\langle i,j \rangle\rangle} (s_z)_{ss} \eta_{ij} c_{is}^\dagger c_{js}$$

where $c_{is}^{\dagger}$ are creation and $c_{is}$ annihilation operators operators at the site $i$, sublattice $\sigma$, spin $s$, and $\eta_{ij} = \pm 1$ for a clockwise/anticlockwise hopping. A topological gap opens if $|m| < |3\sqrt{3}\lambda|$ and is a trivial insulator otherwise.

# 6 Hybrid systems with graphene

*One love, one heart*
*Let's get together and feel all right*

Bob Marley, One Love

The fabrication of high-quality graphene/superconductor interfaces are reported since graphene's early days.[84,85] Nearly transparent normal-superconductor (NS) interfaces were obtained combining graphene with other van der Waals materials[86]. In fact, This motivated several studies involving a variety of techniques such as: as tunneling spectroscopy,[87,88] Josephson effect,[85,89–91] multiple[92] and specular Andreev reflections,[93,94] imaging Andreev scattering,[95] quantum phase transitions,[96,97] reflectionless tunneling,[30] microwave circuits,[98] and bolometer devices.[99] Furthermore, the ease of producing these systems also paved the route to use the material as an ideal platform to combine superconductivity with other quantum phenomena, such as integer and fractional quantum Hall physics.[100,42,47]

The interface of an antiferromagnet and a superconductor supports solitonic zero-energy modes and becomes a topological superconductor with non-collinear spin order right at the edge.[101–104] Thus, the NS interface with the aforementioned (Sec. 3.2) canted-antiferromagnetic quantum Hall phase in graphene is expected to be an one-dimensional topological superconductor.[43] This theoretical ideia motivated several experiments, in particular, an experiment showing the interference of chiral Andreev states in quantum Hall graphene,[42] in which disorder plays a major role,[45] as we explore in more detail in part I of this thesis.

Combining van der Waals materials has also been a very active research field in materials science in the last few years. For example, a small twist angle between two graphene sheets results in a system with flat bands for which superconducting[11] and correlated insulator[12] phases appear, depending on the doping level. This is a result of the long range Moiré pattern due to the periodic coupling between the two layers. There are other ways to create superlattices in graphene, for example, by artificially generating strain fields that lead to buckling transitions, when placed on top of hexagonal diboride (hBN) and niobium diselenide ($NbSe_2$).[15] The buckling-induced periodic pseudo-magnetic field leads to the formation of nearly flat bands and correlated states,[16] as we explore in more detail on part II.

# Part I

# Majorana modes and Andreev chiral states in quantum Hall graphene

# 7 Effective model for Majorana modes in graphene

*All in all, it was all just bricks in the wall.*

Pink Floyd, Another brick in the wall

It was recently proposed that the interface between a graphene nanoribbon in the canted antiferromagnetic quantum Hall state and a s-wave superconductor may present topological superconductivity, resulting in the appearance of Majorana zero modes.[43] However, a description of the low-energy physics in terms of experimentally controllable parameters was still missing. Starting from a mean-field continuum model for graphene in proximity to a superconductor, we derive the low-energy effective Hamiltonian describing the interface of this heterojunction from first principles. A comparison between tight-binding simulations and analytical calculations with effective masses suggests that normal reflections at the interface must be considered in order to fully describe the low-energy physics.

## 7.1 Introduction

Zero-energy excitations in symmetry-protected topological superconducting systems are predicted to behave as zero energy Majorana quasi-particles.[105–107,72,108] Despite the recent experimental efforts to capture signatures of such excitations, there is still no general consensus regarding the existence of these ellusive zero-energy modes.[109–112] This problem stimulated a plethora of new theoretical proposals for systems supporting Majorana modes in a variety of nanosystems, from nanowires to two-dimensional heterostructures.[25,113–116,72] In this chapter, we consider the proposal of one-dimensional topological superconductivity at the interface of graphene/superconductor junctions,[43] experimentally motivated by ballistic junctions in quantum Hall regime and tunability of magnetic ordering.[117,49,90,118]

The possible appearance of Majorana modes in graphene relies on the interplay between three different phenomena (scheme in Fig. 6(b)).[43] First, each of the two degenerate zero energy eigenstates in the zeroth Landau level of quantum Hall graphene is restricted to a distinct combination of valley and sublattice indices. Hence, there is an

The content of this is chapter has been previously published as Antonio L. R. Manesco, G. Weber, and D. Rodrigues Jr., *Effective model for Majorana modes in graphene*, Phys. Rev. B **100**, 125411 (2019).

Figure 6 – (a) Scheme of the magnetization in the $A$ and $B$ sublattices; $\theta$ denotes the canting angle between both magnetizations. (b) Schematic representation of the graphene-superconductor setup considered in this chapter. For the derivation of the effective model, we considered an infinite ribbon along the $x$-axis (so that $k_x$ is a good quantum number). For negative values of $y$ (blue region), we added an orbital magnetic field, $B$, to induce Landau levels. The emergent magnetic ordering, with magnitude $m$, was treated as a mean field term. For $y > 0$ (orange region), we included an induced $s$-wave superconducting order parameter, $\Delta$, and chemical potential, $\mu$, as a result of a $s$-wave superconductor deposited over this region. The continuum Hamiltonian for this system is written in (7.2).

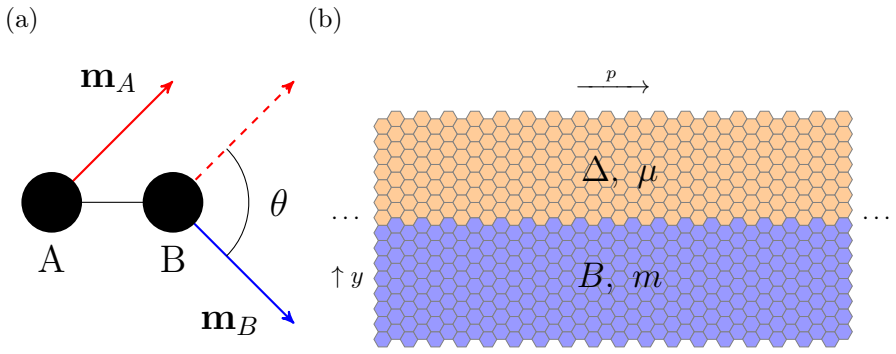


Source: author.

intrinsic identification of sublattice and valley degrees of freedom.[119–121] Second, electronic interactions lead to the emergence of a canted antiferromagnetic ordering that can be tuned by an applied Zeeman field, as shown in Fig. 6(a).[117,122,49,51] Thus, the aforementioned identification is enlarged to include spin degrees of freedom as well. As consequence, counter-propagating edge states with different helicities emerge, just as in a quantum spin Hall insulator [Fig. 4 (c)].[82,43] Finally, by inducing a superconducting order parameter the system becomes gapped and Majorana zero modes may emerge.[113] We also note that a similar phenomenon was predicted to occur at the interface between superconductors and antiferromagnetic insulators,[102] suggesting that the role of the quantum Hall state in graphene is just to induce high correlations in the flat-band zeroth Landau level.[51]

Mean-field simulations of such graphene/superconductor junctions corroborated this proposal for hosting Majorana zero modes, and an *ad hoc* phenomenological model for the edge states was proposed from numerical band diagram calculations. The model is described by the following effective low-energy Hamitonian:[43]

$$H_{\text{eff}} = \begin{pmatrix} \mu_1 + v_1 p & b_\theta & w & 0 \\ b_\theta & \mu_2 - v_2 p & 0 & w \\ w & 0 & -\mu_2 - v_2 p & b_\theta \\ 0 & w & b_\theta & -\mu_1 + v_1 p \end{pmatrix}, \tag{7.1}$$

where $\mu_i$ and $v_i$, $i = 1, 2$, are on-site energies and propagation velocities of the chiral modes, respectivelly. The topological gap is denoted by $b_\theta \propto \cos\theta$, where $\theta$ is the canting

angle between the magnetic moment of each sublattice, see Fig 6a. The ferromagnetic state corresponds to $\theta = 0$, while the antiferromagnetic state to $\theta = \pi$. The parameter $w$ represents the intervalley coupling and $p$ is the quasi-momentum along the interface direction. The Hamiltonian (7.1) is in the same representation of (7.6).

Starting from a mean-field continuum model for graphene, we derive the effective Hamiltonian (7.1) from a more constructive approach. Besides providing a better understanding of the physics described by (7.1), our approach allows us to express the phenomenological parameters in terms of real, experimentally controllable ones. In particular, we uncover the important role played by normal reflections at the graphene/superconductor interface, which have to be properly considered in order to fully describe the low-energy Hamiltonian.

This chapter is organized as follows. In Sec. 7.2, we propose a continuum Hamiltonian to describe a strip of graphene in the quantum Hall canted-antiferromagnetic (QHCAF) phase in proximity to an $s$-wave superconductor (SC). We then obtain an effective Hamiltonian to describe the interface physics by projecting the continuum Hamiltonian onto the zero energy modes at the QHCAF/SC interface. In Sec 7.3, we argue that some terms present in the Hamiltonian (7.1) can only be derived by considering termination-sensitive normal reflections at the QHCAF/SC interface. To account for these phenomena we consider effective masses that describe the boundary conditions at the interface. In section 7.4, we briefly discuss the appearance of Majorana modes and the resulting topological classification. Finally, in Sec. 7.5, we summarize our results and discuss some points that must be considered in future works.

## 7.2 The model

We start with a low-energy continuum Hamiltonian for the QHCAF/SC junction (illustrated in Fig. 6(b)). For $y < 0$, we consider graphene in the presence of a perpendicular orbital magnetic field ($B$), leading to the quantum Hall state. We also include a mean-field staggered magnetization energy ($m$), proposed as the explanation for the gap opening at graphene's zeroth Landau level.[117,122,49,51] For $y > 0$, we also consider graphene, but in proximity to an $s$-wave superconductor, leading to an induced order parameter ($\Delta$) and shifting the chemical potential to $\mu$, defined with respect to the Dirac cone. The presence of superconductivity repels the orbital magnetic field and, therefore, no magnetization is expected. In the valley-symmetric representation,[58] the Dirac-Bogoliubov-de Gennes (DBdG) Hamiltonian reads (using $\hbar = v = e = 1$)

$$\mathcal{H} = \Pi_x \Gamma_1 + \Pi_y \Gamma_2 + m \left( \Gamma_3 \sin\frac{\theta}{2} + \Gamma_4 \cos\frac{\theta}{2} \right) \Theta(-y) + (\Delta\Gamma_5 - \mu\Gamma_0)\,\Theta(y), \qquad (7.2)$$

Figure 7 – Local density of states and Majorana polarization for QHCAF/SC junctions. In the upper half of the panels, we have graphene with an induced $s$-wave superconducting coupling, whereas for the lower half we have graphene in: (a) ferromagnetic ($\theta = 0$); (b) antiferromagnetic ($\theta = \pi$); (c) canted-antiferromagnetic ($\theta = \pi/2$) states. (d) Majorana polarization[123,124] corresponding to (c). We used $B = 0.05\frac{\hbar}{ea^2}$, $m = 0.5t$, $\mu = 0.3t$ and $\Delta = 0.25t$, where $t$ is the hopping energy in order to reproduce the phenomenology with lower computational cost. The length unit is the lattice constant.

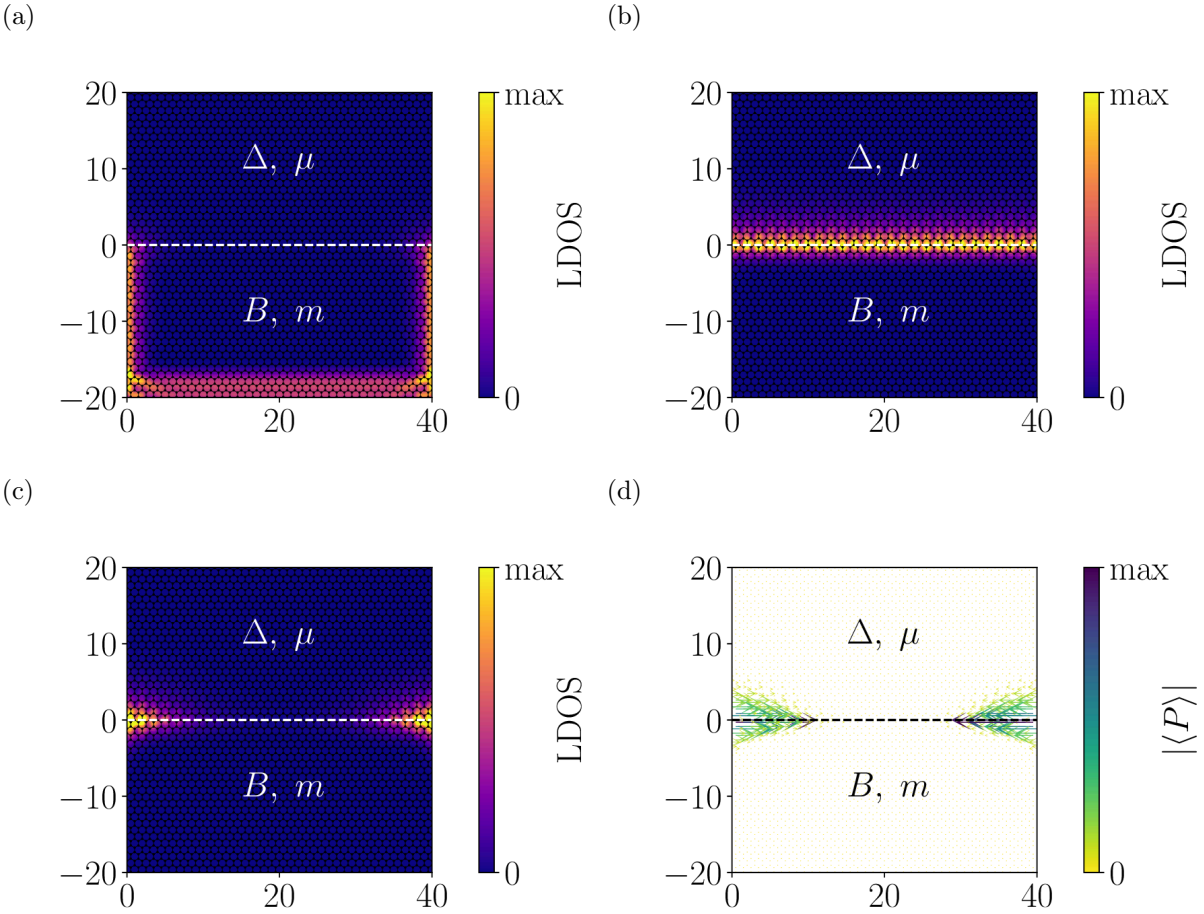


Source: author.

where $\Pi_i = p_i + A_i$ is the canonical momentum in the presence of a magnetic field $B$, $v$ is the Fermi velocity and $\theta$ is the magnetization canting angle between graphene sublattices. The Heaviside step function is denoted by $\Theta(y)$. In order to preserve translational symmetry along the $x$-axis, we consider the Landau gauge $\mathbf{A} = (By, 0, 0)$ for $y < 0$. Moreover, we set $\mathbf{A} = (0, 0, 0)$ for $y > 0$ to ensure the continuity of the gauge field and properly account for the Meissner effect. We relegate the explicit expressions for the spinors and $\Gamma$-matrices to Appendix A.1.

To properly integrate out the extra degrees of freedom and derive a model that describes only the interface states, we first examine numerical results from a tight-binding implementation of (7.2) using the Kwant code.[125] Figure 7 shows the local density of

states and Majorana polarization[123,124] at zero energy under three situations: ferromagnetic ($\theta = 0$), antiferromagnetic ($\theta = \pi$) and canted-antiferromagnetic ($\theta = \pi/2$) orderings. Since only the antiferromagnetic state exhibits zero energy modes that extend all over the interface, we impose $\theta = \pi$ in (7.2). Setting, without any loss in generality, $p_x = 0$, we solve $\mathcal{H}_0\psi = 0$ to find the zero energy states of

$$\mathcal{H}_0 = -i\Gamma_2\partial_y + (By\Gamma_1 + m\Gamma_3)\,\Theta(-y) + (\Delta\Gamma_5 - \mu\Gamma_0)\,\Theta(y). \tag{7.3}$$

Diagonalizing (7.3), we obtain the following eigenstates

$$\psi_\alpha(y) = \frac{1}{\mathcal{N}} e^{\lambda_\alpha(y)}\psi_\alpha^{(0)}(y), \tag{7.4}$$

where $\lambda_\alpha(y)$ and $\psi_\alpha^{(0)}(y)$ are, respectively, the eigenvalues and eigenspinors of

$$\Lambda(y) = -i\int_0^y d\xi\ \Gamma_2^{-1}\left[\Theta(-\xi)(B\xi\Gamma_1 + m\Gamma_4) + \Theta(\xi)\,(\Delta\Gamma_5 - \mu\Gamma_0)\right],$$

and $\mathcal{N}$ is a normalization constant. Next, we impose two physical constraints on the eigenfunctions: (i) regularity at spatial infinity, *i.e.*, we discard all solutions $\psi_\alpha(y)$ that diverge as $y \to \pm\infty$; (ii) continuity at the interface. We relegate the lengthy expressions for the resulting eigenbasis $\{\tilde{\psi}_\alpha\}$ to Appendix A.2.

We can finally derive an effective Hamiltonian for general interface states by calculating

$$\mathcal{H}_{\text{eff}}^{\alpha\beta} = \langle\tilde{\psi}_\alpha|\mathcal{H} - \mathcal{H}_0|\tilde{\psi}_\beta\rangle. \tag{7.5}$$

In terms of the spinor basis $\Psi = i(-\psi_{+-}, \psi_{++}, -\psi_{--}, \psi_{-+})^T$, it reads

$$\mathcal{H}_{\text{eff}} = \begin{pmatrix} \tilde{v}p & b_\theta & 0 & 0 \\ b_\theta & -\tilde{v}p & 0 & 0 \\ 0 & 0 & -\tilde{v}p & b_\theta \\ 0 & 0 & b_\theta & \tilde{v}p \end{pmatrix}. \tag{7.6}$$

Thus, the effective degrees of freedom correspond to four chiral modes with the same propagation velocity $\tilde{v}$. There is also an intravalley coupling between the two different helicities, $b_\theta = \tilde{\Delta}\cos\theta$, that vanishes for antiferromagnetic ordering ($\theta = \pi$). The explicit expressions for $\tilde{v}$ and $\tilde{\Delta}$ can be found in (7.16).

The resulting effective Hamiltonian (7.6) coincides with the phenomenological model (7.1) only in the case of vanishing on site energies, $\mu_1 = \mu_2 = 0$, absence of intervalley coupling, $w = 0$ and coinciding propagation velocities $v_1 = v_2 = \tilde{v}$. The first two deficiencies of our effective model are related to not taking into account the effect of terminations and normal reflections on the physics of the edge states. On the other hand, the indistinguishability of the propagation velocities is a limitation of the first order

expansion performed near the Fermi level to obtain the continuum model for graphene. These issues will be dealt with in details in the next section. We note, nonetheless, that the topological gap, $b_\theta$, is the same in both models. Thus, one may expect the appearance of bound states whenever the gap changes sign, as explained in the Section 7.4.

## 7.3 Effect of terminations and normal reflections

It is well known that the effect of atomic structure in graphene-vacuum boundaries is crucial to fully describe the low-energy spectrum of finite systems.[58] However, to the best of our knowledge, so far no systematic study was performed to account for similar effects in graphene/superconductor junctions. In Sec. 7.2, the only boundary condition imposed at the interface was the continuity of the eigenspinors to enforce the effects of Andreev reflections.[93,91] Thus, termination physics associated with normal reflections were not considered. In the following, we provide numerical evidence that termination dependent boundary conditions corresponding to normal reflections are needed to fully describe the low-energy dynamics.

### 7.3.1 Numerical analysis

Tight-binding numerical simulations of graphene nanoribbons corresponding to the system described by the Hamiltonian (7.2) were conducted for both armchair and zigzag prinstine interfaces using the Kwant code.[125] We have used a set of unrealistic parameters that emphasize the actual phenomenology and keep a lower computational cost. The same qualitative results were obtained with realistic parameters.[43,117,122,49,51] The complete electronic band structure and low-energy spectrum for $\theta = \pi$ are shown in Fig. 8. Clearly, different phenomenologies are expected for armchair and zigzag interfaces. For zigzag boundaries, Fig. 8(d) and 8(e), there is an energy offset for the Dirac cones in relation to the Fermi level, corresponding to the different $\mu_1$ and $\mu_2$ in the phenomenological model (7.1). On the other hand, for armchair boundaries, Fig. 8(a), 8(b) and 8(c), there is a gap, captured by the energy $w$ in (7.1), due to intervalley scattering. This gap can be softened by substituting the step function variation of parameters in Eq. (7.2) by smooth functions, such as $\tanh(y)$.

Next, we consider the effect of varying the chemical potential at the superconducting regions. For higher values, see Fig. 8(b) for armchair interfaces and 8(d) for zigzag boundaries, there is an obvious difference in the propagation velocities of the chiral modes, captured by the different $v_1$ and $v_2$ in (7.1). This is probably because, at the high-doping regime, we are sufficiently far away from the Fermi level. In this case, the linear expansion used to derive the continuum model for graphene, on which the Hamiltonian (7.2) is based, does not reproduce all relevant phenomena.[126] In other words, higher-order terms

Figure 8 – Band diagrams for pristine armchair (a), (b) and (c) and zigzag (d) and (e) graphene nanoribbons. All calculations were performed for $60a$ width ribbons divided in half: the superconducting-induced region for $y > 0$ and quantum Hall regime for $y < 0$. Also, $B = 0.05\frac{\hbar}{ea^2}$, $m = 0.5t$ and $\Delta = 0.1t$, where $t$ is the hopping constant. These parameters do not correspond to realistic conditions, but they preserve the phenomenology and have lower computational costs. For the armchair ribbons, (b) and (c), a smooth variation of the parameters was used, proportional to $\tanh y$, which results in a significant reduction of the gap, when compared with the variation proportional to the Heaviside step function (a). In (a), (b) and (d), $\mu = 0.5t$, while, for (c) and (e), $\mu = 0.05t$. We stress that for higher values of $\mu$, there is a considerable asymmetry between the propagation velocities, whereas lower values of $\mu$ result in a negligible asymmetry. Finally, we note that an energy offset of the Dirac cones with respect to the Fermi level is only present for zigzag ribbons.

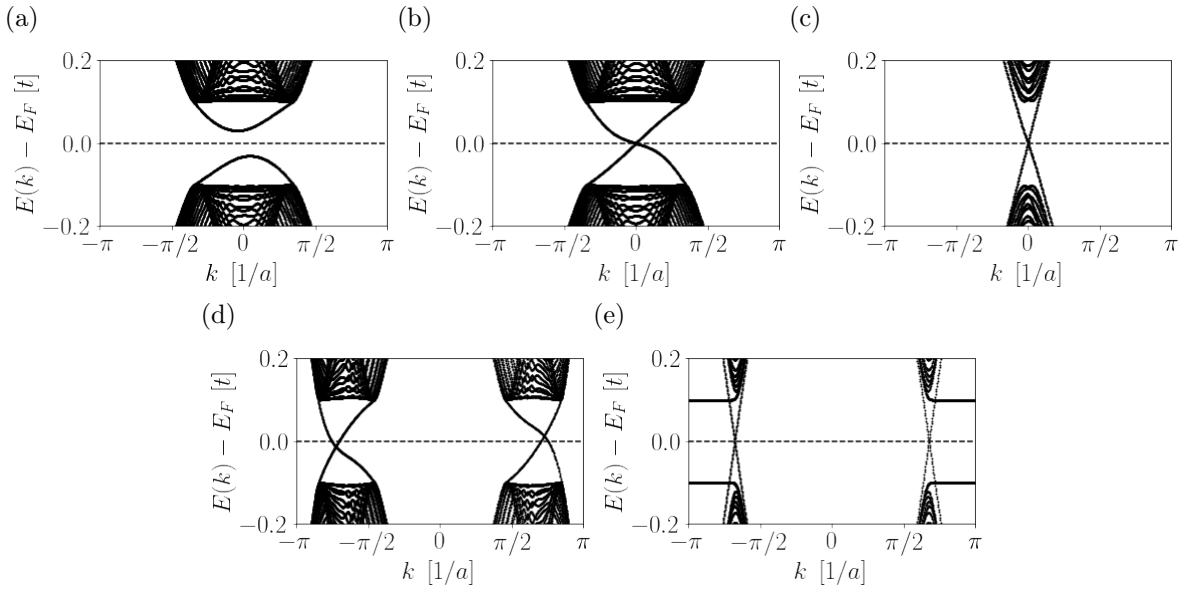


Source: author.

in momentum must be taken into account. Thus, for simplicity, we restrict our analysis to the commonly used low-doping regime,[91,126] in which $v_1 \approx v_2$, see Fig. 8(c) and 8(e).

Therefore, we expect that termination physics may account for the remaining terms in the Hamiltonian. That is what we derive next.

### 7.3.2 Analytical treatment

The effect of termination physics may be addressed by including in the Hamiltonian effective potentials that enforce the desired boundary conditions. Since we have already accounted for Andreev reflections by imposing the continuity of the wave functions at the interface, we need only consider effective potentials describing normal reflections.

Consider a general energy independent boundary condition for the Dirac equation

corresponding to the following linear restriction on the wave function

$$\psi(\mathbf{r}_B) = M\psi(\mathbf{r}_B), \tag{7.7}$$

where $M$ is an arbitrary Hermitian and unitary matrix. It can be expressed in the form of an additional confinement potential at the boundary $\mathbf{r}_B$ as:[127]

$$V_{term}(\mathbf{r}_B) = v_{term}\delta(\mathbf{r}_B)\tilde{M}, \tag{7.8}$$

where $v_{term}$ is a constant that represents the strength of the potential. The relation between the matrices $M$ and $\tilde{M}$ can be easily obtained by integrating the Dirac equation including the confinement potential (7.8) across an infinitesimal width of the boundary, leading to

$$\tilde{M} = -\frac{i}{v}\mathbf{J}M, \tag{7.9}$$

where $\mathbf{J}$ is the current operator.

For normal reflections,[58] there are three contributions to $\tilde{M}$,

$$\tilde{M}_{ac} = \tau_3 \otimes \rho_1 \otimes s_3 \otimes \sigma_0, \tag{7.10}$$

$$\tilde{M}_{im} = \tau_3 \otimes \rho_3 \otimes s_3 \otimes \sigma_0, \tag{7.11}$$

$$\tilde{M}_{zz} = \tau_3 \otimes \rho_3 \otimes s_1 \otimes \sigma_0, \tag{7.12}$$

corresponding to armchair ($ac$), infinite mass ($im$, sublattice imbalance) and zigzag ($zz$) potentials. So that the effective potential enforcing normal reflections has the following form:

$$V_{term}(y) = V^{zz}_{term}(y) + V^{im}_{term}(y) + V^{ac}_{term}(y). \tag{7.13}$$

We include the effect of the termination potential (7.13) in the Hamiltonian as

$$\mathcal{H}^{\alpha\beta}_{\text{eff}} \mapsto \mathfrak{H}^{\alpha\beta}_{\text{eff}} = \mathcal{H}^{\alpha\beta}_{\text{eff}} + \langle\psi_\alpha|V_{term}(y)|\psi_\beta\rangle. \tag{7.14}$$

Noting also that the $y$-dependence of the $V_{term}$ can be neglected, since the form of the wave functions $\psi_\alpha(y)$ guarantees that such terms have support only at the interface, the resulting Hamiltonian, in the same representation of Eq. 7.6, reads

$$\mathfrak{H}_{\text{eff}} = \begin{pmatrix} \mu_1 + \tilde{v}p & b_\theta & w & 0 \\ b_\theta & \mu_2 - \tilde{v}p & 0 & w \\ w & 0 & -\mu_2 - \tilde{v}p & b_\theta \\ 0 & w & b_\theta & -\mu_1 + \tilde{v}p \end{pmatrix}. \tag{7.15}$$

The different chemical potentials $\mu_1$ and $\mu_2$ derive from the infinite mass and zigzag potentials, and the intervalley mixing energy $w$, from the armchair potential. The explicit expressions for the parameters are:

$$\tilde{v} = \frac{1}{\mathcal{N}^2}\left(2\int_{-\infty}^{0} dy\ \chi(y) - \frac{2\Delta}{\Delta^2 + \mu^2}\right), \tag{7.16a}$$

$$\tilde{\Delta} = \frac{B}{\mathcal{N}^2}\int_{\infty}^{0} dy\ \chi(y), \tag{7.16b}$$

$$\chi(y) = \frac{4me^{y\sqrt{B^2y^2+4m^2}}}{\sqrt{B^2y^2+4m^2}}, \tag{7.16c}$$

$$\tilde{\mu} = \frac{Bv_{im}}{\mathcal{N}^2}\int_{-\infty}^{0} dy\ \frac{y\chi(y)}{m}, \tag{7.16d}$$

$$\delta\tilde{\mu} = \frac{2}{\mathcal{N}^2}\left(v_{zz}\int_{-\infty}^{0} dy\ \chi(y) + \frac{\Delta v_{zz}+\mu v_{im}}{\Delta^2+\mu^2}\right), \tag{7.16e}$$

$$w = \frac{2v_{ac}}{\mathcal{N}^2}\left(\frac{\Delta}{\Delta^2+\mu^2} + 2\int_{-\infty}^{0} dy\ e^{y\sqrt{B^2y^2+4m^2}}\right), \tag{7.16f}$$

$$\mu_1 = \tilde{\mu} + \delta\tilde{\mu}, \tag{7.16g}$$

$$\mu_2 = \tilde{\mu} - \delta\tilde{\mu}. \tag{7.16h}$$

Thus, the effective Hamiltonian (7.15) completely describes the expected phenomenology of graphene terminations. The chemical potentials $\mu_1$ and $\mu_2$ shift the Dirac cones for zigzag interfaces. On the other hand, the armchair potential does not shift the cones, but couple different valleys, leading to a gap opening energy $w$. We can finally check the existence of Majorana zero modes for finite systems and explore the topological classification.

## 7.4 Majorana modes and the topological classification

### 7.4.1 Majorana modes

For the sake of clarity, we will use in this section the following spinor representation $\psi = (\psi_{++}, \psi_{+-}, \psi_{-+}, \psi_{--})^T$. In this representation, the Hamiltonian (7.6) takes the simpler form

$$\tilde{\mathcal{H}}_{\text{eff}} = vp\kappa_3 \otimes \eta_3 + b_\theta \kappa_0 \otimes \eta_1, \tag{7.17}$$

where $\{\kappa_\alpha\}_{\alpha=0}^3$ and $\{\eta_\alpha\}_{\alpha=0}^3$ are sets with the identity and Pauli matrices in the usual representation. The indices of the spinor components, $\psi_{\kappa\eta}$, represent the eigenvalues of $\kappa_3$ e $\eta_3$, respectively.

We can now show that gap closings in (7.17) result in zero energy states that are, indeed, Majorana modes. Making the $x$-dependence of the intravalley coupling explicit, *i.e.*, $b_\theta = b_\theta(x)$, and assuming that it changes sign at $x = 0$, we can expand (7.17) around $x = 0$ to obtain:

$$\tilde{\mathcal{H}}^2_{\text{eff}} = \tilde{v}^2p^2\kappa_0 \otimes \eta_0 + x^2\mathcal{B}_\theta^2\kappa_0 \otimes \eta_0 - \mathcal{B}_\theta\tilde{v}\kappa_3 \otimes \eta_2, \tag{7.18}$$

with $\mathcal{B}_\theta = \partial_x b_\theta|_{x=0}$. The energy spectrum is then easily obtained:

$$E_n^{\kappa,\eta} = \pm\sqrt{2\mathcal{B}_\theta\tilde{v}\left(n+\frac{1}{2}\right) - \kappa\eta\mathcal{B}_\theta\tilde{v}} \tag{7.19}$$

with $\kappa, \eta = \pm$. Also, note that the ground state is doubly degenerate:

$$\gamma_\pm(x) = \langle x|n=0, \kappa=\pm, \eta=\pm\rangle. \tag{7.20}$$

The appearance of these bound states should not be surprising, since it corresponds to a change of the topological invariant on the phenomenological model (7.1),[43] for $\mu_1 = \mu_2 = w = 0$ and $v_1 = v_2 = \tilde{v}$ as we will discuss in Chapter 8.

## 7.5 Summary

In this chapter, we presented a formal derivation of the phenomenological Hamiltonian proposed to describe graphene/superconductor junctions at low-doping. Our approach allows the understanding of such systems in terms of experimentally controllable parameters, although the correspondence between the phenomenological and experimental parameters is highly nontrivial. It was found that, in order to completely describe the low energy spectrum of such junctions, effects related to normal reflection must be taken into account. Generalizing our results to describe graphene/superconductor junctions also at high-doping requires considering higher order corrections in the continuum model for graphene.

# 8 A mathematical detour: Hidden chiral symmetries in BDI multichannel Kitaev chains

*Sometimes I'll start a sentence and I don't even know where it's going. I just hope I find it along the way.*

Michael Scott, The Office

Realistic implementations of the Kitaev chain require, in general, the introduction of extra internal degrees of freedom. In chapter 7, for example, we noted that extra degrees of freedom in graphene, compared to the Kitaev chain, doubles the dimension of the corresponding Hilbert space. To address this situation, we discuss the presence of hidden BDI symmetries for free Hamiltonians describing systems with an arbitrary number of internal degrees of freedom. We generalize the results of a spinfull Kitaev chain to obtain a Hamiltonian with $n$ internal degrees of freedom and derive the corresponding hidden chiral symmetry. As an explicit application of this generalized result, we exploit by analytical and numerical calculations the case of a spinful 2-band Kitaev chain, which can host up to 4 Majorana bound states. We also observe the appearence of minigap states, when chiral symmetry is broken. Finally, we use the developed tools to classify 1D topological superconductivity in quantum Hall graphene/superconductor devices.

## 8.1 Introduction

In 1937, Ettore Majorana proposed that a suitable choice for the $\gamma$-matrix representation would lead to real solutions of the Dirac equation, thus implying that the fermions described by these field solutions corresponded to their own antiparticles.[128] In the past few years, this concept became extremely relevant in the context of Condensed Matter Physics, as Majorana quasiparticle excitations were predicted to emerge in topological superconductors, displaying non-abelian anyonic statistics. This very exotic exchange property has been considered, since then, a very promising route for solving the decoherence problem related to quantum information processing.[25,24,72,129]

The content of this is chapter has been previously published as Antonio L. R. Manesco, G. Weber, and D. Rodrigues Jr., *Hidden chiral symmetries in BDI multichannel Kitaev chains*, J. Phys.: Condens. Matter **30** 175401 (2018) and Antonio L. R. Manesco, G. Weber, and D. Rodrigues Jr., *Effective model for Majorana modes in graphene*, Phys. Rev. B **100**, 125411 (2019).

Alexei Kitaev, in a seminal paper, introduced a simple toy model, corresponding to a one-dimensional spinless $p$-wave superconductor, capable of hosting Majorana zero energy excitations at both ends.[25] A considerably large number of realistic systems exhibiting such phenomenon were then proposed. The most prominent example consists of a semiconductor nanowire with high spin-orbit coupling in the presence of a magnetic field and in proximity to a $s$-wave superconductor.[130–132] Besides the theoretical predictions, there has also been a substantial experimental effort devoted to detecting Majorana bound states in such nanowire heterostructures.[133,28,134,31,35,32,135,136] In addition, materials with triplet $p$-wave superconductivity, such as organic superconductors and the quasi-one-dimensional $Li_{0.9}Mo_6O_{17}$,[137] as well as other heterostructures such as ferromagnetic nanowires,[116] were predicted to host Majorana bound states.

More realistic realizations of the Physics underlying this Kitaev chain may only be obtained with the introduction of internal degrees of freedom, even though it eventually changes the topological classification of the system. For example, for systems such as organic superconductors, quasi-one-dimensional triplet superconductors (like $Li_{0.9}Mo_6O_{17}$) and ferromagnetic nanowires, the relevant internal spin degrees of freedom lead to two different topological classifications: BDI and DIII. In a few words, in such two classes, all relevant discrete symmetries: time-reversal ($\mathcal{T}$), particle-hole ($\mathcal{C}$) and chiral ($\mathcal{S} = i\mathcal{C}\mathcal{T}$) symmetries are preserved.[a] The only difference being that in the former the time-reversal operator squares to $+\mathbb{1}$ while in the latter, to $-\mathbb{1}$.[138,139] The BDI class is characterized by a $\mathbb{Z}$ invariant winding number,[137,140,116] while DIII presents a $\mathbb{Z}_2$ invariant.[141] In semiconductor nanowire heterostructures, a common feature is the appearance of subbands due to size quantization. This requires the introduction of band mixing terms in the Hamiltonian, which break the usual time reversal (with $\mathcal{T}^2 = -\mathbb{1}$, thus DIII) and the chiral symmetry.[142–145] However, as we have previously shown, hidden BDI chiral symmetries can also be introduced in some limits.[142] Also, multiple Majorana modes counted by a winding number were predicted to appear in long-range hopping systems.[146,147]

As a matter of fact, correctly accounting for discrete symmetries, such as the chiral symmetry discussed above, is of extreme experimental significance. Particularly, this breaking of chiral symmetry may lead to the appearance of minigap states, which interfere in the observation of a clear zero-bias peak used as a signature for the presence of Majorana bound states in the system.[133,148] Moreover, theoretical studies of coupled Kitaev chains (Kitaev ladders)[149–151] and multiband systems,[151–153] as well as the recently reported experimental evidence of topological phenomena in a multiband superconductor,[154] corroborate the importance of considering the influence of pairings between internal degrees of freedom on the topological classification of superconductors.

In the context of the following discussion, a non-trivial topological phase of matter is

[a] For both BDI and DIII classes $\mathcal{C}^2 = \mathbb{1}$.

a gapped ground state that cannot be adiabatically connected to the vacuum without closing the gap nor breaking any discrete symmetry (namely, time-reversal, charge-conjugation and chirality). From a mathematical point of view, we are interested in fiber bundles where the base space is the Brillouin zone and the fiber is the subspace of the Hilbert space formed by the ground state vectors. If there is no homeomorphism (modulo trivial core bands) between the total space manifold of a given phase and the vacuum, the system is said to be topologically non-trivial. The presence of discrete symmetries imposes constraints on the Hilbert space and, therefore, also constrains the fiber's group. There are ten possible combination of the three discrete symmetries, and the corresponding group structures are the ten Cartan symmetric spaces.

The number of topologically distinct phases hosted by system with fixed discrete symmetries and number of spatial dimensions corresponds to the number of homotopically innequivalent fiber bundles (modulo trivial bundles) that can be constructed over a given Brillouin zone. Using homotopy arguments in the context of K-theory, it is possible to exploit the Bott periodicity to construct a *periodic table* of symmetry protected topological states.[79,138,27] It is worth noting that there are alternative ways to characterize the ten Cartan symmetric spaces: in terms of the time evolution operator, or in terms of the target spaces of nonlinear sigma models. Regardless of how one obtains the symmetry classes, after fixing the spatial dimensions and the discrete symmetries, topological invariants can be computed by holonomy arguments. A more detailed mathematical discussion regarding the topological classification can be found elsewhere.[139,155,27,156]

Since in superconductors charge conjugation ($\mathcal{C}$) is manifestly present, the other two discrete symmetries ($\mathcal{T}$ and $\mathcal{S}$), which should occur simultaneously or not at all, are the ones that have to be carefully analyzed when adding internal degrees of freedom, *i.e.*, increasing the dimension of the fiber's group structure. For one-dimensional topological superconductors, several works have suggested the introduction of pseudo-time-reversal operators,[157,137,116] resulting, for example, in the uncovering of hidden chiral symmetries in spinful systems.[140] In this chapter, we propose some conditions to construct Kitaev Hamiltonians with an arbitrary number of internal degrees of freedom and argue that it is also possible to define a hidden BDI chiral symmetry for a given superconducting order parameter. These results are applied for a spinful two-band Kitaev chain.

This chapter is organized as follows. In Sec. 8.2, we review the general ideas regarding the classification of one-dimensional topological superconductors, discussing the appropriate topological invariants for a given set of discrete symmetries. In Sec. 8.3.1, we briefly review the chiral symmetry leading to the BDI class[140] and the following geometrical interpretation of the constraints it imposes on the Hamiltonian for the existence of non-trivial topological invariants. In Sec. 8.3.2, we consider, in general, the problem of constructing a Kitaev chain with $n$ degrees of freedom and show how to implement the

Nambu representation to find hidden chiral symmetries. In Sec. 8.3.3, we particularize the previous construction to consider in details the case of a spinful Kitaev chain with two bands. We use the formalism to review the topological classification of quantum Hall graphene/superconductor devices (Sec. 8.3.4). Finally in Sec. 8.4, we summarize our results and point out some interesting directions and open problems.

## 8.2 Classification of chiral topological superconductors

As previously discussed, non-trivial topological phases in condensed matter emerge as a consequence of the dimensionality of the system and the discrete symmetries it preserves.[79,138,27] For superconductors, the mean-field Bogoliubov-de Gennes theory manifestly preserves charge conjugation ($\mathcal{C}$) by construction. Thus, a chiral symmetric system with non-trivial topology necessarily requires time-reversal symmetry, or even a pseudo-time-reversal symmetry, to coexist.[72,140] By pseudo-time-reversal invariance, we mean a symmetry defined by an antiunitary operator that commutes with the Hamiltonian, but does not have the usual physical meaning of a time-reversal. Finally, in a one-dimensional superconductor, given a (pseudo-)time-reversal operator $\mathcal{T}$, the set of possible values for the topological invariant depends on the sign of $\mathcal{T}^2$.[27] In the following, we discuss in more detail these two cases.

For the BDI class, there is a (pseudo-)time-reversal operator satisfying $\mathcal{T}_{BDI}^2 = \mathbb{1}$. Hence, a chiral symmetry operator related to this (pseudo-)time-reversal can be defined as:

$$\mathcal{S}_{BDI} = i\mathcal{C}\mathcal{T}_{BDI}. \tag{8.1}$$

The most general massive $N$-dimensional Dirac Hamiltonian in the Bloch representation can be written in terms of $\Gamma$ matrices as:

$$H_k = h_k^0\Gamma_0 + \sum_{a=1}^{N} h_k^a\Gamma_a \ , \quad \{\Gamma_a, \Gamma_b\} = 2\delta_{ab}, \tag{8.2}$$

where $N = 2n$ is the number of internal degrees of freedom (the factor 2 comes from particle-hole space), $\Gamma_0$ is the corresponding identity matrix and the subscript $k$ indicates a momentum dependency. Noting that mass terms, such as any term proportional to the identity matrix, explicitly break chiral invariance, we restrict our analysis to the massless case, $h_k^0 = 0$. Hence, we can introduce a generalization of the Anderson pseudospin vector $\hat{h}_k = \mathbf{h}_k/\|\mathbf{h}_k\|$, with $\mathbf{h}_k = (h_k^1, \ldots, h_k^N)$.[157,72,27]

Following the ideas of Tewari and Sau,[157] we can now study the manifold determined by $\hat{h}_k$. For a linear chain in first-neighbors approximation, it is possible to write:

$$\hat{h}_k = \Lambda_0 + \Lambda_1 \sin k + \Lambda_2 \cos k, \tag{8.3}$$

where $\{\Lambda_i\}_{i=0}^{2}$ are constant $N$-vectors. Thus, $\hat{h}_k$ parametrizes a manifold $\mathfrak{T} \cong S^1$, so that the number of times the vector $\hat{h}_k$ winds around the origin while the momentum $k$ goes through the Brillouin zone (BZ) defines distinct topological phases, characterized by a different number of Majorana excitations. In other words, the number of Majorana bound-states can be counted by a topological invariant called the *winding number*, $w \in \pi_1(\mathfrak{T}) = \mathbb{Z}$, defined as:[158,157]

$$w = \left| \oint_{BZ} \frac{dk}{4\pi i} \mathrm{tr}\left[\mathcal{S}_{BDI} H_k^{-1} \partial_k H_k\right] \right|, \tag{8.4}$$

where $\mathcal{S}_{BDI}$ is the chiral symmetry operator related to the (pseudo-)time-reversal by (8.1).

On the other hand, systems with a (pseudo-)time-reversal operator that obeys $\mathcal{T}_{DIII}^2 = -\mathbb{1}$ are in the DIII class. Although we will not make any further comments on how to obtain topological invariants for this class,[b] it is important to remark the main difference between systems in the classes BDI and DIII: the presence of a (pseudo-)time-reversal operator that squares to $-\mathbb{1}$ implies the presence of Kramer's degeneracy between Majorana excitations.[160] Hence, for one pair of Majoranas to be annihilated, such degeneracy must be broken, requiring that (pseudo-)time-reversal and chiral symmetry be also broken. As a consequence, a DIII system with multiple pairs of Majorana zero modes can have only two distinct topological phases: one with and another without Majoranas (effectivelly, we can interpret the linear combination of these multiples zero modes as as just one mode). As a result, one must expect a $\mathbb{Z}_2$ invariant instead of $\mathbb{Z}$, which means that the map $\hat{h}_k$ can wind around the origin $n$ times or cannot wind at all, *i.e.*, no intermediary value between 0 and $n$ is possible.

In the following, we focus only on the BDI class, studying how additional internal degrees of freedom may change the behavior of the winding number. To do so, we search for a hidden chiral symmetry, namely an operator:[72,158]

$$\mathcal{S} = i\mathcal{C}\mathcal{T} \quad \text{with} \quad \{H_k, \mathcal{S}\} = 0, \tag{8.5}$$

defined by the physics of the triplet superconducting order parameter. We start from the idea of hidden chiral symmetry introduced by Dumitrescu *et. al.*[140] for spinful systems.

## 8.3 The models

### 8.3.1 A quick review on the spinfull Kitaev chain

We propose a generalized Hamiltonian for a spinfull $p$-wave superconductor considering all possible pairings between the spin channels that are physically compatible with

[b] For a more detailed discussion about the topological classes D, BDI and DIII, we refer the interested reader to the works of Budich and Ardonne[141] and Sedlmayr *et. al.*[159].

the triplet superconducting state. On Wannier representation, it reads

$$\mathcal{H} = \mathcal{H}_0 + \mathcal{H}_R + \mathcal{H}_{SC}, \tag{8.6}$$

$$\mathcal{H}_0 = -\sum_{n,\sigma,\sigma'} \mu_{\sigma\sigma'} c^\dagger_{n\sigma'} c_{n\sigma} + t_{\sigma\sigma'} c^\dagger_{n+1\sigma'} c_{n\sigma} + h.c., \tag{8.7}$$

$$\mathcal{H}_R = \sum_{n,\sigma,\sigma'} i\lambda_{\sigma\sigma'} c^\dagger_{n+1\sigma'} c_{n\sigma} + h.c., \tag{8.8}$$

$$\mathcal{H}_{SC} = \sum_{n,\sigma,\sigma'} (i\sigma_2 \mathbf{d}\cdot\boldsymbol{\sigma})_{\sigma,\sigma'} c^\dagger_{n\sigma} c^\dagger_{n+1\sigma'} + h.c., \tag{8.9}$$

where $\mu_{\sigma\sigma'}$ and $t_{\sigma\sigma'}$ are the spin dependent chemical potential and the hopping energy, respectively; $i\lambda_{\sigma\sigma'}$ is a purely complex hopping which gives rise to the Rashba spin-orbit coupling[161] and $\mathbf{d} = (\Delta_1, \Delta_2, \Delta_3)$ is the triplet superconducting order parameter. The fermion field operators $c_{n\sigma}$ and $c^\dagger_{n\sigma}$ obey

$$\{c_{n\sigma}, c^\dagger_{m\sigma'}\} = \delta_{nm}\delta_{\sigma\sigma'}, \tag{8.10}$$

where the indices $n,\ m$ label lattice positions while $\sigma,\ \sigma'$ label the spin projection along the $z$-axis. The set $\{\sigma_\nu\}_{\nu=0}^4$ consists of the $2\times 2$ identity matrix and the usual Pauli matrices for the spin space.

For convenience, we rewrite the Hamiltonian (8.6) in Bloch representation as

$$\mathcal{H} = \int_{BZ} \frac{dk}{2\pi}\, \psi^\dagger_k\, H_k\, \psi_k, \tag{8.11}$$

where $BZ$ indicates integration over all momenta within the Brillouin zone. Using the Nambu representation[162] $\psi_k = (c_k, \mathcal{T}c_k)^T$, $c_k = (c_{k\uparrow}, c_{k\downarrow})^T$, $\mathcal{T} = i\sigma_2\mathcal{K}$, with $\mathcal{K}$ denoting the complex conjugation operator, we obtain[c]

$$H_k = \tau_3 \otimes (\epsilon^0_k\sigma_0 + \boldsymbol{\lambda}_k\cdot\boldsymbol{\sigma}) + \tau_0 \otimes (\lambda^0_k\sigma_0 + \boldsymbol{\epsilon}_k\cdot\boldsymbol{\sigma}) + \tau_\phi \otimes \mathbf{d}_k\cdot\boldsymbol{\sigma}, \tag{8.12}$$

where $\{\tau_\nu\}_{\nu=0}^4$ is the set with the $2\times 2$ identity and the Pauli matrices for particle-hole space; $\tau_\phi = \tau_1\sin\phi + \tau_2\cos\phi$, $\phi$ is the superconducting phase and

$$[\epsilon^\nu_k\sigma_\nu]_{\sigma\sigma'} = -\mu_{\sigma\sigma'} - 2t_{\sigma\sigma'}\cos k, \tag{8.13}$$

$$[\lambda^\nu_k\sigma_\nu]_{\sigma\sigma'} = 2\lambda_{\sigma\sigma'}\sin k, \tag{8.14}$$

$$\mathbf{d}_k = \mathbf{d}\sin k. \tag{8.15}$$

We note that

$$-\mu_{\sigma\sigma'} = -\mu\sigma_0 + \mathbf{B}\cdot\boldsymbol{\sigma}, \tag{8.16}$$

where $\mu$ is the chemical potential and $\mathbf{B}$ is a Zeeman field. Also,

$$t_{\sigma\sigma'} = t\sigma_0 + \mathbf{C}\cdot\boldsymbol{\sigma}, \tag{8.17}$$

[c] From now on, we use Einstein summation convention for repeated indices; greek letters are used for sums starting from 0, while latin letters are reserved for sums starting from 1.

where $t$ is the spin independent hopping energy, $\mathbf{C}$ is the spin dependent hopping energy.

The Hamiltonian with no spin-dependent hopping was proposed as a realistic model for organic superconductors, such as the quasi-one-dimensional triplet superconductor $Li_{0.9}Mo_6O_{17}$, and ferromagnetic nanowires with zero $s$-wave order parameter.[137,140,116] Moreover, it was also pointed out that the parameter choice leads to two possible chiral operators, *i.e.*, unitary operators that anticommute with the Hamiltonian. One is the chiral symmetry related to the DIII classification, $\mathcal{S}_{DIII} = \tau_{\phi+\pi/2} \otimes \sigma_0$, a consequence of the invariance under the physical time-reversal operator defined by $\mathcal{T}_{DIII} = \tau_0 \otimes i\sigma_2\mathcal{K}$, given $\mathcal{C} = \tau_{\phi+\pi/2} \otimes \sigma_2\mathcal{K}$. The other is the hidden chiral symmetry associated with the BDI classification, $\mathcal{S}_{BDI} = \tau_{\phi+\pi/2} \otimes \hat{d}\cdot\boldsymbol{\sigma}$, $\hat{d} = \mathbf{d}/\|\mathbf{d}\|$, with a corresponding pseudo-time-reversal operator given by $\mathcal{T}_{BDI} = \tau_0 \otimes \left[\hat{d}\cdot\hat{e}_2 + i\left(\hat{d}\wedge\hat{e}_2\right)\cdot\boldsymbol{\sigma}\right]\mathcal{K}$.

The conditions for preserving chiral symmetry in a BDI system have an interesting geometric interpretation which we explore next. Imposing chiral symmetry leads to

$$\{H_k, \mathcal{S}_{BDI}\} = 0 \quad \Rightarrow \quad \begin{cases} [\boldsymbol{\lambda}_k\cdot\boldsymbol{\sigma}, \hat{d}\cdot\boldsymbol{\sigma}] = 0 \\ \{\boldsymbol{\epsilon}_k\cdot\boldsymbol{\sigma}, \hat{d}\cdot\boldsymbol{\sigma}\} = 0 \end{cases}. \tag{8.18}$$

Since $\left[\epsilon_k^0\sigma_0, \hat{d}\cdot\boldsymbol{\sigma}\right] = 0$, the condition (8.18) trivially reduces to:

$$\left[\boldsymbol{\lambda}_k\cdot\boldsymbol{\sigma}, \hat{d}\cdot\boldsymbol{\sigma}\right] = 2i\boldsymbol{\sigma}\cdot(\boldsymbol{\lambda}_k\wedge\hat{d}) = 0 \quad \Rightarrow \quad \boldsymbol{\lambda}_k \parallel \hat{d}, \tag{8.19}$$

$$\left\{\boldsymbol{\epsilon}_k\cdot\boldsymbol{\sigma}, \hat{d}\cdot\boldsymbol{\sigma}\right\} = 2\sigma_0\boldsymbol{\epsilon}_k\cdot\hat{d} = 0 \quad \Rightarrow \quad \boldsymbol{\epsilon}_k \perp \hat{d}. \tag{8.20}$$

These conditions restrict the spin-dependent terms in order to maintain chirality. Finally, it is worth noting that chiral symmetry is only globally realized if $\boldsymbol{\epsilon}_k \perp \hat{d}$, $\forall k$, since the $k$-dependency can result in sweet spots for specific values of $k$ due to competition between $\mathbf{B}$ and $\mathbf{C}$.

To conclude this section, we remark that, although this construction has been explicitly carried out on the example of spinful systems, a system with any two internal degrees of freedom is described by the same mathematical model, thus, presenting the same "topology", *i.e.*, two fibers with the same group structure. Therefore, a spinless system with two bands described in terms of Pauli matrices admits a similar Hamiltonian formulation and invariance under the same hidden symmetry operators, as we demonstrated in a previous work.[142]

In the following, we generalize this approach to obtain a BDI chiral symmetry for the case in which the system has $n$ internal degrees of freedom. We start by considering the general Hamiltonian as a sum of two terms:

$$H_k = H_k^{(0)} + H_k^{SC}, \tag{8.21}$$

where $H_k^{SC} = \tau_\phi \otimes \Delta_k$ is term containing the superconducting order parameter $\Delta_k$ and $H_k^{(0)}$ is the sum of all other terms. Next, in order to satisfy (8.5), we enforce that $\{\mathcal{S}, H_k^{SC}\} = 0$

by making $\mathcal{S} \propto \tau_{\phi+\pi/2} \otimes \Delta_k$ and then imposing the necessary constraints on $H_k^{(0)}$ so that $\{H_k^{(0)}, \mathcal{S}\} = 0$. Finally, we discuss the application of these ideas to a spinfull 2-band Kitaev chain.

### 8.3.2 General construction of a Kitaev chain with $n$ internal degrees of freedom

The conditions derived in Sec. 8.3.1 for the chiral operator originally introduced by Dumitrescu *et al.*[140] raises the question of whether it is possible to find similar hidden symmetries for systems with a richer spinorial structure. The idea is to consider a Hamiltonian which is an element of $SU(2) \times SU(n)$ (particle hole + other degrees of freedom). It is also necessary to introduce a generalized Nambu representation $\psi_k = (c_k, \mathcal{T}c_k)^T$, where $c_k$ is an element of the spinor representation of $SU(n)$. Although the construction of $\mathcal{T}$ is highly dependent on the physical meaning attributed to $SU(n)$ and its representation, some general ideas can be discussed without choosing a specific representation of $\mathcal{T}$. In the next section we will discuss in more details this representation choice for a specific algebra.

Since the Hamiltonian is an element of $SU(2) \times SU(n)$, the action of any (pseudo-)time-reversal operator $\mathcal{T} = U_\mathcal{T}\mathcal{K}$ ($U_\mathcal{T}$ is unitary and $\mathcal{K}$ denotes the complex conjugation) on the generators of $SU(n)$ divides it in one symplectic subgroup[163]

$$\mathcal{T} t_a^S \mathcal{T}^{-1} = -t_a^S, \tag{8.22}$$

and one antisymplectic

$$\mathcal{T} t_a^A \mathcal{T}^{-1} = t_a^A. \tag{8.23}$$

Another important point to consider for correctly implementing the Nambu representation is the effect of $\mathcal{T}$ on the $k$-dependency of the Hamiltonian. Thus, we divide the possible terms in symmetric

$$\mathcal{T} \epsilon_k^a \mathcal{T}^{-1} = \epsilon_k^a \tag{8.24}$$

and antisymmetric

$$\mathcal{T} \lambda_k^a \mathcal{T}^{-1} = -\lambda_k^a \tag{8.25}$$

under $\mathcal{T}$. Taking into account these two effects of the action of $\mathcal{T}$, we propose a general Nambu Hamiltonian

$$H_k = \tau_3 \otimes (\epsilon_k^a t_a^A + \lambda_k^a t_a^S) + \tau_0 \otimes (\epsilon_k^a t_a^S + \lambda_k^a t_a^A) + \tau_\phi \otimes d_k^a \tilde{t}_a \sin k, \tag{8.26}$$

where $\tilde{t}_a$ are the generators of $SU(n)$ such that $U_\mathcal{T}\tilde{t}_a$ are symmetric matrices.[d]

Now we can introduce a hidden chiral symmetry operator similar to the one introduced by Dumitrecu *et al.*[140] for spinfull systems:

$$\mathcal{S}_{BDI} = \tau_{\phi+\pi/2} \otimes \hat{d}^a \tilde{t}_a \tag{8.27}$$

[d] For example, in the $SU(2)$ case, $U_\mathcal{T} = i\sigma_2$, as explicitly written in (8.9). We note, nonetheless, that changing the spinor representation from the usual to the Nambu removes $U_\mathcal{T}$.

where $\hat{d}^a$ is the normalized $d^a$ vector such that $\mathcal{S}_{BDI}^2 = \mathbb{1}$. Finally, the condition for the existence of chiral symmetry, *i.e.*, $\{H_k, \mathcal{S}_{BDI}\} = 0$, implies

$$[\epsilon_k^a t_a^A + \lambda_k^a t_a^S, \hat{d}^b \tilde{t}_b] = 0, \tag{8.28}$$

$$\{\epsilon_k^a t_a^S + \lambda_k^a t_a^A, \hat{d}^b \tilde{t}_b\} = 0. \tag{8.29}$$

These conditions result in a series of constraints on the Hamiltonian, which are analogous to the locking conditions on the spin space obtained in Sec. 8.3.1. The chiral operator prohibits some of the coefficients $\epsilon_k^a$ and $\lambda_k^a$ multiplying the generators of $SU(n)$, *i.e.*, the isospin-dependent terms are locked. However, the geometric interpretation is not completely analogous. The reason lies in the algebraic structure of $SU(n)$ for an arbitrary $n \geq 3$:

$$[t_a, t_b] = i f_{ab}^c t_c, \tag{8.30}$$

$$\{t_a, t_b\} = \frac{1}{2n}\delta_{ab} t_0 + g_{ab}^c t_c, \tag{8.31}$$

where some of the structure constants $f_{ab}^c$ are zero and some $g_{ab}^c$ are non-zero. Thus, the parallel and perpendicular conditions derived in Sec. 8.3.1 do not hold in general anymore.

Even though we obtained some general conditions for constructing the Hamiltonian and finding hidden chiral symmetries, it is not clear how to apply these results without a specific choice of representation. Thus, we now provide a concrete discussion considering a spinful 2-band system.

### 8.3.3 The spinful 2-band Kitaev chain and its chiral symmetries

Following the construction of a Kitaev chain with an arbitrary number of degrees of freedom presented in Sec. 8.3.2, we propose a general Hamiltonian for a spinfull Kitaev chain with two bands. The Hamiltonian is now an element of $SU(2) \times SU(4) \cong SU(2) \times SU(2) \times SU(2)$. Denoting the spin (band) subspace by the matrices $\sigma_\nu$ ($\rho_\nu$), and taking $\mathcal{T} = i\sigma_2 \otimes i\rho_2 \mathcal{K}$, it is straightforward to obtain

$$\begin{aligned} H_k = \tau_3 \otimes (&\epsilon_k^{00}\sigma_0 \otimes \rho_0 + \epsilon_k^{ij}\sigma_i \otimes \rho_j + \lambda_k^{i0}\sigma_i \otimes \rho_0 + \lambda_k^{0i}\sigma_0 \otimes \rho_i) \\ + \tau_0 \otimes (&\lambda_k^{00}\sigma_0 \otimes \rho_0 + \lambda_k^{ij}\sigma_i \otimes \rho_j + \epsilon_k^{i0}\sigma_i \otimes \rho_0 + \epsilon_k^{0i}\sigma_0 \otimes \rho_i) \\ + \tau_\phi \otimes &d^{ij}\sigma_i \otimes \rho_j \sin k. \end{aligned} \tag{8.32}$$

Next, we consider the necessary conditions to have the hidden chiral symmetry:

$$\mathcal{S}_{BDI} = \tau_{\phi+\pi/2} \otimes \hat{d}^{ij}\sigma_i \otimes \rho_j, \tag{8.33}$$

where $\hat{d}^{ij}$ is normalized so that $\mathcal{S}_{BDI}^2 = \mathbb{1}$. It is evident that $\epsilon_k^{00}$ cannot break chirality, whereas $\lambda_k^{00}$ must be always zero for $\mathcal{S}_{BDI}$ to be preserved, *i.e.*, $\{H_k, \mathcal{S}_{BDI}\} = 0$. After

collecting the terms with the same matrix structure of the superconducting order parameter, *i.e.*, all terms proportional to $\sigma_i \otimes \rho_j$, the conditions (8.28) and (8.29) lead to

$$\epsilon_k^{ij} \hat{d}^{ab} \varepsilon_{ia}^n \varepsilon_{jb}^m = 0, \tag{8.34}$$

$$\lambda_k^{ij} \hat{d}^{ij} = 0. \tag{8.35}$$

Here, $\varepsilon_{ia}^n$ denotes the totally antisymmetric Levi-Civita tensor in three dimensions. For these terms, the analogy with Sec. 8.3.1 is direct, because in this case $f_{ab}^c$ are always non-zero and $g_{ab}^c$ are always zero.

To corroborate the results (8.34) and (8.35) regarding the locking conditions imposed by the superconducting order parameter $\hat{d}^{ab}$, we have performed independent numerical simulations with the KWANT package.[125] For simplicity, we implemented the following representative Hamiltonian:

$$H_k = \tau_3 \otimes (\epsilon_k \sigma_0 \otimes \rho_0 + m\sigma_\theta \otimes \rho_\gamma) + \tau_\phi \otimes \Delta\sigma_1 \otimes \rho_2 \sin k, \tag{8.36}$$

where $\epsilon_k = -\mu - 2t\cos k$, $\sigma_\theta = \sigma_1 \sin\theta + \sigma_3 \cos\theta$ and $\rho_\gamma = \rho_1 \sin\gamma + \rho_2 \cos\gamma$. Chiral symmetry $S_{BDI} = \tau_{\phi+\pi/2} \otimes \sigma_1 \otimes \rho_2$ should be preserved if, and only if, $\sigma_\theta = \pm\sigma_1$ and $\rho_\gamma = \pm\rho_2$. Therefore, varying the angles $\theta$ and $\gamma$ may lead to the appearance of minigap states when chiral symmetry is broken and of Majorana zero modes when the chirality condition holds. This behavior is explicitly confirmed by Fig. 9. For $\gamma = 0$ and $\sigma_\theta = \pm\sigma_1$, the minigap closes. However, for $\gamma \neq 0$, chiral symmetry is broken for any value of $\theta$ and the minigap only closes when accidental degeneracy emerges. Nonetheless, there is no topological protection in the latter case.

Figure 9 – Eigenvalues (in units of $t$) for a system described by the Hamiltonian (8.36) with 100 lattice positions as a function of $\theta$: (a) $\mu = 0$, $\Delta = 0.75t$, $m = 0.5t$, $\gamma = 0$; (b) $\mu = 0$, $\Delta = 0.75t$, $m = 0.5t$, $\gamma = \frac{\pi}{16}$. Non-zero values of $\gamma$ open minigap states for all values of $\theta$, except when breaking chiral symmetry leads to hotspots of zero energy minigap states which are not topologically protected.

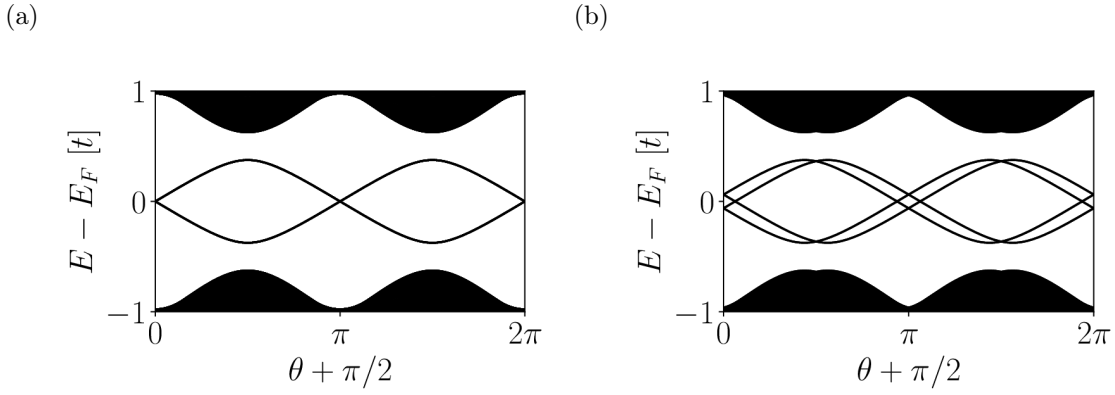


Source: author.

For the Hamiltonian (8.36), it is also possible to count the number of Majorana zero modes by calculating the winding number. In Fig. 10(a), we show the effect of varying $\mu$ and $m$ on the number of Majorana pairs. As expected, four Majorana pairs are possible. If we increase the absolute values of $\mu$ or $m$, the overlap between these zero modes eventually leads to their annihilation, resulting in lower winding numbers. Finally, we remark that only even winding numbers appear in the phase diagram of Fig. 10(a), which is a feature of a symmetry between spin and band subspaces. This condition will be broken next.

Figure 10 – Winding number for a 2-band spinful Kitaev chain. (a) Diagram obtained from Hamiltonian (8.36) as a function of $\mu$ and $m$ in units of $t$ with $\Delta = 0.75t$, $\theta = \pi/2$ and $\gamma = 0$. The highlighted points (in red colour) indicate the origin of the diagrams (b) and (c). (b) Diagram obtained from Hamiltonian (8.41) with $\Delta = 0.75t$, $\theta = \pi/2$, $\gamma = 0$ and $\mu = 0.5$, m= 0.5. (c) Diagram obtained from Hamiltonian (8.41) with $\Delta = 0.75t$, $\theta = \pi/2$, $\gamma = 0$ and $\mu = 2.5$, m= 2.5. It is evident that breaking spin-band degeneracy leads to phases with an odd number of Majorana pairs.

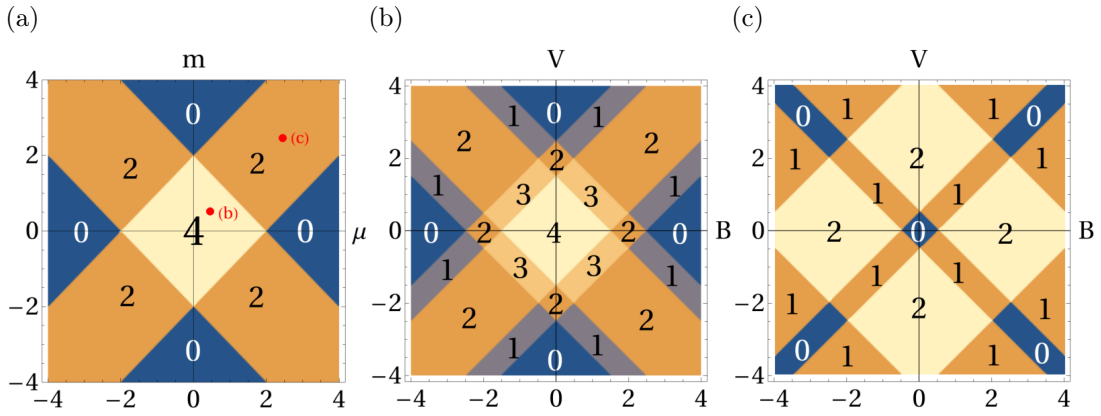


Source: author.

We now consider in more details the influence of the terms proportional to $\sigma_i \otimes \rho_0$ and $\sigma_0 \otimes \rho_i$. One can check that chiral symmetry requires:

$$\lambda_k^{i0} \hat{d}^{ab} \varepsilon_{ia}^{n} = 0, \tag{8.37}$$

$$\lambda_k^{0i} \hat{d}^{ab} \varepsilon_{ib}^{m} = 0, \tag{8.38}$$

$$\epsilon_k^{i0} \hat{d}^{ib} = 0, \tag{8.39}$$

$$\epsilon_k^{0i} \hat{d}^{ai} = 0. \tag{8.40}$$

It is interesting to note that the previous conditions (8.19) and (8.20) to maintain chiral symmetry on spinfull systems still hold. Namely, (8.37) implies that $\hat{d}^{ib}$ should be parallel to $\lambda_k^{i0}$ and (8.39) means that $\hat{d}^{ib}$ needs to be perpendicular to $\epsilon_k^{i0}$. Also, analogous results (8.38) and (8.40) hold for band degrees of freedom. Numerical simulations breaking these conditions on the band subspace also resulted on the appearance of minigap states, similar to the ones seen in Fig. 9.

To evaluate the effect of breaking spin-band degeneracy on the topological phase diagram, we added some of these four terms to the Hamiltonian (8.36) according to:

$$H_k \to H_k + \tau_0 \otimes (B\sigma_3 \otimes \rho_0 + V\sigma_0 \otimes \rho_1). \tag{8.41}$$

Here, $B$ denotes a Zeeman field along the $z$-axis and $V$, an analogous contribution to the band subspace, but along the $x$-direction. As expected, odd winding numbers also appear as indicated in Figs. 10(b) and 10(c). Hence, the system can indeed host any integer number of Majorana bound states from 0 to 4. Figure 10(c) deserves some special care regarding the value of the winding number at the origin. As a matter of fact, in spite of what the diagram may suggest, exactly at the origin, *i.e.*, for $B = V = 0$, $w = 2$, as consistency with Fig 10(a) requires.

Finally, there remains to take into account the effects of $k$-dependent terms, such as Rashba spin-orbit couplings, on the phase diagram. Interestingly, adding such terms to the hamiltonian (8.41) do not change the topological phase diagrams in Fig. 10. Thus, indicating that the Majorana modes are insensitive to them. Nevertheless, for finite systems, the presence of $k$-dependent terms leads to the appearance of minigap states due to the hybridization of Majorana end states, which became clearer as we shortened the chain.

### 8.3.4 Topological classification of quantum Hall graphene/superconductor devices

We now consider how the extra terms of the effective Hamiltonian (7.15) affect the emergence of Majorana modes. Using the same representation of (7.17), the effective Hamiltonian (7.15) reads:

$$\mathfrak{H}_{\text{eff}} = \tilde{\mu}\ \kappa_3 \otimes \eta_0 + \delta\tilde{\mu}\ \kappa_0 \otimes \eta_1 + w\ \tau_1 \otimes \eta_0 + \tilde{v}p_x\ \tau_3 \otimes \eta_1 - b_\theta \kappa_0 \otimes \eta_3. \tag{8.42}$$

Interestingly, if we compare (8.42) to the Hamiltonian of a topological superconducting ferromagnetic nanowire:[116]

$$H_{\text{ferr}} = [tp_x^2 - (\mu + 2t)]\sigma_0 \otimes \tau_3 + [\Delta_s\ \sigma_0 + p_x \mathbf{d} \cdot \boldsymbol{\sigma}] \otimes \tau_1 + \mathbf{V} \cdot \boldsymbol{\sigma} \otimes \tau_0, \tag{8.43}$$

where $t$ is the hopping constant, $\mu$ is the chemical potential, $\Delta_s(\mathbf{d})$ is an $s(p)$-wave superconducting order parameter, $\mathbf{V}$ is the Zeeman term and the matrices $\tau_\alpha$ and $\sigma_\alpha$ designate particle-hole and spin spaces, respectively, we find the following correspondence:

$$t = d_1 = d_2 = V_2 = 0, \tag{8.44}$$

$$\mu \leftrightarrow b_\theta, \tag{8.45}$$

$$\Delta_s \leftrightarrow \delta\tilde{\mu}, \tag{8.46}$$

$$d_3 \leftrightarrow \tilde{v}, \tag{8.47}$$

$$V_1 \leftrightarrow w, \tag{8.48}$$

$$V_3 \leftrightarrow \tilde{\mu}. \tag{8.49}$$

Thus, we can conclude that the system described by the effective Hamiltonian (8.42) has a charge-conjugation-like symmetry, described by an anti-unitary operator that anticommutes with the Hamiltonian.[43] On the other hand, $w$ and $\tilde{\mu}$ explicitly break any pseudo-time-reversal symmetry, described by anti-unitary operators that commute with the Hamiltonian and square to $-\mathbb{1}$.[140,116] Finally, there is a pseudo-time-reversal symmetry, described by some anti-unitary operator that commutes with the Hamiltonian and squares to $+\mathbb{1}$, that is explicitly broken for non-zero $\tilde{\mu}$.[140,116,164] Therefore, for disordered interfaces, corresponding to non-zero $w$ and $\tilde{\mu}$, only the charge-conjugation-like symmetry is preserved and the system is in D class.[43]

## 8.4 Summary

One-dimensional $p$-wave systems with an arbitrary number of internal degrees of freedom allow the emergence of a variable number of zero energy Majorana excitations at both ends, if a BDI chiral symmetry is preserved. In this chapter, we have shown that a hidden chiral symmetry can be derived from the superconducting terms in the Hamiltonian and provided a geometrical interpretation of the constraints imposed on systems that preserve it. This condition restricts the isospin-dependent terms of the Hamiltonian by restricting the possible adjoint elements of the $SU(n)$ representation.

We examined in detail the consequences of this severe restriction imposed on BDI systems for a spinful 2-band $p$-wave superconductor, in particular, showing that breaking chiral symmetry leads to the emergence of minigap states, that the winding number can assume the values between 0 and 4 and, finally, that odd values of the winding number are only possible when the spin-band degeneracy is broken.

We reviewed the topological classification of quantum Hall graphene/superconductor devices by mapping the effective Hamiltonian (7.15) to the Hamiltonian describing a superconducting ferromagnetic nanowire. The presence of interface potentials breaks all discrete symmetries but charge-conjugation. Hence, there is only one non-trivial topological phase possible corresponding to the class D.

# 9 Mechanisms of Andreev reflection in quantum Hall graphene

*Isn't it enough to see that a garden is beautiful without having to believe that there are fairies at the bottom of it too?*

Douglas Adams, The Hitchhiker's Guide to the Galaxy

In this chapter, we perform realistic simulations of a hybrid superconductor-graphene device in the quantum Hall regime to indentify the origin of downstream resistance oscillations in a recent experiment [Zhao *et. al.* Nature Physics 16, (2020)]. A comparison between the simulations and the experimental data suggests that disorder-induced intervalley scattering at the normal-superconductor (NS) interface can be the dominant cause of oscillations. We also show conductance oscillations due to additional edge states on clean interfaces with Fermi level mismatch. However, the regular pattern as a function of external parameters is not visible in the presence of disorder. The results presented in this chapter provide a way to qualitatively probe the quality of NS interfaces on multiterminal quantum Hall devices.

## 9.1 Introduction

Already starting in the early years of graphene, researchers were able to fabricate and measure high quality graphene–superconductor devices.[84,85] The ease of fabrication inspired a plethora of works, including: tunneling spectroscopy,[87,88] Josephson effect,[85,90,91,89], multiple Andreev reflections,[92] imaging Andreev scattering,[95] quantum phase transitions,[96,97] reflectionless tunneling,[30] microwave circuits,[98] and bolometer devices.[99] Because quantum Hall effect in graphene manifests already at relatively low magnetic fields below 1T, graphene is also uniquely fit to combine quantum Hall physics with superconductivity and Andreev reflection.[46,42,47,100]

Because boundary conditions favors the population of one sublattice[165,58] and the lowest Landau level states are valley-sublattice locked,[165,48] edge states in quantum Hall graphene are valley-polarized. The boundary of graphene and a superconductor converts electrons to holes with opposite valley isospin and, therefore, generates nonlocal Andreev

The content of this is chapter has been previously submitted as a preprint as Antonio L. R. Manesco, I. M. Flór, C.-X. Liu, and A. R. Akhmerov, *Mechanisms of Andreev reflection in quantum Hall graphene*, arXiv:2103.06722.

reflections. The combination of valley-sublattice locking with nonlocal Andreev reflection makes conductance depend solely on the device geometry (see Sec. 9.3 for details).[56] If the two edges connected to the superconductor are parallel, as depicted in Fig. 11 (a), the conductance between the two normal leads is[56]

$$G_{xx} = -\frac{2e^2}{h}, \tag{9.1}$$

where $e$ is the electron charge and $h$ is the Planck constant.

Figure 11 – (a) An example device for probing nonlocal Andreev reflection in graphene. The device has 3-terminals: two normal leads (grey) and a superconducting lead (blue). Both graphene edges connected with the superconducting lead are zigzag, which mimics the valley polarization of a generic graphene boundary. The interface can be either armchair (main figure) or zigzag (inset). (b) The measured downstream resistance $\widetilde{R}_{xx}$ as a function of the magnetic field $B$ and the gate voltage $V_G$ in a multi-terminal setup [courtesy of Zhao *et. al.*. Zhao *et al.* (42)] The regions with filling factor $\nu = 1$ and $\nu = 2$ are highlighted.

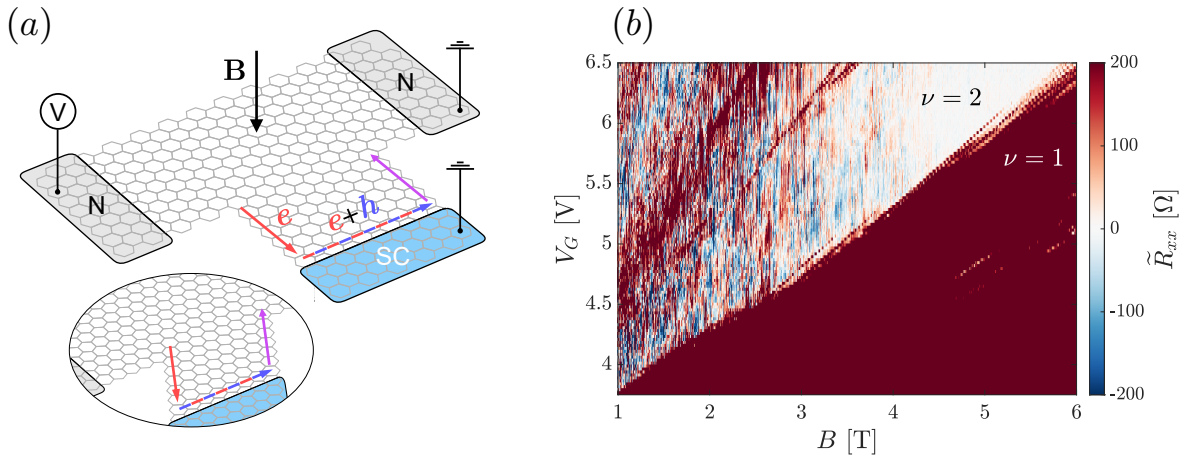


Source: author.

Contrary to the prediction from the theory with idealized conditions,[58] a recent work observed downstream resistance oscillations in a multiterminal device as a function of the magnetic field and the gate voltage, shown in Fig 11 (b). The authors have interpreted the data as chiral Andreev edge states interference, supported by tight-binding calculations.[42]

Our goal is to investigate Andreev states interference and identify its possible origins. We identified three mechanisms leading to deviations from constant conductance. We start by following Zhao *et. al.*[42] and study the Andreev interference created by the lattice mismatch. Interference, in this case, is highly dependent on the interface orientation, due to the small intervalley coupling. We then consider short-range disorder (Sec. 9.5) and show that the larger momentum transfer results in irregular oscillations between normal and Andreev reflections at any interface orientation. Finally (Sec. 9.6), we demonstrate

that a sufficiently high Fermi level mismatch generates additional edge states and lead to interference by means of intravalley scattering.

All three mechanisms produce conductance fluctuations, albeit with different characteristics. Lattice and Fermi level mismatch at perfect interfaces generate a regular interference pattern in nonlocal conductance due to the translational invariance of the Hamiltonian. An irregular interference pattern, like the one observed in experiment, occurs only in the presence of strong disorder. We compare the results with experimental data and discuss the relevance of our findings in Sec. 9.8.

## 9.2 Tight-binding model

From this section on, we present numeical results obtained with tight-binding calculations using the Kwant package.[125] The Hamiltonian reads

$$\mathcal{H} = \sum_i \psi_i^\dagger(\Delta_i\tau_x - \mu_i\tau_z)\psi_i - \sum_{\langle i,j\rangle} \psi_i^\dagger(t_{ij}e^{i\tau_z\phi_{ij}}\tau_z)\psi_j, \tag{9.2}$$

where $\psi_i = (c_i, c_i^\dagger)^T$, $c_i^\dagger$ and $c_i$ are the electron creation and annihilation operators at the position $\mathbf{r}_i$, and $\langle i,j\rangle$ are all the pairs of nearest neighbor sites. We simulate the interface by using the following position dependence of the chemical potential $\mu_i$ and the superconducting pairing potential $\Delta_i$:

$$\mu_i = (\mu_{SC} - \mu_{QH})f(\mathbf{r}_i) + \mu_{QH}, \quad \Delta_i = \Delta\Theta(x_i), \quad f(\mathbf{r}_i) = \frac{1}{2}\left[1 + \tanh\left(\frac{x_i}{\chi}\right)\right], \tag{9.3}$$

with $\mu_{QH}$ and $\mu_{SC}$ the onsite energies at the normal and the superconducting region. The hopping energies $t_{ij} = t$ are constant in the honeycomb crystal structure, and equal to $t_{ij} = t/2$ in the square lattice that we use to simulate a lattice mismatch with the superconductor. The Peierls phase is:

$$\phi_{ij} = -\frac{\pi B}{\phi_0}(y_j - y_i)(x_j + x_i)\Theta\left(\frac{x_i + x_j}{2}\right), \tag{9.4}$$

where $B$ is the orbital magnetic field, $\phi_0 = h/e$ is the magnetic flux quantum, and $\Theta(x)$ is the Heaviside step function. The model is rescaled as $a \mapsto \tilde{a} = sa$ and $t \mapsto \tilde{t} = t/s$ to reduce the computational cost keeping the Fermi velocity $v_F \propto ta$ unchanged.[166] In all transport calculations, we use $t = 2.8\,\text{eV}$, $a = 0.142\,\text{nm}$,[54] $s = 10$, $\Delta = 1.3\,\text{meV}$ in order to match the MoRe pairing potential,[42] and we choose $\chi = 50\,\text{nm}$ to match, in order of magnitude, electrostatic estimations in a similar system.[86] On band structure calculations we take $\Delta = 0.05t$ and a square superconductor to better visualize the data. Unless stated

otherwise, the superconducting region has a honeycomb structure. The $\tau_i$ Pauli matrices, in the usual representation, act on electron-hole spinor components.

The code and data used to produce the figures and derive the effective model are available in Zenodo.[167] We use Adaptive[168] to efficiently sample $k$-space on bandstructure calculations.

## 9.3 Valley-dependence of Andreev reflection

Andreev reflection is a process in which an incoming charge carrier is reflected back as its time-reversal partner. In graphene, it means that electrons are converted to holes in the opposite valley.[93,91] Thus, a correlation between charge and valley densities is expected. Moreover, boundary conditions applied to graphene's lowest Landau level result in valley-polarized edge modes.[48,58] We can observe both phenomena by computing the local values of valley and charge densities, as shown in Fig. 12. Here we compute the valley density as the expectation value of the anti-Haldane operator, $V$.[169,170a] In the presence of a magnetic field, we introduce a Peierls phase correction $\phi_{ij}(B)$:

$$V(B) = \frac{i}{3\sqrt{3}} \sum_{\langle\langle i,j \rangle\rangle} \eta_{ij} s_z^{ij} e^{i\phi_{ij}(B)} c_i^\dagger c_j, \tag{9.5}$$

where $\langle\langle i,j \rangle\rangle$ denotes a sum performed over the next-nearest-neighbors, $\eta_{ij} = \pm 1$ for a clockwise/anticlockwise hopping, and $s_z = \pm 1$ if $\mathbf{r}_i$ is in the A/B sublattice.

In a two-terminal setup with a NS interface, the longitudinal conductance in the lowest Landau level was previously shown to be:[56]

$$G_{NS} = \frac{2e^2}{h}(1 - \cos\Phi), \tag{9.6}$$

where $\Phi$ is the angle difference between the valley isospins of the states entering and leaving the superconductor, depicted in Fig. 13 (a). It turns out that $\Phi$ depends on the geometry, resulting in constant conductance with different values, as shown in Fig. 13 (b).

It is straightforward to compute the nonlocal conductance $G_{xx}$ of a 3-terminal device as the one depicted in Fig. 11. First, we take $\Phi = \pi$. Then, we notice that

$$G_{xx} = \frac{2e^2}{h} - G_{NS} = \frac{2e^2}{h}\cos\Phi, \tag{9.7}$$

leading to Eq. 9.1.

## 9.4 Andreev interference in clean graphene quantum Hall devices

The NS interface hosts two propagating Andreev states moving along a single direction (throughout the chapter we neglect spin physics). Linearizing the dispersion of

[a] Note that this operator has eigenvalues $\pm 1$ at the valley $K/K'$.

Figure 12 – (a) Valley, $\mathcal{V}(\mathbf{r}) = \langle \mathbf{r}|V(B)|\mathbf{r}\rangle$, and (b) charge, $\mathcal{C}(\mathbf{r}) = \langle \mathbf{r}| - \tau_z|\mathbf{r}\rangle$, densities near a NS interface ($x = 0$) with $B = 1T$ and $\mu = 0.075t$ in a graphene nanoribbon. It is visible that both incoming and outgoing modes are valley polarized and that charge and valley densities are highly correlated. The length is in units of nm (the honeycomb crystal in the backgound is just illustrative).

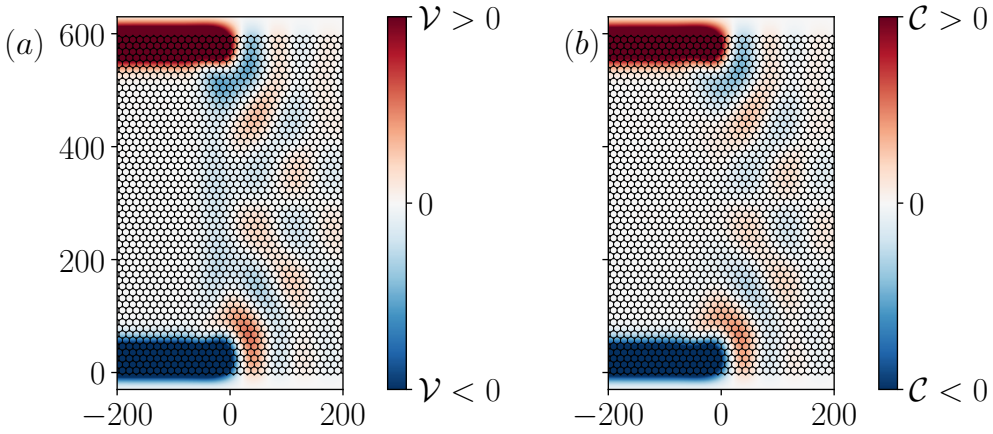


Source: author.

Figure 13 – (a) Incoming $\nu_i$ (solid) and outgoing $\nu_o$ (dashed) valley isospins on the Bloch sphere for zigzag (armchair) propagating modes in blue (red) in the case of a superconductor covering different edges in an NS junction. (b) $G_{NS}$ conductance plateaus in the lowest Landau level on a zigzag edge junction for several values of $\Phi$ realized with different arrangements of the superconductor on the junction.

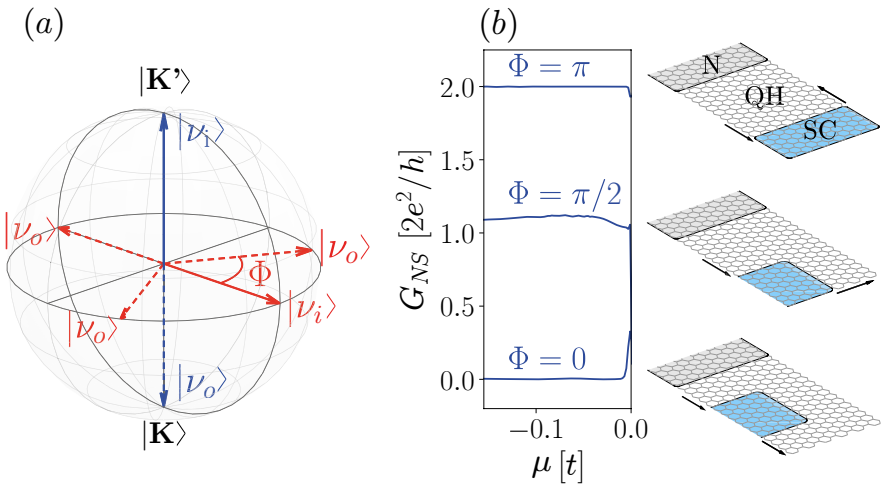


Source: author.

the two edge states near zero energy we obtain the edge state Hamiltonian

$$H_{\text{eff}} = \begin{pmatrix} v(k+k_0) & 0 \\ 0 & v(k-k_0) \end{pmatrix} = vk\sigma_0 + vk_0\sigma_z, \tag{9.8}$$

where $k$ is the momentum along the interface, and $v$ is the Fermi velocity of the propagating chiral modes (see Sec. B for a derivation). The projections of the valley momenta on the graphene-superconductor interface $\pm k_0$ depend on the lattice orientation: $k_0 = 0$ if the interface is along the armchair direction, while a general boundary orientation results in $k_0 \sim \pi/a$, with $a$ the graphene lattice constant. The Hamiltonian acts on $\Psi = (\psi_1, \psi_2)^T$ (presented in the Sec. B), where $\psi_1$ is a linear combination of electron states at valley $K$ and hole states at the valley $K'$, and $\psi_2$ is the opposite. The Pauli matrices $\sigma_0$ and $\sigma_{i=x,y,z}$ act on $\Psi$.

Intervalley coupling is added by the Hamiltonian

$$H_{\text{intervalley}} = m\sigma_x, \tag{9.9}$$

where $m$ is the coupling constant. The coupling between the two chiral edge states with $m$ leads to oscillations between normal and Andreev reflections as a function of the magnetic field and the gate voltage.[42] A sufficiently low value of $m \ll vk_0$ preserves the valley polarization. Estimating $m \sim vk_F$, the intervalley coupling is non-negligible only if $k_0 \lesssim k_F$. Therefore, conductance oscillations are visible only if the NS boundary is oriented withing angles $\lesssim k_F a \sim 1^\circ$ from the armchair direction.[171,57,165,58]

To confirm the absence of interference at clean (small $m$) NS interfaces with an arbitrary orientation, we simulate a 3-terminal setup with two different geometries depending on the NS interface: (a) armchair; (b) zigzag, as shown in Fig. 11. In both cases, the two edges connected with the superconductor are zigzag, therefore preserving the hypothesis for Eq. 9.1. The conductance between the two normal leads is computed as

$$G_{xx} = \frac{e^2}{h} \sum_{i,j} \left( T_{ee}^{ij} - T_{he}^{ij} \right), \tag{9.10}$$

where $T_{ee}^{ij}$ is the probability of an electron from channel $j$ in the source lead transmit as an electron to the channel $i$ in the drain lead and $T_{he}^{ij}$ is the probability of an electron transmit as a hole.

In this section, we follow[42] and use square superconductor, which weakly breaks valley conservation. With an armchair interface [Fig. 14 (a)], the conductance shows an interference pattern [Fig. 14 (c)]. Chiral modes at zigzag interfaces, on the other hand [Fig. 14 (b)], have constant nonlocal conductance [Fig. 14 (d)], in agreement with the analytical model.

We find that interference of chiral Andreev states is highly sensitive to the NS interface orientation. Moreover, conductance is expected to be constant for clean interfaces with arbitrary orientation.[56] Since it is unlikely that in the experiment[42] the NS interface has a perfect alignment with the armchair direction, we must consider other phenomena to explain the observed downstream resistance oscillations.

Figure 14 – Band structure of a NS ribbon with (a) armchair and (b) zigzag terminations with $\mu_{QH} = \mu_{SC} = 0.05t$, $B = 1T$. The opacity is the expectation value of $f(\mathbf{r}_i)$, defined on Eq. 9.3, with $\chi = 5$. We see that the positive velocity modes (chiral Andreev states) occur near $k = 0$ with armchair interfaces and are well-separated in momentum space for zigzag orientation. The resulting nonlocal conductance presents an interference pattern for armchair interfaces (c) while the expected constant value from Eq. 9.1 is obtained for zigzag interfaces (d).

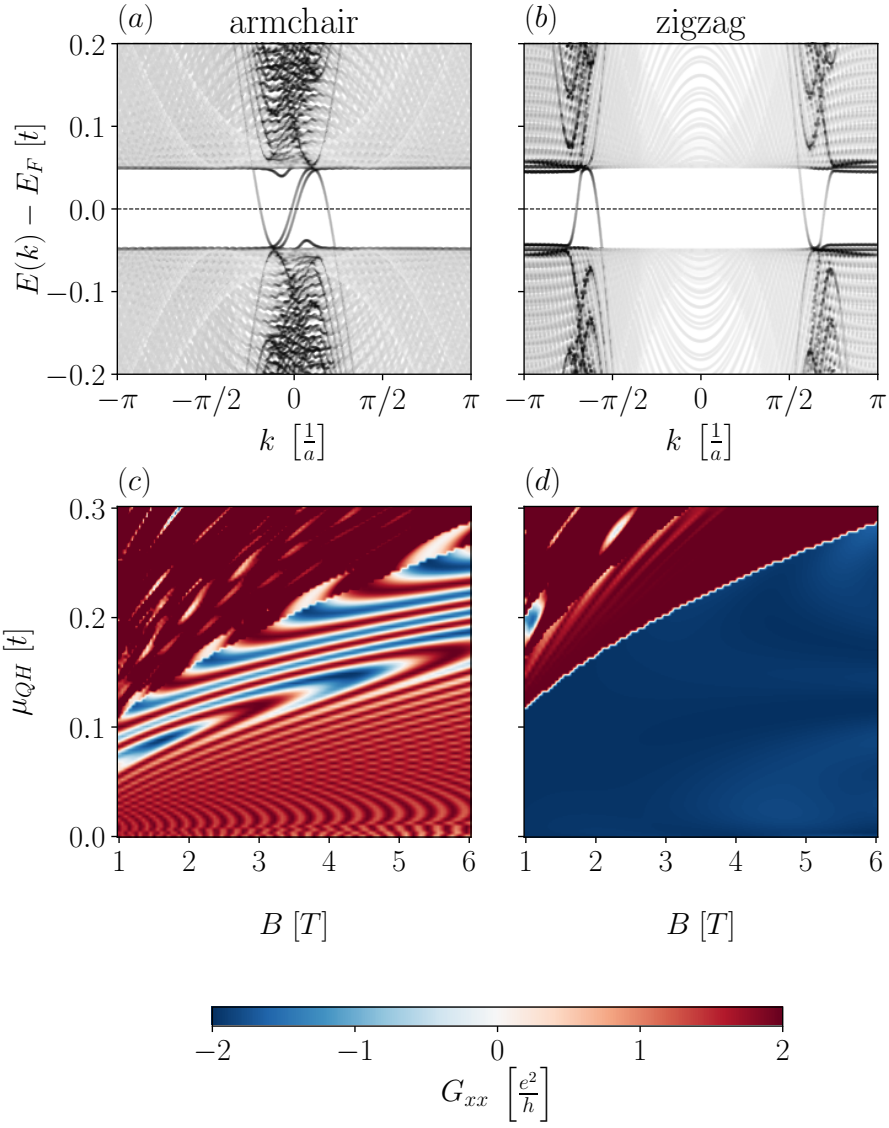


Source: author.

## 9.5 Effects of disorder

To increase the transition rate between the two chiral states, we add short-range disorder. The additional term in the Hamiltonian has the form of an uniformly-distributed uncorrelated onsite potential:

$$\mathcal{H}_{\text{disorder}} = \sum_i \psi_i^\dagger \left( \delta\mu_i^{(\text{edge})} + \delta\mu_i^{(\text{SC})} \right) \tau_z \psi_i, \tag{9.11}$$

with $\delta\mu_i^{(\text{edge})}, \delta\mu_i^{(\text{SC})} \in [-t, t)$, illustrated in Fig. 15 (a). The disorder region width in the quantum Hall region is 6 nm, such that it is always smaller than the magnetic length $l_B = \sqrt{\hbar/eB}$ within the magnetic field range considered.

Figure 15 – Effects of disorder on the downstream resistance. (a) Scheme of disorder landscape: blue represents $\delta\mu_i^{(\text{edge})}$; red represents $\delta\mu_i^{(\text{SC})}$. The resulting nonlocal conductance with finite $\delta\mu_i^{(\text{edge})}$ (b) is minor and the conductance is still nearly constant in a large area of the parameter space. When $\delta\mu_i^{(\text{SC})}$ is finite (c), however, the effects are much stronger and persistent for all $\mu$ and $B$.

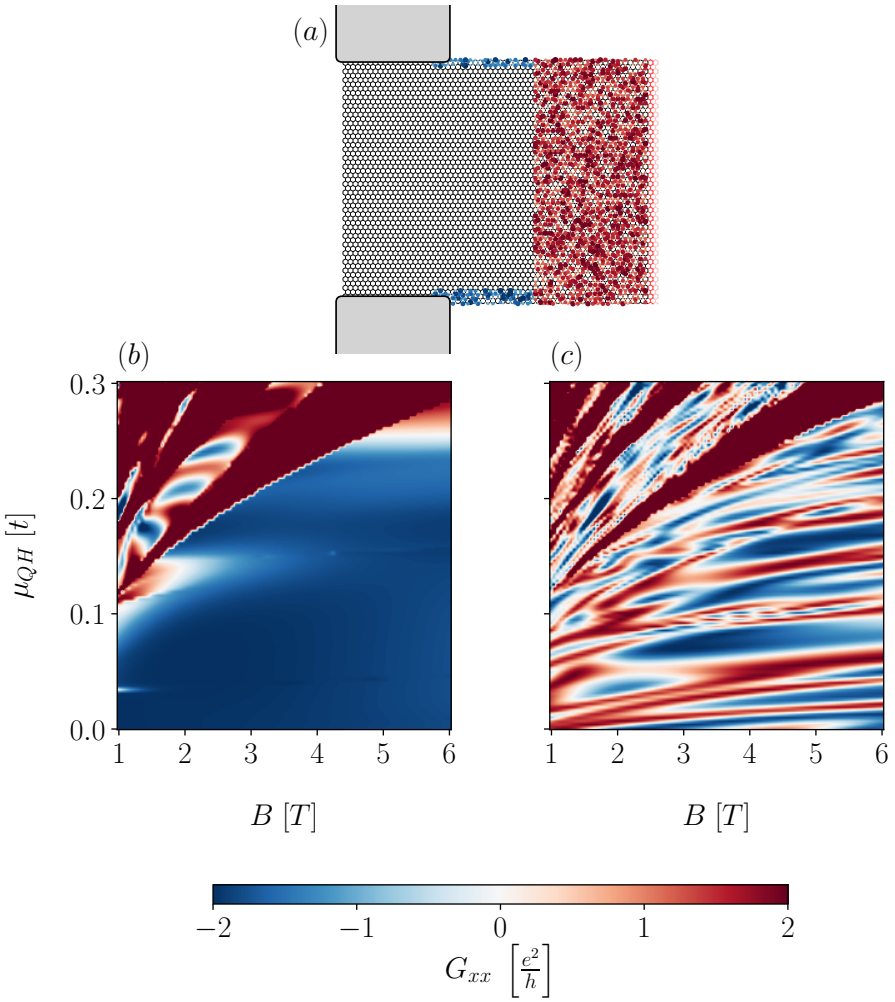


Source: author.

Although the effects disorder at the edges on the conductance are visible, nearly constant negative values are still visible on large portions of the parameter space [Fig. 15 (b)]. On the other hand, scattering caused by disorder along the NS interface leads to strong irregular oscillations (Eq. 9.1) for all $\mu_{QH}$ and $B$ [Fig. 15 (c)]. The conductance fluctuations with interface disorder are similar to Fig. 11 (b), suggesting that disorder in the superconducting region is the main cause of interference in the experiment.[42]

## 9.6 Effects of Fermi level mismatch

The superconductor on top of graphene transfers charge carriers to the underlying layer. Hence, there will be a Fermi level mismatch between the quantum Hall and the proximity-induced superconducting regions. The resulting potential landscape obtained via electrostatic simulations varies across tens of nanometers,[86] in contrast to previous theoretical works that consider an abrupt Fermi level change when compared to the other relevant length scales.[93,91] Such smooth variation, therefore, does not promote intervalley scattering.

An electrostatic potential shift near the NS interface locally changes the filling factor. Thus, extra bands cross the Fermi energy, as depicted in Figs. 16 (a), and Eq. 9.8 does not hold. Since incoming and outgoing modes connected with the superconductor couple with all Andreev states, the nonlocal conductance no longer depends only on valley polarization of edge states connected with the superconductor. Instead, we see an interference pattern, as depicted in Fig. 16 (b).

Figure 16 – (a) Band structure of a NS ribbon with Fermi energy mismatch ($\mu_{QH} = 0.1t$, $\mu_{SC} = 0.5t$, and $B = 1T$). The opacity is the same as in Fig. 14. One can clearly see the presence of extra non-chiral edge states. (b) Nonlocal conductance of a system with finite Fermi level mismatch ($\mu_{SC} = 0.5t$). There is a clear deviation from the predicted constant value of Eq. 9.1 due to the extra propagating modes.

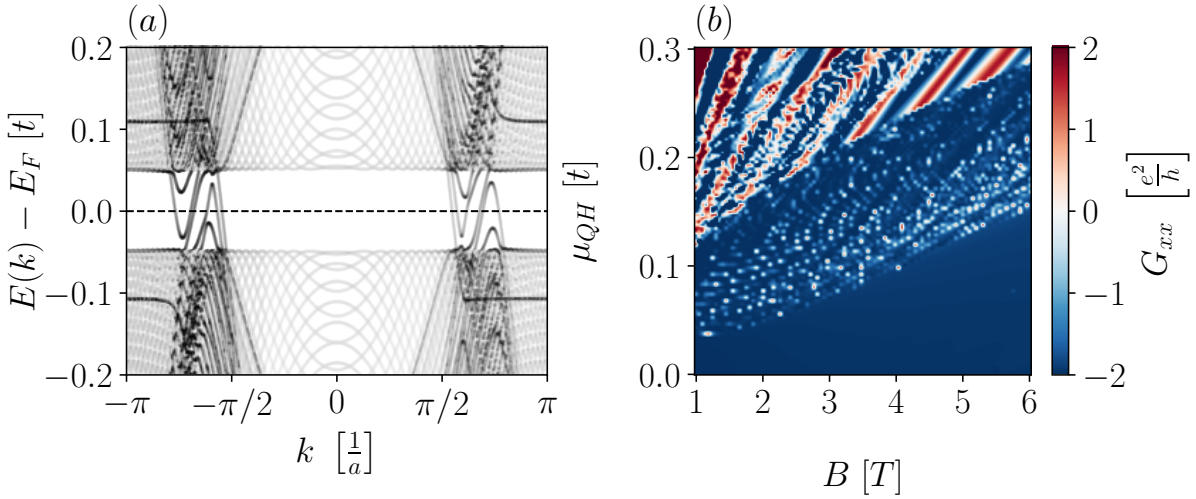


Source: author.

It is worth emphasizing that interference caused by Fermi level mismatch is independent on the quality of the NS interface. Disorder, however, hides the regular pattern. Therefore, the electrostatic-induced interference discussed in this section is observed only when the NS interface is clean.

## 9.7 Absorption of quasi-particle excitations by the superconudctor

The absorption of quasi-particles by the superconductor reduces the probability of outgoing electrons and holes at the end of the interface. We effectively add a "survival probability" $P_{\text{surv}}$ by modifying the system: we attach a metallic lead to the superconducting region such that quasiparticles can now tunnel through the superconductor with a finite probability. Thus, the nonlocal conductance change as[42]

$$\tilde{G}_{xx} = P_{\text{surv}} G_{xx} \tag{9.12}$$

where $G_{xx}$ is given by Eq. 9.7. Thus, the nonlocal conductance is suppressed, as seen in (Fig. 17, following experimental results.[42]

Figure 17 – (a) Quasiparticle tunneling to the superconductor suppresses the nonlocal conductance.

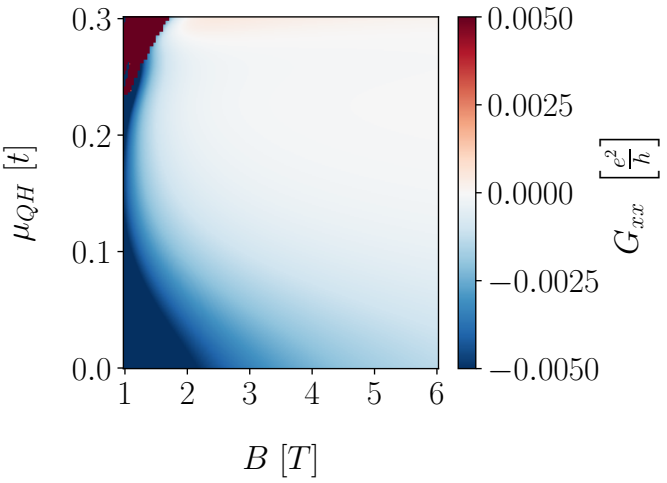


Source: author.

## 9.8 Experimental relevance

Our results help to establish a rigorous interpretation of the experiment by characterizing the NS interface quality. Irregular oscillations, similar to the experiment, were obtained with disorder at the NS interface. Thus, irregular sign changes in nonlocal transport measurements can be used as a way to check the quality of devices. This is not possible in the normal state due to the absence of backscattering in the quantum Hall regime. Clean devices, *e.g.*, with nearly transparent NS interfaces and edges defined by gate potentials, are expected to present nearly constant conductance or a regular oscillation pattern caused by Fermi level mismatch. The presence of vortices also plays an important role when interference is present by adding a phase factor along the interface.[42]

Otherwise, vortices just suppress the conductance due to quasiparticle tunneling through the superconductor, as discussed in the Sec. 9.7.

Recent experimental works[46,42,47] motivate the combination of quantum Hall effect and superconducting order in graphene as a platform for Majorana zero modes.[43] Our results cover two different situations that prevent the existence of a non-trivial topological phase: (i) the strong intervalley scattering caused by disorder closes the topological gap; (ii) Fermi level mismatch promotes the population of undesired edge states along the NS interface.[43,44] Therefore, fabrication of high-quality graphene/superconductor heterostructures is necessary, for example, using van der Waals materials such as $NbSe_2$.[86] Moreover, experimental routes to suppress the Fermi level mismatch together with electrostatic simulations are necessary to properly analyze the edge states population at the NS interface.

## 9.9 Summary

We reviewed three mechanisms responsible for a deviation from constant Andreev conductance on quantum Hall graphene devices. We verified that chiral Andreev edge states interference happens when the graphene orientation along the NS interface is armchair and are absent otherwise. The reason is the zero momentum separation between the chiral Andreev edge states on armchair interfaces, such that arbitrarily small intervalley coupling leads to interference. The perfect alignment with the armchair orientation, however, is unlikely to happen. We also found that scattering between the two edge states is created with short-range disorder, leading to irregular Andreev conductance oscillations that resamble the recent experimental data.[42] Finally, we found that, even with clean interfaces, the population of non-chiral edge states along the NS interface caused by Fermi level mismatch also leads to Andreev conductance oscillations. Our results provide a series of considerations necessary to properly interpret experiments and characterize the quality of devices. Furthermore, we argue that the intense search for Majorana physics in graphene quantum Hall devices require improvements in the NS interfaces' quality and proper understanding and control of the Fermi level mismatch.

# Part II

# Buckled graphene superlattices

# 10 Correlations in the elastic Landau level of spontaneously buckled graphene

*Yeah, b***h! Magnets!*

Jesse Pinkman, Breaking Bad

Electronic correlations stemming from nearly flat bands in van der Waals materials have demonstrated to be a powerful playground to engineer artificial quantum matter, including superconductors, correlated insulators and topological matter. This phenomenology has been experimentally observed in a variety of twisted van der Waals materials, such as graphene and dichalcogenide multilayers. Here we show that spontaneously buckled graphene can yield a correlated state, emerging from an elastic pseudo Landau level. Our results build on top of recent experimental findings reporting that, when placed on top of hBN or $NbSe_2$ substrates, wrinkled graphene sheets relax forming a periodic, long-range buckling pattern. The low-energy physics can be accurately described by electrons in the presence of a pseudo-axial gauge field, leading to the formation of sublattice-polarized Landau levels. Moreover, we verify that the high density of states at the zeroth Landau level leads to the formation of a periodically modulated ferrimagnetic groundstate, which can be controlled by the application of external electric fields. Our results indicate that periodically strained graphene is a versatile platform to explore emergent electronic states arising from correlated elastic Landau levels.

## 10.1 Introduction

One of the key features of graphene's electronic structure is that low-energy electrons behave as massless Dirac fermions.[53,54] Among the successful applications of this model, we can highlight the prediction of the so-called zeroth Landau level (ZLL) formed exactly at the Fermi energy,[63,54,48,59] in contrast to the well-known behaviour for systems with parabolic low-energy dispersion.[60,61,172] The high density of states resulting from the flat band dispersion leads to electronic instabilities at half-filling, *e.g.* the formation of canted antiferromagnetic ordering in the quantum Hall edge modes.[117,173,51,122,50,49]

The content of this is chapter has been previously published as Antonio L. R. Manesco, J. L. Lado, Eduardo V. S. Ribeiro, G. Weber, and D. Rodrigues Jr., *Correlations in the elastic Landau level of spontaneously buckled graphene*, 2D Mater. **8** 015011 (2021).

Interestingly, the emergence of Landau levels is not a unique consequence of orbital magnetic fields. They also appear when the system is subjected to *pseudo* magnetic fields (PMF) and their corresponding pseudo-axial gauge fields, for example, due to the presence of strain,[66,174–179] modulated interlayer hopping,[180] or interlayer bias.[170] In these artificial Landau levels, which also appear in twisted bilayer graphene systems displaying the so-called magic angle flat bands bands,[181,13,180,182] electronic instabilities are also present.[67,12,183–187,10] The emergence of correlations in van der Waals superlattices has also been reported in a variety of Moiré graphene multilayers[188,189] and Moiré dichalcogenide multilayers,[190,191] suggesting that van der Waals systems combining both graphene and dichalcogenides can provide an additional new platform for correlated physics.

Here we put forward a minimal graphene-based van der Waals multilayer system showing a correlated state, stemming from the emergence of localized modes associated to an elastic gauge field. Our results build on top of recent experimental reports regarding the formation of buckled graphene superlattices when the material is placed on top of hBN or $NbSe_2$ substrates.[15] Indeed, the experimental data shows the formation of Landau subbands with sublattice polarization – a distinctive signature of PMF, suggesting a low energy description realizing a periodically-modulated pseudo-axial gauge field.[15,192,15] Furthermore, electronic correlations were observed when tunning the system to half-filling,[15] consitent with the results showed in this paper.

We investigate the effects of electronic interactions in the pseudo Landau level of buckled graphene, showing the emergence of localized correlated states. In particular, we show the emergence of a periodically-modulated ferrimagnetic groundstate, realizing a magnetic honeycomb superlattice. We also consider the effects of charge doping, motivated by the possibility of gate-tuning graphene/hBN heterostructures, and spin-orbit coupling (SOC) due to the lack of inversion symmetry. The first shows optimal magnetization for half-filling, consistent with the correlation gap opening experimentally oberved,[15] while the second leads to a non-collinear ferrimagnetic ordering. Finally, we show that the presence of an external perpendicular electric field breaks the global sublattice symmetry as an effective mass in the superlattice scale, suppressing the magnetic ordering when this effective mass is comparable with the gap size.

The chapter is organized as follows. Sec. 10.2 is devoted to introducing the studied model. In Sec. 10.3, we present key results regarding the magnetic ordering and the effects of gate-tuning, SOC and an external electric field on the interacting system. Finally, in Sec. 10.4, we summarize our results.

## 10.2 The system

In this section, we consider a model for interacting electrons in graphene with a buckled superlattice, as depicted in Fig. 18 (a). The source code and data used to produce the figures in this chapter are available.[193] Our starting point is the nearest neighbour tight-binding model for a pristine graphene sheet:

$$\mathcal{H} = -t \sum_{s} \sum_{\langle i,j \rangle} c_{is}^{\dagger} c_{js} + U \sum_{i} c_{i\uparrow}^{\dagger} c_{i\uparrow} c_{i\downarrow}^{\dagger} c_{i\downarrow}, \tag{10.1}$$

where $c_{is}^{(\dagger)}$ annihilates (creates) electrons in the position $i$ with spin $s$. For the sake of lower computational costs, we rescaled the system according to the procedure described in[166,184,183]. Namely, we guarantee that the linear dispersion is preserved by fixing the Fermi velocity as $v_F \propto ta$, where $t$ is the hopping energy and $a$ is the lattice constant. Hence, we can change the lattice constant as $a \to \beta a$ as long as we compensate the hopping energy by making $t \to t/\beta$. We consider the effects of interactions by setting a finite value for the Hubbard constant $U$, which we rescale as $U \to U/\beta$ to fix the ratio $U/t$. Unless explicitly written, all the results presented in this paper were obtained for a supercell with $25 \times 25$ unit cells, corresponding to $\beta \sim 2 - 3$, considering the supercell lattice constant $L_M \sim 14 - 18nm$.[15] We also keep $U = t$ in all calculations, a conservative value compared with the DFT estimations of $U \approx 2t$[194] to ensure our results hold even if the strain is smaller than the observed values. The reduced Brillouin zone for the supercell is depicted in Fig. 18c. The interacting Hubbard term is solved at the mean-field level.

In the presence of strain, the lattice translational symmetry is broken. Therefore, we must relax the condition that the hopping energy $t$ (and $v_F$ as well) is a constant and consider three non-equivalent hopping energies, $t_i$, $i \in \{1, 2, 3\}$, as shown in Fig. 18 (b). We can parametrize them as

$$t_i = t + \delta t_i, \tag{10.2}$$

with $\delta t_i$ being the difference between the new hopping energy and the one for free-standing graphene.

The low-energy description obtained by substituting Eq. 10.2 into Eq. 10.1 corresponds to a modified Dirac Hamiltonian with an additional gauge field that depends on the new hoppings as:

$$A_x = \frac{\sqrt{3}}{2ev_F}(t_3 - t_2), \tag{10.3}$$

$$A_y = \frac{1}{2ev_F}(t_2 + t_3 - 2t_1). \tag{10.4}$$

For the system under investigation, the corresponding PMF landscape was obtained by a combination of charge distribution and Landau level spacing obtained from STM and is

Figure 18 – (a) Representation of the buckled graphene superlattice. The colors represent the magnitude of the PMF, Eq. 10.5 (red is for positive and blue for negative). (b) In the presence of strain, the three hopping energies of an arbitrary atom have their degeneracy broken and we distinguish them by indexing them as $t_i$, $i \in \{1, 2, 3\}$. (c) Representation (out-of-scale) of the reduced Brillouin zone for the supercell considered in this chapter (small hexagon) in comparison with the larger Brillouin zone obtained with graphene's crystal vectors (large hexagon). This reduced Brillouin zone is a consequence of the long-wavelength PMF. The high-symmetry points are represented with lowercase letters to distinguish them from graphene's original Brillouin zone high-symmetry points. (d) Valley flux for a system with a $25 \times 25$ supercell.

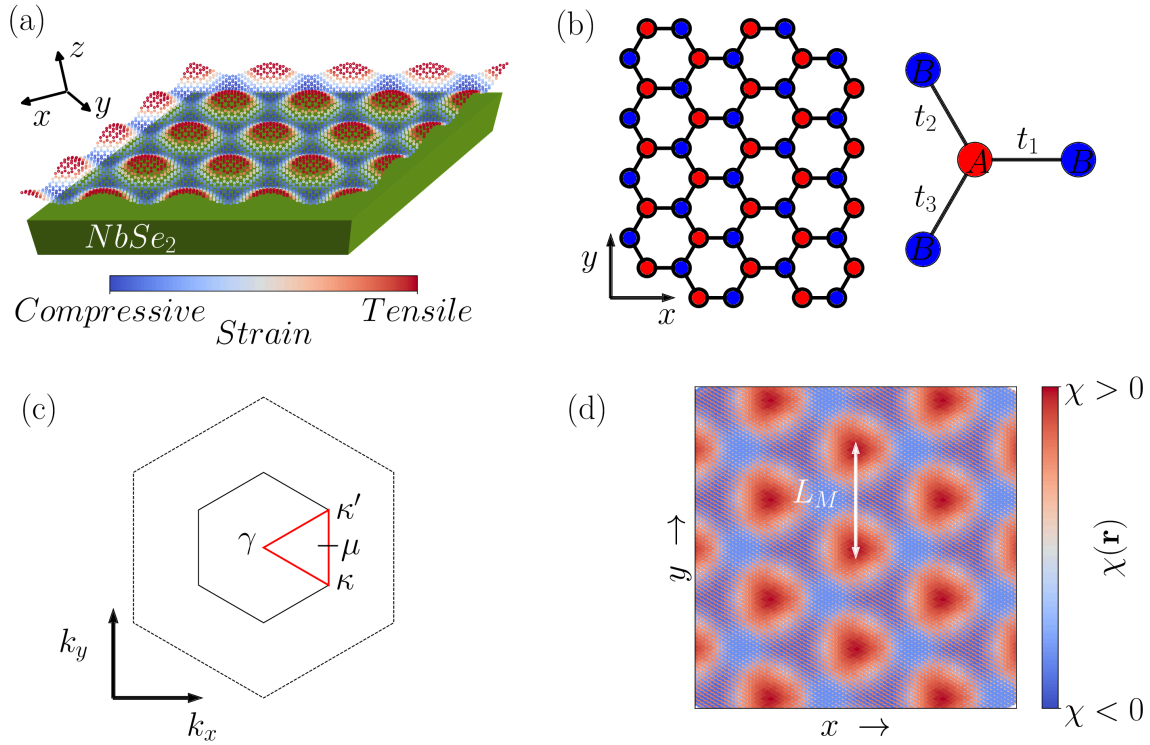


Source: author.

given by:[15,192,15]

$$B(\mathbf{r}) = B_{\text{eff}} \sum_{i=1}^{3} \cos(\mathbf{b}_i \cdot \mathbf{r}), \tag{10.5}$$

with

$$\mathbf{b}_1 = \frac{2\pi}{L_M}\left(-\frac{1}{\sqrt{3}}, 1, 0\right), \tag{10.6}$$

$$\mathbf{b}_2 = \frac{2\pi}{L_M}\left(\frac{2}{\sqrt{3}}, 0, 0\right), \tag{10.7}$$

$$\mathbf{b}_3 = \frac{2\pi}{L_M}\left(-\frac{1}{\sqrt{3}}, -1, 0\right). \tag{10.8}$$

It can be implemented by taking:

$$\delta t_i = -\frac{\sqrt{3} e v_F L_M}{4\pi} \sin(\mathbf{b}_i \cdot \mathbf{r}). \tag{10.9}$$

Thus, the resulting gauge choice explicitly preserves the $C_3$ symmetry in the tight-binding basis. Due to the rescaling of the system, we will measure the magnetic field in terms of the dimensionless parameter $L_M/l_B$, where $l_B = \sqrt{\hbar/eB_{\text{eff}}}$. Taking $B = 120T$, $L_M/l_B \sim 6-8$,[15] so we take the intermediate value of $L_M/l_B = 7$ for our simulations. In fact, Fig. 20 shows that a correlated state takes place at values slightly below $L_M/l_B = 6$, even with $U = t$. Therefore, using realistic values of $U \approx 2t$[194] a spontaneous symmetry breaking is expected within the experimental range.

The emergence of a pseudo-axial gauge field can also be explicitly derived from the real-space tight-binding model in Eq. 10.1 with hopping constants given by Eq. 10.2 without resorting to the low-energy description. For this purpose, we consider the real-space valley Berry flux $\chi(\mathbf{r})$ and define the valley Chern number of the system as its integral over the unit cell:

$$C_V = C_K - C_{K'} = \int_{u.c.} \chi(\mathbf{r}) d^2\mathbf{r}. \tag{10.10}$$

The real-space valley Berry flux in the tight-binding model is equivalent to the analytically derived valley-dependent magnetic field, and therefore will reflect the real-space structure of the emergent magnetic field explicitly in the full tight binding model across the unit cell. The real-space valley Berry flux can be computed within the Green's function formalism as:[195,183]

$$\chi(\mathbf{r}) = \langle \mathbf{r}| \int_{-\infty}^{0} d\omega \int_{\text{BZ}} \frac{d^2\mathbf{k}}{(2\pi)^2} \frac{\epsilon_{\alpha\beta}}{2} G_V (\partial_{k_\alpha} G_V^{-1})(\partial_{k_\beta} G_V) |\mathbf{r}\rangle. \tag{10.11}$$

Here, $\epsilon_{\alpha\beta}$ denotes the Levi-Civita tensor,

$$G_V = [\omega - H(\mathbf{k}) + i0^+]^{-1} \mathcal{P}_V \tag{10.12}$$

the Green's function associated to the Bloch Hamiltonian $H(\mathbf{k})$, and $\mathcal{P}_V$ the valley operator.[170,169,196] As shown in Fig. 18 (d), it is clearly observed that certain regions of the system show a positive valley flux, whereas others have negative flux. The negative valley flux is associated with the regions with compressive anisotropic strain, whereas the positive valley flux is associated with tensile anisotropic strain. This is the very same phenomenology expected from the artificial magnetic field obtained with a low energy Dirac expansion, reinforcing the connection between the low energy model and the exact solution of the tight-binding model.

We now study the electronic dispersion in the absence (Fig 19 (a)) and presence (Fig 19 (b)) of electronic interactions. In the non-interacting case, the system remains

gapless even in the presence of modulated strain, but with a highly reduced Fermi velocity due to a bandwidth quench to $W \sim 0.2t$ (Fig 19 (a)). Moreover, we observe that the strain modulation does not create intervalley scattering by projecting the resulting band diagram onto the valley states by means of the valley polarization operator $\mathcal{P}_V$,[170,169,196] see Fig 19 (a). Hence, valley is still a good quantum number. Interestingly, when interactions are turned on (Fig 19 (b)), a correlation gap $\Delta_{\text{corr}} \sim 0.01t$, consistent with the recent experiment,[15] opens up in the electronic structure stemming from an emergent magnetic state that slightly breaks sublattice symmetry of the electronic spectrum, which was also experimentally observed.[15] We highlight that such magnetism is not expect for pristine graphene with $U = t$, and, therefore, the bandwidth quench caused by strain is essential for a correlated state, since $W \ll U$. In the following, we address in details the origin of this symmetry breaking.

Figure 19 – (a) Band diagram for a non-interacting system consisting of a periodically strained graphene sheet projected onto the valley degrees of freedom, showing the absence of inter-valley mixing. (b) Selfconsistent band diagram for the corresponding interacting system projected onto sublattice degrees of freedom, showing an spontaneous sublattice asymmetry. The color scale in (a) indicates $+1$ for valley $K$ and $-1$ for $K'$, while in (b) $+1$ corresponds to sublattice $A$ and $-1$ to sublattice $B$.

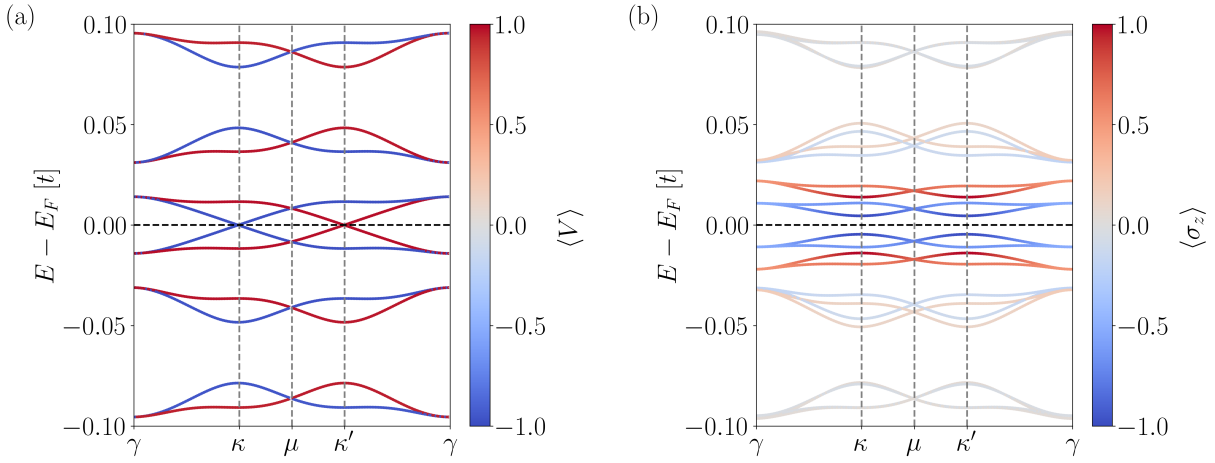


Source: author.

## 10.3 Magnetic ordering

### 10.3.1 Formation of periodically-modulated magnetization

To better understand the emergence of the correlated state, it is convenient to look at the spatial distribution of the low energy states in the absence of interactions (Fig. 20 (a)). The spatial distribution of these states corresponds to the zones of the superlattice under the influence of a strong elastic gauge field. Hence, according to the previous low energy discussion, these regions would be associated to zero pseudo Landau levels. A

Figure 20 – (a) Local density of states for the non-interacting case and (b) magnetization along the $z$-direction revealing antiferromagnetic ordering for the interacting case. A closer analysis reveals a ferrimagnetic periodic ordering, with the ferromagnetic component changing in sign with $B(\mathbf{r})$. (c) The dependence of both the modulated ferromagnetic ($\Xi$) and antiferromagnetic ($\mathcal{N}$) order parameters on the PMF for a $10 \times 10$ supercell.

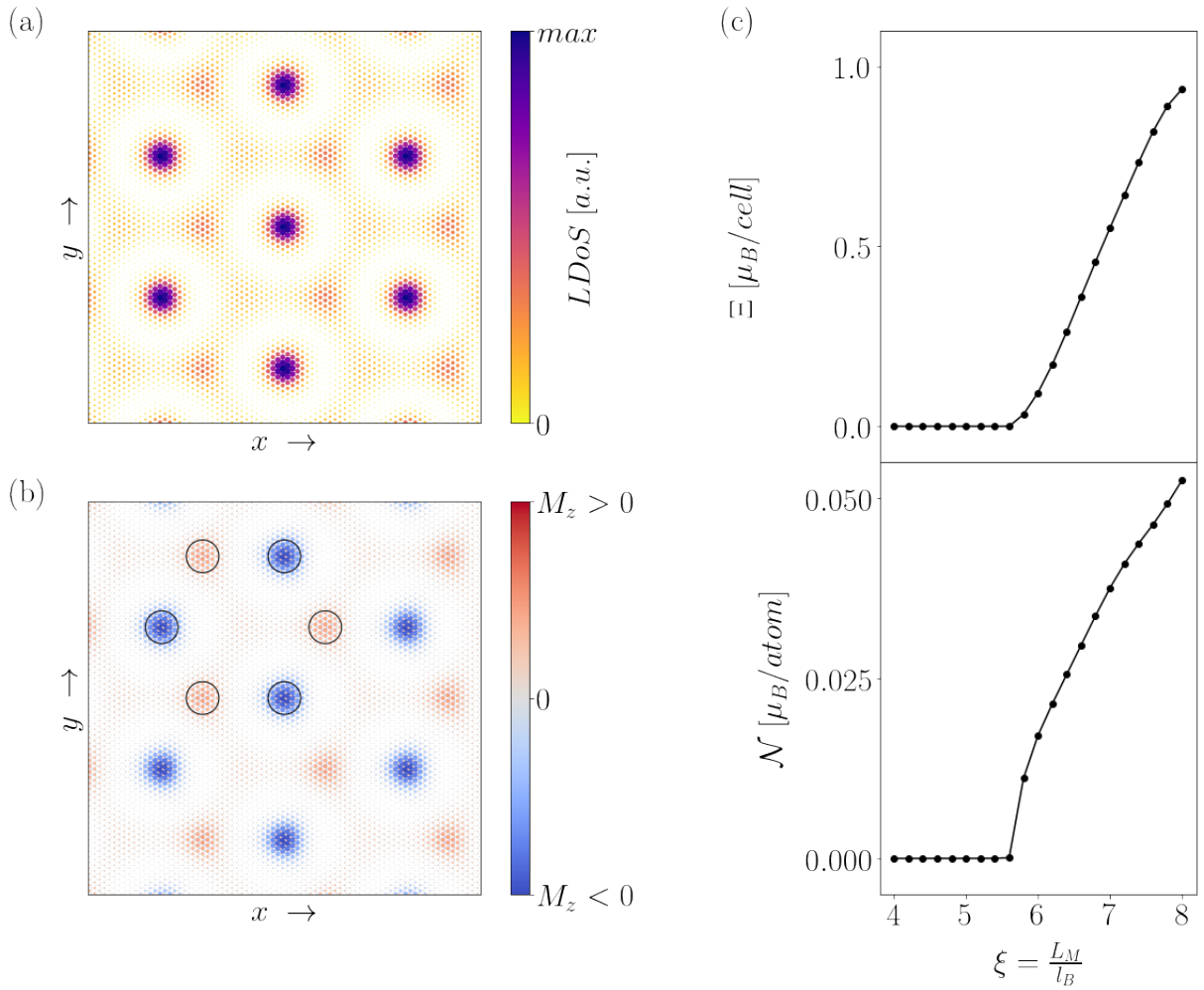


Source: author.

closer look also reveals that each extrema of the local density of states (LDOS) is strongly sublattice polarized, with the occupied sublattice depending on the PMF direction, as expected[197] and experimentally observed.[15] The localized states resulting from the buckling pattern indeed present non-zero magnetic order parameters when Hubbard interactions are considered. As expected, the magnetization (Fig. 20 (b)) correlates with the density of states of the non-interacting system (Fig. 20 (a)).

Figure 20 (b) shows the development of a periodically-modulated ferrimagnetic order parameter, which can also be interpreted as an antiferromagnetic signal with a noticeable sublattice imbalance due to the superposition of a smaller ferromagnetic signal, see Fig. 20 (c), in agreement with previous studies of a similar system.[67] The ferrimagnetism, in a first look, is counterintuitive following Lieb's theorem for a bipartide lattice,[198] and requires,

thus, a sublattice symmetry breaking. That is provided by the PMF,[197] as discussed in the previous paragraph. Furthermore, even though the groundstate is ferrimagnetic, the net magnetization of the system is zero. That is again a consequence of the pseudomagnetic field, since the sublattice polarization depends on the PMF sign. In other words, it is a consequence of the sublattice symmetry being broken *only* locally, but globally preserved with such PMF landscape.

In order to properly quantify the magnetization using global values within the supercell, one must carefully choose the order parameters. Since we are dealing with a system with ferrimagnetic ordering (in other words, a superposition of spatially-modulated antiferromagnetic and ferromagnetic order parameters), a good representative quantity is the standard Nèel order parameter:

$$\mathcal{N} = \left| \sum_i \left( \mathbf{m}_i \cdot \hat{z} \right) \sigma_i \right|, \tag{10.13}$$

where $\mathbf{m}_i$ is the magnetic moment at position $i$ and $\sigma_i$ is the corresponding sublattice index $\pm 1$. It is interesting to note that the magnetization profile shown in Fig. 20 (b) corresponds to an emerging honeycomb superlattice (actually, such emerging superlattice is already visible in the non-interacting LDOS profile in Fig. 20 (a)). Namely, we can distinguish two different ferrimagnetic regions with net magnetization $M_z > 0$ and $M_z < 0$ with majority of electrons located at $A$ and $B$ sublattices, respectively. Each of these regions can be understood as different Wannier orbitals of the emerging superlattice. Therefore, defining the usual ferromagnetic order parameter $\sum_i \mathbf{m}_i \cdot \hat{z}$ is pointless, since the contribution of neighboring Wannier orbitals will cancel themselves out, leading to zero net contribution. A better idea is then to modulate the usual ferromagnetic order parameter with a function that changes in sign for different superlattice Wannier orbitals. In fact, this can be done by considering the sign of the PMF. Namely,

$$\Xi = \left| \sum_i \mathrm{sgn}\left[ B(\mathbf{r}_i) \right] \left( \mathbf{m}_i \cdot \hat{z} \right) \right|. \tag{10.14}$$

The resulting order parameter $\Xi$ is intuitively understood as the superstructure's Nèel order parameter. Thus, all the phenomenology can be reduced to the analysis of such emerging honeycomb structure. We emphasize that Eq. 10.14 does not imply a dynamical coupling between the electronic spins and the PMF, but it reflects an indirect correlation between the magnetization and the PMF caused by sublattice plarization at the zeroth pseudo Landau level.[197]

We show in Fig. 20 (c) the dependence of both magnetizations on the PMF, indicating a clear phase transition. As a matter of fact, previous results showed that the scale-independent parameter is actually the product between the PMF and the number of sites inside the supercell,[67] a conclusion we verified for the system under consideration.

Figure 21 – (a, b) In plane magnetization for both sublattices of the emerging honeycomb superlattice, showing that the groundstate presents non-collinear magnetism. In (a), we zoom in the regions corresponding to $M_z < 0$ from Fig. 20 (b), while in (b), in the regions correponding to $M_z > 0$. The out-of-plane component, however, is about an order of magnitude larger and is qualitatively the same as in the case without SOC. (c) Dependency of magnetization with the filling factor for a $10 \times 10$ supercell showing that the magnetization is sensitive to doping.

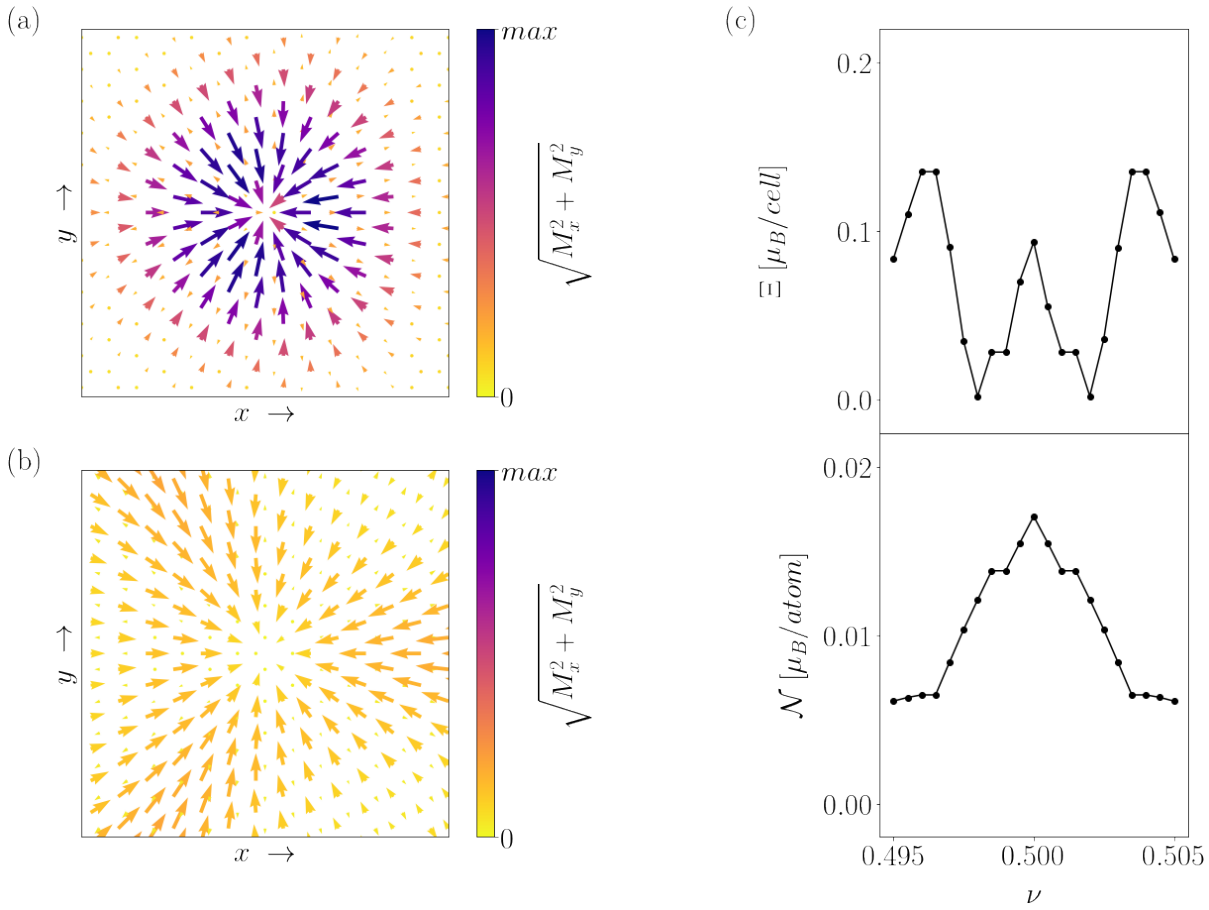


Source: author.

The transition occurs slightly below $L_M/l_B = 6$, meaning that a magnetic groundstate is expected for PMFs within the experimental range,[15] even using a conservative value of $U = t$, implying that for a realistic Hubbard coupling constant ($U \approx 2t$)[194] a spontaneous symmetry breaking is expected even for lower strain values.

### 10.3.2 Effects of doping and spin-orbit coupling

We now consider two relevant effects: (i) charge doping due to gate-tuning and (ii) effects of spin-orbit coupling (SOC) due to the breaking of inversion symmetry in the presence of a substrate.

Considering charge doping, one can check in Fig. 21 (c) a rapid decay in the

magnetic ordering as one goes away from half-filling. This result is consistent with the experimental observation of a gap opening as the Fermi energy approaches half-filling

We include spin-orbit coupling stemming from broken mirror symmetry with the substrate by adding a Rashba-like term to the graphene Hamiltonian:

$$H_{SOC} = i\lambda_R \sum_{i,j} (\mathbf{d}_{ij} \times \sigma_{s,s'} c^\dagger_{is} c_{js'}) \cdot \hat{z}, \tag{10.15}$$

with $\lambda_R = 0.015t$ to match *ab initio* estimations for graphene/$NbSe_2$ heterostructures.[199] Spin-momentum coupling explicitly breaks the spin rotation symmetry, allowing in-plane contributions to the magnetization to appear, as shown in Fig. 21 (a, b). On the other hand, the out-of plane contribution is an order of magnitude larger and qualitatively equal to calculations without SOC.

### 10.3.3 Breakdown of magnetic ordering with electric fields

The buckling pattern induces a non-homogeneous height variation of the graphene sheet with respect to the underlying substrate. Hence, the application of a perpendicular electric field should induce non-homogeneous energy shifts in real space. To account for this phenomenology, we consider the contribution from the following Hamiltonian:

$$\mathcal{H}_{\text{elec}} = \sum_{i=1}^{3} \mu(\mathbf{r}_i) c^\dagger_{is} c_{is} \ , \quad \mu(\mathbf{r}) = \mu_0 \sum_{i=1}^{3} \cos(\mathbf{b}_i \cdot \mathbf{r}), \tag{10.16}$$

where $\mu_0 = E\ \delta h/4.5$ is proportional to the electric field $E$ and the buckling amplitude $\delta h = 0.4nm$ (the factor 4.5 comes from the amplitude of the summation in Eq. 10.16). It is important to emphasize a peculiar feature of the heterostructure we consider in this chapter which is not expected for similar systems, *e.g.* corrugated graphene.[177] Namely, the functional forms of $\mu(\mathbf{r})$ (Eq. (10.16)) and the PMF $B(\mathbf{r})$ (Eq. (10.5)) match. This is a direct consequence of the PMF following the topography modulation in the system.[15] Such unique property results from a strong in-plane deformation which is hard to extract from STM measurements.[a] Indeed, this feature is essential for the electric tunnability of the system, since the nonzero values of $\mu(\mathbf{r})$ coincide with the locations with higher local density of states.

The resulting band diagram for the noninteracting system in Fig. 22 (a) shows that, in the presence of such perpendicular electric field, a gap opens and global sublattice symmetry breaks. It is straightforward to understand this effect, if we consider the emerging honeycomb superlattice: the electric field has the same effect as a sublattice mass in the superlattice.

[a] Privite communication with Slaviša Milovanović.

Figure 22 – (a) Band structure in the presence of a perpendicular bias, showing the emergence of a gap stemming from sublattice inequivalence ($\mu_0 = 0.005t$). This bias induced gap is expected to compete with the interaction induced gap. (b) Dependence of the magnetization on the external perpendicular electric field for a $10 \times 10$ supercell.

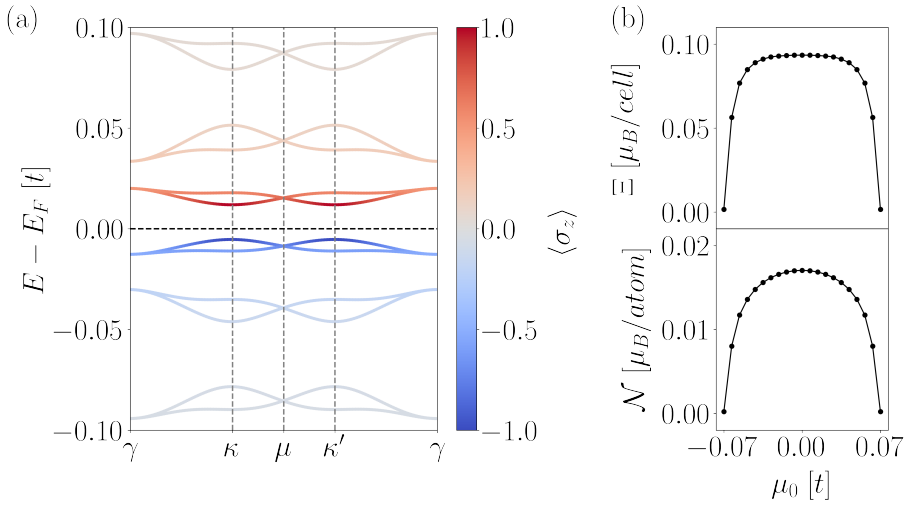


Source: author.

When electronic interactions are considered, one must expect a competition between two effects. In the presence of a finite sublattice mass, states with positive energy will be located in the sublattice $A$, while negative states, in the sublattice $B$, as one can see in Fig. 22 (a). On the other hand, in the presence of magnetic ordering, both sublattices are populated below and above the Fermi level, see Fig. 19 (b). As the sublattice mass increases, just one sublattice becomes populated below the Fermi energy, with both spin-up and spin-down states. In other words, one should expect that the magnetic ordering should be suppressed when the sublattice mass is larger than the antiferromagnetic gap, which should happen for $E \sim 0.1V/nm$. Indeed, that is exactly what we observe in Fig. 22 (b).

## 10.4 Summary

We showed that the zeroth pseudo Landau level subband formed in buckled graphene superlattices hosts a periodic magnetically ordered groundstate at half-filling, in agreement with recent experimental results. This periodic pattern results in an emerging antiferromagnetic honeycomb superlattice. Moreover, we showed that in the non-interacting scenario, a perpendicular electric field opens up a gap and can be interpreted as a sublattice effective mass in the superlattice scale. Interestingly, in the interacting case, the competition between the bias induced mass and the antiferromagnetic gap provides a route for electrically controlling the magnetic groundstate of the system. Our results show that strained graphene provides a powerful two dimensional platform to explore correlated physics in hybrid van der Waals structures, and to study the interplay between

artificial gauge fields and interactions. Finally, it is worth noticing that the interplay of such magnetic state with the $NbSe_2$ superconductivity, not addressed in the current chapter, can lead to a versatile platform to explore superlattice Yu-Shiba-Rusinov physics, and ultimately Majorana states.

# 11 Correlation-induced valley topology in buckled graphene superlattices

*Eu quero dizer*
*Agora o oposto do que eu disse antes*
*Eu prefiro ser*
*Essa metamorfose ambulante*

Raul Seixas, Metamorfose Ambulante

Flat bands emerging in buckled monolayer graphene superlattices have been recently shown to realize correlated states analogous to those observed in twisted graphene multilayers. Here, we demonstrate the emergence of valley topology driven by competing electronic correlations in buckled graphene superlattices. We show, both by means of atomistic models and a low-energy description, that the existence of long-range electronic correlations leads to a competition between antiferromagnetic and charge density wave instabilities, that can be controlled by means of screening engineering. Interestingly, we find that the emergent charge density wave has a topologically non-trivial electronic structure, leading to a coexistent quantum valley Hall insulating state. In a similar fashion, the antiferromagnetic phase realizes a spin-polarized quantum valley-Hall insulating state. Our results put forward buckled graphene superlattices as a new platform to realize interaction-induced topological matter.

The data shown in the figures, as well as the code generating all of the data in this chapter is available on Zenodo.[200]

## 11.1 Introduction

Mesoscopic systems provide a powerful platform to design quantum matter,[14,201–204] with the paradigmatic example of topological superconductivity artificially engineered in hybrid systems.[24,130,33,43,28,40,205–208] Moire two-dimensional materials have risen as a tunable platform to engineer states of matter,[204] ultimately allowing to explore a variety of

The content of this is chapter has been previously submitted as a preprint as Antonio L. R. Manesco, J. L. Lado, *Correlation-induced valley topology in buckled graphene superlattices*, arXiv:2104.00573.

controlable correlated states.[209–212] This emergence of tunable correlations stems from the quench of kinetic energy in emergent flat bands, controllable by twist engineering.[213–215] A variety of twisted van der Waals materials have been demonstrated in this direction, including bilayers, trilayers and tetralayers.[12,189,216–219]

Beyond the wide family of twisted moire multilayer heterostructures,[204] monolayer graphene has also been experimentally shown to realize moire-induced correlation physics in the single layer limit.[15] The field of straintronics, *i.e.*, the control of electronic properties of materials with strain,[220] has shown different methods to create two-dimensional periodically-strained superlattices, from substrate engineering[221] to inducing buckling transitions during fabrication.[15] From a low-energy perspective, strain fields act as valley-dependent pseudo-magnetic fields, leading to the emergence of pseudo-Landau levels.[66,179,222,223] From a critical value of in-plane strain, the elastic energy is spontaneously reduced with out-of-plane distortions,[224–226] as depicted in Fig. 23(a). The electronic structure reconstruction due to the strain field leads to the formation of nearly flat bands.[15,192] Moreover, the bandwidth suppression enhances the interaction effects and leads to electrically-controllable correlated phases.[15,16]

Here we show that buckled graphene superlattices yield correlation-induced topological states, stemming from the combination of pseudo-Landau levels and non-local electronic interactions.[15,16] In particular, we demonstrate that the low-energy states generated by the buckling [Fig. 23(b)] show an emergent honeycomb structure. Also, similarly to free-standing graphene, the bandstructure [Fig. 23(d)] has Dirac cones at the corners of the mini-Brillouin zone.[16] We derive the low-energy model describing the bands closer to the Fermi energy (Sec. 11.2), and explore the impact of electron-electron interactions, showing the existence of charge density wave and antiferromagnetic ground states (Sec. 11.3). Interestingly, these phases driven by electronic interactions show finite valley Chern numbers, and associated topological surface states. We finally demonstrate the robustness of our model by comparing it with full atomistic selfconsistent calculations, showing analogous phenomenology as the one predicted by the effective model. Our results demonstrate that buckled graphene monolayer can sustain a rich family of correlated topological states, realizing analogous physics to twisted graphene multilayers in the single monolayer limit.

## 11.2 The system

First, we review the electronic structure obtained with atomistic calculations discussed in Chapter 10. Under the periodic pseudo-magnetic field in Eq. 10.5, the electronic structure is folded into the mini-Brillouin zone defined by the $\mathbf{b}_n$ vectors from Eq. 10.6 [see Fig. 23(c)], and the hoppings are modulated as Eq. 10.9. As the strain takes a finite value, the crossings due to band foldings are split, creating mini-bands [see 23(d)]

Figure 23 – (a) Scheme of the buckled graphene superlattice studied. The $B$-field is the same as in Eq. 10.5 (b) Local density of states from full-lattice calculations. It is possible to note the emerging honeycomb structure. Valley-projected band structures from a full-lattice simulation of a buckled graphene superlattice (c) in the absence of strain and (d) in the buckled state. The dashed grey regions indicate the active bands for which we derive the effective model.

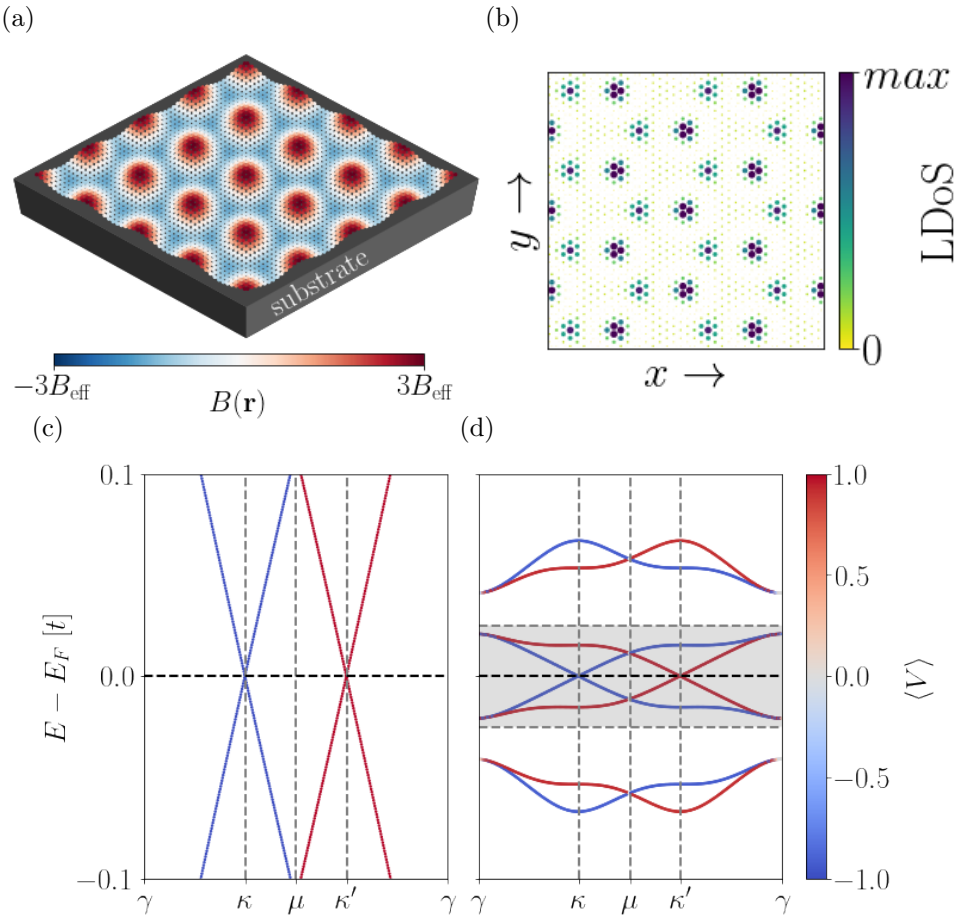


Source: author.

which we interpret as pseudo-Landau bands.[15,16] Hence, quasiparticles feel a bandwidth quench.

We perform the valley projection in full-lattice calculations (Figs. 23d and 28) computing the expectation value of the anti-Haldane coupling, $\langle V \rangle = \langle \Psi | V | \Psi \rangle$, with[169,170,227]

$$V = \frac{i}{3\sqrt{3}} \sum_{\langle\langle i,j \rangle\rangle} \eta_{ij} (\sigma_z)_{ij} \psi_i^\dagger \psi_j, \tag{11.1}$$

where $\eta_{ij} = \pm 1$ for clockwise/anticlockwise hopping, $\langle\langle i, j \rangle\rangle$ denotes a sum over second-neighbors, and $\sigma_z$ acts om sublattice degrees of freedom.

From the local density of states plot in Fig. 23(b), obtained with full-lattice tight-binding calculations described in Chapter 10,[16] it is possible to infer that the system has an emerging honeycomb superlattice. The Wannier sites are localized at the minima and

Figure 24 – (a) Schematic representation of the effective model in Eq. 11.2. (b) Valley-projected bandstructure of the effective model described by the Hamiltonian 11.2 with $m = M = \tilde{t}$.

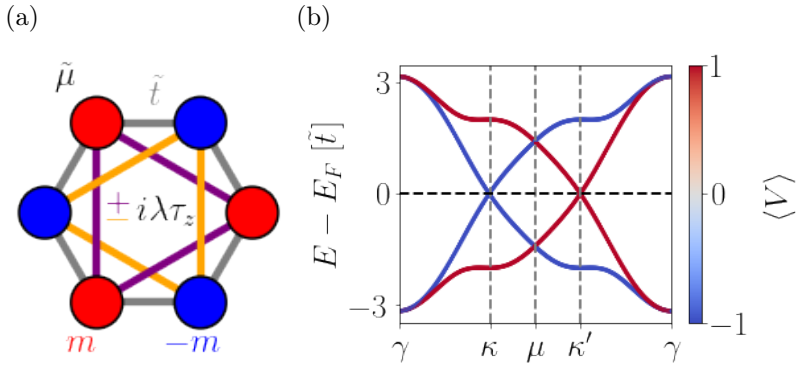


Source: author.

maxima of $B(\mathbf{r})$ [Eq. 10.5] since the characteristic length $\sqrt{\hbar/eB(\mathbf{r})}$ is smaller near the extrema. The two extrema (minimum and maximum) correspond to the two sublattices of this effective honeycomb structure. To reduce the computational cost of our numerical calculations, we now focus on the low-energy model describing these Wannier states, *i.e.*, on the active bands closer to the Fermi energy, highlighted in Fig. 23(d). This approach is analogous to low-energy models of twisted-bilayer graphene.

From both the space-dependent hopping constants (Eq. 10.9) and density of states [Fig. 23(b)], we conclude that the system is invariant under $C_3$-rotations. Moreover, the bandstructure in Fig. 23(d) suggest that valley number is a conserved quantity. Finally, in the absence of electronic interactions, the system has time-reversal symmetry. With the current constraints, we find that the family of honeycomb Hamiltonians restricted to these symmetries is[228]

$$\begin{aligned}\mathcal{H} = &-\tilde{\mu}\sum_{i}\sum_{s,\tau} c^{\dagger}_{is\tau}c_{is\tau} + m\sum_{i}\sum_{s,\tau}(\sigma_z)_{ii}c^{\dagger}_{is\tau}c_{is\tau} \\ &-\tilde{t}\sum_{s,\tau}\sum_{\langle i,j\rangle} c^{\dagger}_{is\tau}c_{js\tau} + i\lambda\sum_{s,\tau}\sum_{\langle\langle i,j\rangle\rangle}(\tau_z)_{\tau\tau}\eta_{ij}c^{\dagger}_{is\tau}c_{js\tau}\end{aligned} \tag{11.2}$$

where $c^{\dagger}_{is\tau}$ are creation and $c_{is\tau}$ annihilation operators operators at the site $i$, sublattice $\sigma$, valley $\tau$, and spin $s$. The Pauli matrices $\sigma_i$ and $\tau_i$ act on sublattice and valley degrees of freedom. The onsite energy and the hopping constants are denoted by $\tilde{\mu}$ and $\tilde{t}$ to distinguish from the atomistic model. There is also a sublattice imbalance $m$ and a valley-dependent second-neighbors hopping $\lambda$. An scheme of this model is shown in Fig. 24(a). Note that, since the Brillouin zone of this system corresponds to the mini-Brillouin zone from the atomistic model, there is an extra *mini-valley* degree of freedom corresponding to the two nonequivalent points $\kappa$ and $\kappa'$ in effective model Brillouin zone.

It is visible that the Hamiltonian of Eq. 11.2 is equivalent to the Kane-Mele (KM) model: it consists on the tight-binding model of a honeycomb structure with a sublattice imbalance and a second-neighbors hopping that depends on the valley isospin. The mapping between both models is made by identifying the valley isospin in the buckled superlattice to spin in KM model ($\text{spin}_{KM} \rightarrow \text{valley}_{\text{buckled}}$), as well as identifying the mini-valleys $\kappa$ and $\kappa'$ in the buckled system to the valleys $K$ and $K'$ in KM model ($\text{valley}_{KM} \rightarrow \text{mini-valley}_{\text{buckled}}$).[82,83] As shown in Fig. 24(b), the energy dispersion is similar to the bandstructure of the full system [Fig. 23(d)] when $m = 3\sqrt{3}\lambda =: M$. Therefore, the non-interacting strained system (without symmetry breakings) is enforced to have $M = m = \tilde{t}$ due to its gapless nature. Note that arbitrarily small variations of $m/M$ open a gap in the effective model. If $\delta(m/M) > 0$, the system becomes a trivial insulator. On the other hand, $\delta(m/M) < 0$ opens a topological gap and the system becomes a quantum valley Hall insulator, in analogy to the spin Hall insulator phase in the KM model.

Since the topographic shape of the buckling has the same functional form of $B(\mathbf{r})$, out-of-plane displacement fields lead to a modulation of onsite energies as shown in Eq. 10.16.[16] Thus, near the maxima of $B(\mathbf{r})$, $\mu(\mathbf{r}) \approx 3\mu_0$, while $\mu(\mathbf{r}) \approx 3\mu_0/2$ near the minima of $B(\mathbf{r})$. From the effective model perspective, the onsite energy modulation due to an additional displacement field is:

$$\mathcal{H}_{\text{elec}} = 3\mu_{\text{elec}} \sum_{i\in A} \sum_{s.\tau} c^{\dagger}_{is\tau} c_{is\tau} - \frac{3\mu_{\text{elec}}}{2} \sum_{i\in B} \sum_{s,\tau} c^{\dagger}_{is\tau} c_{is\tau}, \tag{11.3}$$

where $\mu_{\text{elec}} \propto \mu_0$. The sum over $i$ is performed on different sublattices in Eq. 11.3, since the corresponding Wannier sites are located at the maxima and minima of $\mu(\mathbf{r})$. This extra term modifies the Hamiltonian as $m \rightarrow m + 3\mu_{\text{elec}}/2$, and $\tilde{\mu} \rightarrow \tilde{\mu} - 3\mu_{\text{elec}}/2$. Therefore, out-of-plane displacement fields might be used as a knob to control the ratio $m/M$, ultimately working as an electric control of the system's topology, as shown in Fig. 25 (a).

## 11.3 Interaction-driven quantum valley Hall effect

The reduced bandwidth reduction due to the pseudo-magnetic field has been shown to lead to a correlated phase.[15,16] Yet, due to the degeneracy of the low energy states, different groundstates may be realized in the system, depending on the range and strength of interactions.[50,48,49] The computational cost of full-lattice calculations makes an extensive investigation of possible groundstates impractical. Hence, the reduced computational cost with an effective model allows us to explore the phase diagram as a function of electronic interactions.

To investigate the phase diagram of buckled graphene, we now include electronic

Figure 25 – Valley Chern number dependence on (a) sublattice imbalance $m$ and antiferromagnetic mass $m_{\mathrm{AF}}$ for the effective model, taking constant $\lambda$. Panel (b) shows the valley Chern number obtained after including interactions in the model, as a function of the Hubbard constant $\tilde{U}$ and nearest-neighbors interactions $\tilde{V}$. Solid lines indicate a topological phase transition and dashed lines indicate $m = M$, which for $m_{\mathrm{AF}}$ corresponds to the non-interacting strained system.

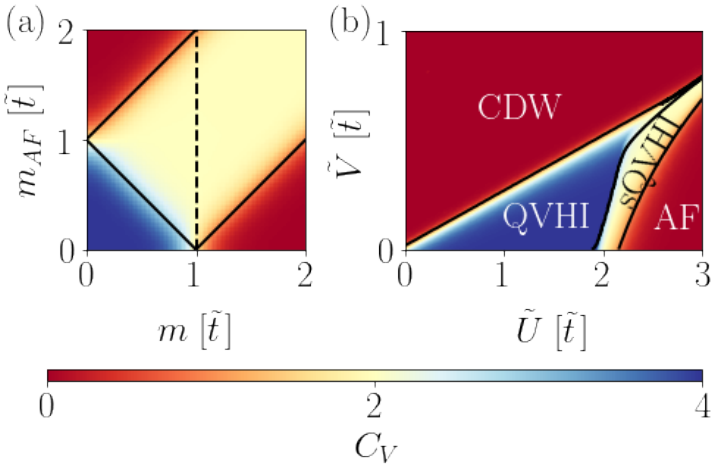


Source: author.

interactions in the low energy model

$$\mathcal{H}_{\mathrm{int}} = \tilde{U} \sum_{\substack{\alpha,\beta \\ \alpha\neq\beta}} \sum_{i} n_{i\alpha} n_{i\beta} + \tilde{V} \sum_{\langle i,j \rangle} \sum_{\alpha,\beta} n_{i\alpha} n_{j\beta} \tag{11.4}$$

where $\tilde{U}$ is the onsite Hubbard interaction, $\tilde{V}$ is the nearest-neighbor interaction, and $n_{i\alpha} := c^{\dagger}_{i\alpha} c_{i\alpha}$ is the number operator at the Wannier site $i$. The subindices $\alpha$ and $\beta$ are a short-hand notation to include both valley and spin degrees of freedom.

We solve this Hamiltonian by means of a mean-field approximation. Namely, we make

$$\mathcal{H}_{\mathrm{int}} \approx \mathcal{H}_{\mathrm{MF}} = \sum_{i,j,\alpha,\beta} \chi_{ij\alpha\beta} c^{\dagger}_{i\alpha} c_{j\beta}, \tag{11.5}$$

and find $\chi_{ij\alpha\beta}$ self-consistently. First, it is important to note that the interaction strengths $\tilde{U}$ and $\tilde{V}$ depend on the screening created by the substrate of the buckled structure,[229] and as such can be controlled by screening engineering.[229–232] In the following, we will explore the potential symmetry broken states as a function of the two interaction strengths, keeping in mind that such values would be controlled by substrate engineering. As we change the ratio of the local and non-local interactions, we see that there are two different groundstates, shown in the phase diagram of Fig. 26(c). The order parameters are extracted by computing checking the matrix form of $\chi_{ij\alpha\beta}$: a change in the sublattice imbalance $m$ is interpreted as a charge density wave; while an additional term with the same matrix form

Figure 26 – Illustration of (a) antiferromagnetic and (b) charge density wave groundstates. (c) Phase diagram as a function of the coupling constants $\tilde{U}$ and $\tilde{V}$. The groundstate is a charge density wave (CDW) unless $\tilde{U}$ is sufficiently high. For $\tilde{U}$ higher than a critical value, an antiferromagnetic (AF) order develops. (d) System gap as a function of the electron-electron couplings. It is visible that the gap closes outside the region in which the broken symmetry changes.

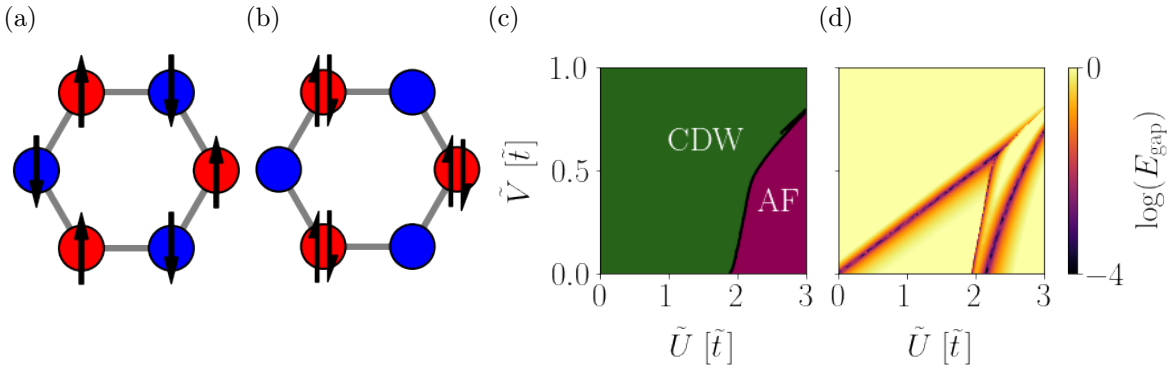


Source: author.

of Eq. 11.6 is interpreted as an antiferromagnetic order. A charge density wave, illustrated in Fig. 26(b), develops and persists until the Hubbard constant reaches a critical value at which an antiferromagnetic ordering, depicted in Fig. 26(a), occurs. For $\tilde{V} = 0$, this critical value is $\tilde{U}_c \sim 2t$, as expected for honeycomb systems.[194]

From a mean-field perspective, the charge density wave groundstate leads to a change in the sublattice imbalance. In other words, it leads to a transformation $m \to m + m_{\text{CDW}}$. The effects of an antiferromagnetic order lead to the additional term in the Hamiltonian 11.2:

$$H_{AF} = m_{\text{AF}} \kappa_0 \otimes \tau_0 \otimes \sigma_z \otimes s_z, \tag{11.6}$$

where $s_z$ acts on the spin space. Note that one can interpret the antiferromagnetic term as a spin-dependent sublattice imbalance.

As discussed in Sec. 11.2, small variations on the ratio $m/M$ lead to a gap opening. That makes one wonder if there are topological phase transitions as we change the electron-electron coupling constants. Hence, we compute, for different values of $m$ and $m_{\text{AF}}$, the valley Chern number[195,183]

$$C_V = C_K - C_{K'} = \int_{-\infty}^{0} d\omega \int_{\text{BZ}} \frac{d^2\mathbf{k}}{(2\pi)^2} \frac{\epsilon_{\alpha\beta}}{2} G_V (\partial_{k_\alpha} G_V^{-1})(\partial_{k_\beta} G_V). \tag{11.7}$$

Here, $\epsilon_{\alpha\beta}$ denotes the Levi-Civita tensor,

$$G_V = [\omega - H(\mathbf{k}) + i0^+]^{-1} \mathcal{P}_V \tag{11.8}$$

the Green's function associated with the Bloch Hamiltonian $H(\mathbf{k})$, and $\mathcal{P}_V = \tau_z$ is the valley operator.

Figure 27 – Sublattice-projected bandstructure for selected $\tilde{U}$ and $\tilde{V}$ showing all four distinct phases: (a) charge density wave, (b) antiferromagnet, (c) quantum valley Hall insulator, and (d) spin-polarized quantum valley Hall insulator.

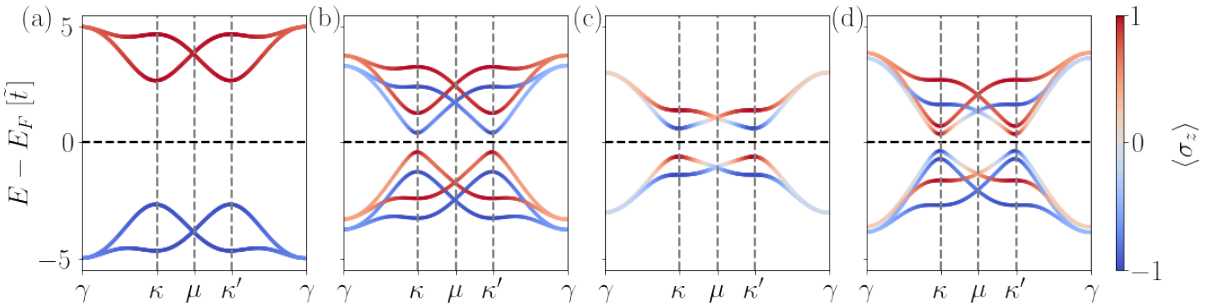


Source: author.

We see in Fig. 25 (a) that there are two topologically nontrivial phases: one of them is a QVHI for both spin channels (valley Chern number 4), the other is the one that we predict to exist in a single spin channel (valley Chern number 2). The formation of both phases is rather intuitive to understand. While the QVHI takes place when $\delta(m/M) < 0$, the sQVHI phase exist for any finite $m_{\mathrm{AF}}$. The reason is that while one spin channel suffers a shift $m \to m + m_{\mathrm{AF}}$, the other is shifted as $m \to m - m_{\mathrm{AF}}$. Thus, one spin channel becomes topological and the other becomes a trivial insulator. This is visible in Fig. 27: in the QVHI phase [Fig. 27 (c)], all four bands show a band inversion; and in the sQVHI phase [Fig. 27 (d)], only two out of the four bands show a band inversion. The band inversion occurs in the spin channels for which the sublattice imbalance decreases.

Now we note that, even though there are only two regions in the order parameter map of Fig. 26(c), there are several gap closings in Fig. 26(d). Reviewing the phase diagram by also checking the valley Chern number, it is visible that varying $\tilde{U}$ and $\tilde{V}$ yields four distinct phases: trivial charge density wave and antiferromagnet, as well as topological charge density wave (QVHI) and topological antiferromagnet (sQVHI). We also show selected valley-projected band diagrams in Figs. 27 (a-d). While the trivial charge density wave [Fig. 27(a)] and antiferromagnetic [Fig. 28(b)] bulk bands have well-defined sublattice numbers, the QVHI [Fig. 27(c)] and the sQVHI [Fig. 27(d)] show a band inversion.

To compare with the effective model calculations, we perform self-consistent Hubbard mean-field calculations in a superlattice following our the results of Chapter 10.[16] To reduce the computational cost, we rescaled the system as $a \to \beta a$ and $t \to t/\beta$ so the Fermi velocity keeps constant.[166] We choose, as an example, the Hubbard constant to be $U = 0.3t$, resulting in a correlation gap in the bandstructure [see Fig. 28(b)]. The gap is a result of a magnetic phase in the form of a superlattice-modulated ferrimagnetic order [see Fig. 28(a)]. Integrating the magnetization in the vincinity of a minimum of $B(\mathbf{r})$ the magnetization is finite and positive, while it is negative in the neighborhood of

Figure 28 – (a) Magnetization along the $z$-direction. A periodically modulated ferrimagnetic order is formed. From a superlattice perspective, it corresponds to a antiferromagnetic honeycomb structure. Results of full-lattice calculations with modulated hoppings in Eq. 10.9 solved self-consistently with an additional Hubbard constant $U = 0.3t$. Valley Chern number in a (b) infinite system and (c) in a nanoribbon. (d) $y$-position projection of a nanoribbon bandstructure. We see that each edge has two counter-propagating edge states with opposite valley-polarization.

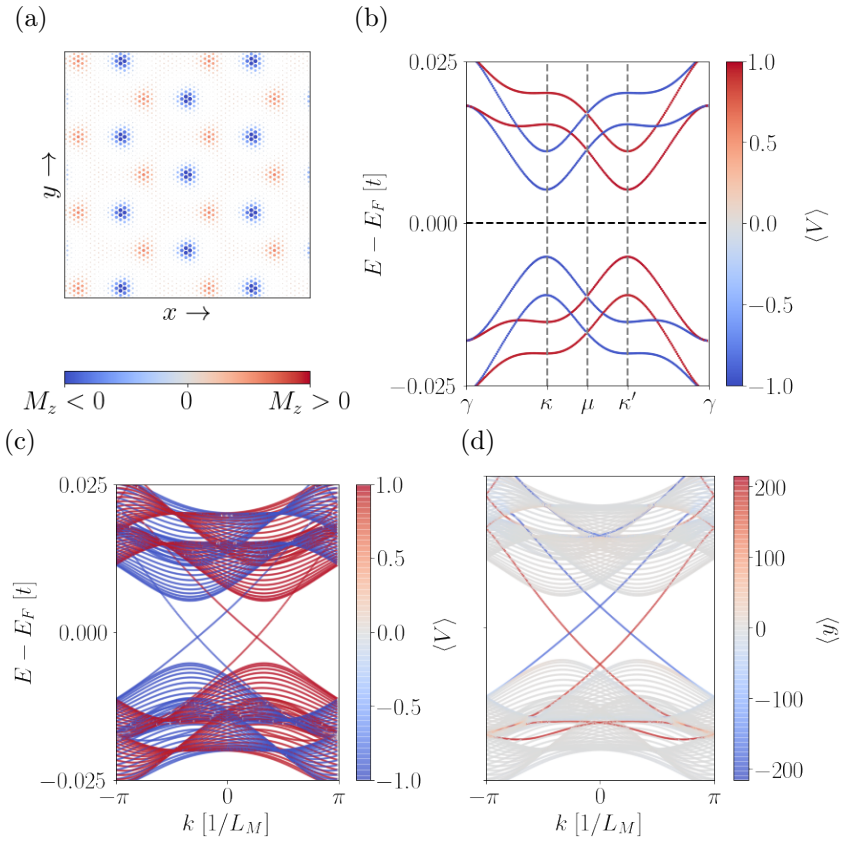


Source: author.

pseudo-magnetic field maxima. In this situation, the system has a valley Chern number 2, in accordance with our effective model calculations with an antiferromagnetic ordering. We found that this system is in the sQVHI phase, with valley Chern number 2, compatible with the magnetically ordered groundstate observed.[16] The existence of topological edge states is visible in the bandstructure of a nanoribbon, shown in Fig. 28(c) and 28(d). As expected, we observe two counter-propagating (helical-like) edge states with opposite valley numbers at both boundaries, similarly to the Kane-Mele model.[82,83] Finally, we note that the local charge accumulation with the periodic potential might also change the values of $\tilde{U}$ and $\tilde{V}$. Furthermore, the increase of out-of-plane fields closes the antiferromagnetic gap.[16] Thus, electrostatic control is not only a knob to control topology, but also electronic correlations.

## 11.4 Summary

To summarize, we have shown that buckled graphene superlattices show spontaneous symmetry breaking driven by electronic interactions, leading to a topological gap opening. First, by combining atomistic low energy models with a symmetry analysis, we derived an effective model for the lowest bands of buckled graphene superlattices. We then included electronic interactions in a non-local form in the low-energy model, showing the emergence of competing ground states. Namely, an antiferromagnetic and a charge density wave. Remarkably, the spontaneous breaking of symmetries was shown to lead to a topological gap opening for a wide range of the non-local interactions. The charge density wave phase hosts a quantum valley Hall insulator, while the antiferromagnetic phase has a spin-polarized quantum valley Hall insulator region in the parameter space. Our results put forward buckled graphene superlattices as a platform to study interaction-induced valley topology, and highlight that single layer moire systems can potentially host analogous correlated states to those of complex twisted graphene multilayers.

# Part III

# Concluding remarks

*And in the end*
*The love you take*
*Is equal to the love you make*

The Beatles, The End

Graphene's versatility led to several groundbreaking discoveries in the field of Condensed Matter Physics. Not only the fabrication of high-quality two-dimensional mesoscopic devices, but also the possibility to engineer correlated and topological phases. The plethora of different phenomena reported and predicted in the last couple of decades makes graphene a candidate to spintronics, valleytronics, twistronics, straintronics and quantum computation. Combining graphene with other materials opens an even wider range of possibilities. In this thesis, we covered experimental realizations of hybrid devices that use graphene as a building block. We both investigated the current status of state-of-art experiments as well as proposed new phenomena and ways to improve ongoing experiments.

In Part I, we investigated electronic, topologial and transport properties of quantum Hall graphene/superconductor junctions. First, a low-energy theory was derived using a combination of wave-matching with Wilson masses to describe topological superconductivity at half-filling. Our theory suggest the need to minimize intervalley scattering to open the topological gap. Moreover, Fermi level mismatch must also be avoided to ensure a finite gap. Thus, the topologically non-trivial phases is sensitive to parameters that are challenging to control in experiments.

A recent Andreev conductance measurements in quantum Hall graphene devices was then studied, as a way to better understand the current status of fabrication quality. We investigated different mechanisms that could lead to interference of chiral Andreev states recently reported in an experiment. We showed that lattice orientation produces intervalley scattering, leading to interference-induced conductance oscillations when the interface is along the armchair orientation. The interference, however, is rapidly supressed as one moves away from the armchair orientation. Such perfect alignment with the armchair orientation would be accidental in experiments. Hence, it is unlikely to be the reason of the reported interference. However, if intervalley mixing is enhanced by disorder, irregular oscillations in conductance as a function of magnetic field and gate voltage appear, in good qualitative agreement with experiments.

We further consider Fermi level mismatch between the quantum Hall region and the superconductor. Electrostatic simulations in previous works showed that the potential

landscape is smooth, such that intervalley scattering is not possible. The mismatch, on the other hand, locally changes the filling factor. Thus, close to the interface, non-chiral edge states are also populated. The incoming edge states couples with the multiple edge states, resulting on extra interference patterns.

Our analysis has several consequences to the interpretation of state-of-art experiments. First, the similarity of our simulations including disorder with the experimental data suggest that there is a need to improve the quality of graphene/superconductor interfaces. A possible alternative is to use van der Waals superconductors, such as $NbSe_2$. The interference caused by Fermi level mismatch also motivates further attention to the electrostatic profile close to the junction. Moreover, the existance of both effects is detrimental to engineer Majorana zero modes.

We then moved to the investigation of recently fabricated graphene/$NbSe_2$ hybrid systems. It has been shown that compressive strain introduced during fabrication results in a buckling transition to reduce elastic energy. The out-of-plane deformation has a periodic pattern, resulting in superlattices with period $\sim 14\,\mathrm{nm}$. The bandstructure resconstruction due to strain leads to the formation of nearly flat bands.

The kinetic energy quench caused by the superlattice strain field enhances the effect of electron-electron interactions. We showed that this buckled system undergoes a spontaneous symmetry breaking, in agreement with experiments. Namely, we showed the system has a modulated ferrimagnetic order parameter. Using the system's topography, we also showed that it is possible to electrically control the correlations. Finally, our calculations showed that spin-orbit coupling leads to non-collinear magnetic groundstates.

Observing the local density of states at Fermi energy, we see that the studied buckling pattern induces a honeycomb potential. Electrons are bounded to the lower and upper bounds of the pseudo-magnetic field caused by strain. Using symmetry arguments, we developed a low-energy theory for the system, reducing the computational cost to evaluate the effects of external fields and interactions. Our calculations showed that the system has two competing groundstates: charge density wave and antiferromagnetism, both of which have a topological region. While the CDW phase is a quantum valley Hall insulator, the AF phase is a spin-polarized quantum valley Hall insulator. Thus, this buckled graphene superlattice is an ideal platform to design valley topology.

To summarize, in this thesis we explored the interplay of electronic correlations and topology in hybrid graphene-based systems. We investigated two different systems explored in recent state-of-art experiments. We suggested possible improvements for upcoming experiments studying superconducting coherence in quantum Hall edge states, ultimately aiming to create Majorana zero modes. We also predicted competing correlated phases in buckled graphene superlattices, some of them showing non-trivial valley topology.

# References


1 LILIENFELD JULIUS EDGAR. Lilienfeld Julius Edgar. **Method and Apparatus for Controlling Electric Currents**. Jan. 1930. 1745175A. U.S. pat. Cit. on p. 29.

2 MOORE, Gordon E. Cramming more components onto integrated circuits, Reprinted from Electronics, volume 38, number 8, April 19, 1965, pp.114 ff. **IEEE Solid-State Circuits Society Newsletter**, v. 11, n. 3, p. 33–35, 2006. DOI: 10.1109/N-SSC.2006.4785860. Cit. on p. 29.

3 ROTMAN, David. We're Not Prepared for the End of Moore's Law. **MIT Technology Review**. Cit. on p. 29.

4 NOVOSELOV, K. S. *et al.* Electric Field Effect in Atomically Thin Carbon Films. **Science**, American Association for the Advancement of Science, v. 306, n. 5696, p. 666–669, Oct. 2004. ISSN 0036-8075, 1095-9203. DOI: 10.1126/science.1102896. pmid: 15499015. Cit. on pp. 29, 36.

5 GEIM, A. K.; NOVOSELOV, K. S. The Rise of Graphene. **Nature Materials**, Nature Publishing Group, v. 6, n. 3, p. 183–191, Mar. 2007. ISSN 1476-4660. DOI: 10.1038/nmat1849. Cit. on p. 29.

6 NOVOSELOV, K. S.; MISHCHENKO, A.; CARVALHO, A.; NETO, A. H. Castro. 2D Materials and van Der Waals Heterostructures. **Science**, American Association for the Advancement of Science, v. 353, n. 6298, July 2016. ISSN 0036-8075, 1095-9203. DOI: 10.1126/science.aac9439. pmid: 27471306. Cit. on p. 29.

7 SCHAIBLEY, John R. *et al.* Valleytronics in 2D Materials. **Nature Reviews Materials**, Nature Publishing Group, v. 1, n. 11, p. 1–15, Aug. 2016. ISSN 2058-8437. DOI: 10.1038/natrevmats.2016.55. Cit. on p. 29.

8 AHN, Ethan C. 2D Materials for Spintronic Devices. **npj 2D Materials and Applications**, v. 4, n. 1, p. 17, Dec. 2020. ISSN 2397-7132. DOI: 10.1038/s41699-020-0152-0. Cit. on p. 29.

9 QIAN, Xiaofeng; LIU, Junwei; FU, Liang; LI, Ju. Quantum Spin Hall Effect in Two-Dimensional Transition Metal Dichalcogenides. **Science**, American Association for the Advancement of Science, v. 346, n. 6215, p. 1344–1347, Dec. 2014. ISSN 0036-8075, 1095-9203. DOI: 10.1126/science.1256815. pmid: 25504715. Cit. on p. 29.

10 CAO, Y. *et al.* Superlattice-Induced Insulating States and Valley-Protected Orbits in Twisted Bilayer Graphene. **Physical Review Letters**, v. 117, n. 11, p. 116804, Sept. 2016. DOI: 10.1103/PhysRevLett.117.116804. Cit. on pp. 29, 89.

11 CAO, Yuan *et al.* Unconventional Superconductivity in Magic-Angle Graphene Superlattices. **Nature**, Nature Publishing Group, v. 556, n. 7699, p. 43–50, Apr. 2018. ISSN 1476-4687. DOI: 10.1038/nature26160. Cit. on pp. 29, 49.

12 CAO, Yuan *et al.* Correlated Insulator Behaviour at Half-Filling in Magic-Angle Graphene Superlattices. **Nature**, Nature Publishing Group, v. 556, n. 7699, p. 80–84, Apr. 2018. ISSN 1476-4687. DOI: 10.1038/nature26154. Cit. on pp. 29, 49, 89, 101.

13 BISTRITZER, R.; MACDONALD, A. H. Moire Bands in Twisted Double-Layer Graphene. **Proceedings of the National Academy of Sciences**, Proceedings of the National Academy of Sciences, v. 108, n. 30, p. 12233–12237, July 2011. ISSN 0027-8424, 1091-6490. DOI: 10.1073/pnas.1108174108. pmid: 21730173. Cit. on pp. 29, 89.

14 ZHANG, Yang; YUAN, Noah F. Q.; FU, Liang. Moiré Quantum Chemistry: Charge Transfer in Transition Metal Dichalcogenide Superlattices. **Physical Review B**, American Physical Society, v. 102, n. 20, p. 201115, 30 Nov. 2020. DOI: 10.1103/PhysRevB.102.201115. Cit. on pp. 29, 100.

15 MAO, Jinhai *et al.* Evidence of Flat Bands and Correlated States in Buckled Graphene Superlattices. **Nature**, Nature Publishing Group, v. 584, n. 7820, p. 215–220, 7820 Aug. 2020. ISSN 1476-4687. DOI: 10.1038/s41586-020-2567-3. Cit. on pp. 29–32, 49, 89–94, 96, 97, 101, 102, 104.

16 MANESCO, A. L. R. *et al.* Correlations in the Elastic Landau Level of Spontaneously Buckled Graphene. **2D Materials**, IOP Publishing, v. 8, n. 1, p. 015011, Oct. 2020. ISSN 2053-1583. DOI: 10.1088/2053-1583/abbc5f. Cit. on pp. 29, 31, 32, 37, 49, 101, 102, 104, 107, 108.

17 MEINDL, J. D. Limits on Silicon Nanoelectronics for Terascale Integration. **Science**, American Association for the Advancement of Science, v. 293, n. 5537, p. 2044–2049, Sept. 2001. ISSN 00368075, 10959203. DOI: 10.1126/science.293.5537.2044. pmid: 11557881. Cit. on pp. 29, 38.

18 LUNDSTROM, M. APPLIED PHYSICS: Enhanced: Moore's Law Forever? **Science**, American Association for the Advancement of Science, v. 299, n. 5604, p. 210–211, Jan. 2003. ISSN 00368075, 10959203. DOI: 10.1126/science.1079567. pmid: 12522237. Cit. on p. 29.

19 COLES PATRICK, Scott Pakin. The Problem with Quantum Computers. **Scientific American Blog Network**. Cit. on p. 30.

20 ARUTE, Frank *et al.* Quantum Supremacy Using a Programmable Superconducting Processor. **Nature**, Nature Publishing Group, v. 574, n. 7779, p. 505–510, Oct. 2019. ISSN 1476-4687. DOI: 10.1038/s41586-019-1666-5. Cit. on p. 30.

21 CHOJUL. 9, Adrian; 2020; PM, 2:00. The Biggest Flipping Challenge in Quantum Computing. **Science | AAAS**, July 2020. Cit. on p. 30.

22 STANESCU, Tudor D. **Introduction to Topological Quantum Matter & Quantum Computation**. 1ª edição: CRC Press, Dec. 2016. Cit. on pp. 30, 43, 44, 46.

23 BERNEVIG, B. Andrei; ZHANG, Shou-Cheng. Quantum Spin Hall Effect. **Physical Review Letters**, American Physical Society, v. 96, n. 10, p. 106802, Mar. 2006. DOI: 10.1103/PhysRevLett.96.106802. Cit. on pp. 30, 47.

24 KITAEV, A. Yu. Fault-Tolerant Quantum Computation by Anyons. **Annals of Physics**, Elsevier, v. 303, n. 1, p. 2–30, Jan. 2003. ISSN 0003-4916. DOI: 10.1016/S0003-4916(02)00018-0. Cit. on pp. 30, 62, 100.

25 KITAEV, A. Yu. Unpaired Majorana Fermions in Quantum Wires. **Physics-Uspekhi**, Uspekhi Fizicheskikh Nauk (UFN) Journal, v. 44, p. 131–136, 10S Oct. 2001. ISSN 1063-7869. DOI: 10.1070/1063-7869/44/10S/S29. Cit. on pp. 30, 44, 52, 62, 63.

26 TOPOLOGICAL Insulators and Topological Superconductors. Sun, 04/07/2013 - 12:00. ISBN 978-0-691-15175-5. Cit. on pp. 30, 33, 34, 43.

27 RYU, Shinsei; SCHNYDER, Andreas P.; FURUSAKI, Akira; LUDWIG, Andreas W. W. Topological Insulators and Superconductors: Tenfold Way and Dimensional Hierarchy. **New Journal of Physics**, IOP Publishing, v. 12, n. 6, p. 065010, June 2010. ISSN 1367-2630. DOI: 10.1088/1367-2630/12/6/065010. Cit. on pp. 30, 44, 46, 64, 65.

28 MOURIK, V. *et al.* Signatures of Majorana Fermions in Hybrid Superconductor-Semiconductor Nanowire Devices. **Science**, American Association for the Advancement of Science, v. 336, n. 6084, p. 1003–1007, May 2012. ISSN 0036-8075, 1095-9203. DOI: 10.1126/science.1222360. pmid: 22499805. Cit. on pp. 30, 63, 100.

29 DAS, Anindya *et al.* Zero-Bias Peaks and Splitting in an Al–InAs Nanowire Topological Superconductor as a Signature of Majorana Fermions. **Nature Physics**, Nature Publishing Group, v. 8, n. 12, p. 887–895, Dec. 2012. ISSN 1745-2481. DOI: 10.1038/nphys2479. Cit. on p. 30.

30 POPINCIUC, M. *et al.* Zero-Bias Conductance Peak and Josephson Effect in Graphene-NbTiN Junctions. **Physical Review B**, American Physical Society, v. 85, n. 20, p. 205404, May 2012. DOI: 10.1103/PhysRevB.85.205404. Cit. on pp. 30, 49, 75.

31 DENG, M. T. *et al.* Anomalous Zero-Bias Conductance Peak in a Nb–InSb Nanowire–Nb Hybrid Device. **Nano Letters**, American Chemical Society, v. 12, n. 12, p. 6414–6419, Dec. 2012. ISSN 1530-6984. DOI: 10.1021/nl303758w. Cit. on pp. 30, 63.

32 FINCK, A. D. K. *et al.* Anomalous Modulation of a Zero-Bias Peak in a Hybrid Nanowire-Superconductor Device. **Physical Review Letters**, American Physical Society, v. 110, n. 12, p. 126406, Mar. 2013. DOI: 10.1103/PhysRevLett.110.126406. Cit. on pp. 30, 63.

33 LAW, K. T.; LEE, Patrick A.; NG, T. K. Majorana Fermion Induced Resonant Andreev Reflection. **Physical Review Letters**, American Physical Society, v. 103, n. 23, p. 237001, Dec. 2009. DOI: 10.1103/PhysRevLett.103.237001. Cit. on pp. 30, 100.

34 STANESCU, Tudor D.; LUTCHYN, Roman M.; DAS SARMA, S. Majorana Fermions in Semiconductor Nanowires. **Physical Review B**, American Physical Society, v. 84, n. 14, p. 144522, Oct. 2011. DOI: 10.1103/PhysRevB.84.144522. Cit. on p. 30.

35 CHURCHILL, H. O. H. *et al.* Superconductor-Nanowire Devices from Tunneling to the Multichannel Regime: Zero-Bias Oscillations and Magnetoconductance Crossover. **Physical Review B**, American Physical Society, v. 87, n. 24, p. 241401, June 2013. DOI: 10.1103/PhysRevB.87.241401. Cit. on pp. 30, 63.

36 PIKULIN, D. I. *et al.* A Zero-Voltage Conductance Peak from Weak Antilocalization in a Majorana Nanowire. **New Journal of Physics**, IOP Publishing, v. 14, n. 12, p. 125011, Dec. 2012. ISSN 1367-2630. DOI: 10.1088/1367-2630/14/12/125011. Cit. on p. 30.

37 KONDO Effect in an Integer-Spin Quantum Dot | Nature. Cit. on p. 30.

38 ZAREYAN, M.; BELZIG, W.; NAZAROV, Yu. V. Superconducting Proximity Effect in Clean Ferromagnetic Layers. **Physical Review B**, American Physical Society, v. 65, n. 18, p. 184505, Apr. 2002. DOI: 10.1103/PhysRevB.65.184505. Cit. on p. 30.

39 CHO, Sungjae *et al.* Kondo-like Zero-Bias Conductance Anomaly in a Three-Dimensional Topological Insulator Nanowire. **Scientific Reports**, v. 6, n. 1, p. 21767, Feb. 2016. ISSN 2045-2322. DOI: 10.1038/srep21767. Cit. on p. 30.

40 ZHANG, Hao *et al.* Large Zero-Bias Peaks in InSb-Al Hybrid Semiconductor-Superconductor Nanowire Devices, Jan. 2021. arXiv: 2101.11456 [cond-mat]. Cit. on pp. 30, 100.

41 NEXT Steps of Quantum Transport in Majorana Nanowire Devices | Nature Communications. Cit. on p. 30.

42 ZHAO, Lingfei *et al.* Interference of Chiral Andreev Edge States. **Nature Physics**, Nature Publishing Group, n. 8, p. 1–6, May 2020. ISSN 1745-2481. DOI: 10.1038/s41567-020-0898-5. Cit. on pp. 30, 32, 49, 75–77, 80, 82, 84, 85.

43 SAN-JOSE, P. *et al.* Majorana Zero Modes in Graphene. **Physical Review X**, American Physical Society, v. 5, n. 4, p. 041042, Dec. 2015. DOI: 10.1103/PhysRevX.5.041042. Cit. on pp. 30, 32, 37, 49, 52, 53, 57, 61, 74, 85, 100, 142.

44 MANESCO, A. L. R.; WEBER, G.; RODRIGUES, D. Effective Model for Majorana Modes in Graphene. **Physical Review B**, American Physical Society, v. 100, n. 12, p. 125411, Sept. 2019. DOI: 10.1103/PhysRevB.100.125411. Cit. on pp. 30, 37, 85, 142.

45 MANESCO, Antonio L. R.; FLÓR, Ian Matthias; LIU, Chun-Xiao; AKHMEROV, Anton R. Mechanisms of Andreev Reflection in Quantum Hall Graphene, 11 Mar. 2021. arXiv: 2103.06722 [cond-mat]. Cit. on pp. 30, 49.

46 LEE, Gil-Ho *et al.* Inducing Superconducting Correlation in Quantum Hall Edge States. **Nature Physics**, Nature Publishing Group, v. 13, n. 7, p. 693–698, July 2017. ISSN 1745-2481. DOI: 10.1038/nphys4084. Cit. on pp. 32, 75, 85.

47 GÜL, Önder *et al.* Induced Superconductivity in the Fractional Quantum Hall Edge, Sept. 2020. arXiv: 2009.07836 [cond-mat]. Cit. on pp. 32, 49, 75, 85.

48 GOERBIG, M. O. Electronic Properties of Graphene in a Strong Magnetic Field. **Reviews of Modern Physics**, American Physical Society, v. 83, n. 4, p. 1193–1243, Nov. 2011. DOI: 10.1103/RevModPhys.83.1193. Cit. on pp. 32, 36, 37, 75, 78, 88, 104.

49 YOUNG, A. F. *et al.* Tunable Symmetry Breaking and Helical Edge Transport in a Graphene Quantum Spin Hall State. **Nature**, Nature Publishing Group, v. 505, n. 7484, p. 528–532, Jan. 2014. ISSN 1476-4687. DOI: 10.1038/nature12800. Cit. on pp. 32, 37, 52–54, 57, 88, 104.

50 KHARITONOV, Maxim. Phase Diagram for the $N$=0 Quantum Hall State in Monolayer Graphene. **Physical Review B**, American Physical Society, v. 85, n. 15, p. 155439, Apr. 2012. DOI: 10.1103/PhysRevB.85.155439. Cit. on pp. 32, 37, 88, 104.

51 LADO, J. L.; FERNÁNDEZ-ROSSIER, J. Noncollinear Magnetic Phases and Edge States in Graphene Quantum Hall Bars. **Physical Review B**, American Physical Society, v. 90, n. 16, p. 165429, Oct. 2014. DOI: 10.1103/PhysRevB.90.165429. Cit. on pp. 32, 37, 53, 54, 57, 88.

52 ZHOU, Haoxin *et al.* Strong-Magnetic-Field Magnon Transport in Monolayer Graphene, Feb. 2021. arXiv: 2102.01061 [cond-mat]. Cit. on pp. 32, 37.

53 WALLACE, P. R. The Band Theory of Graphite. **Physical Review**, American Physical Society, v. 71, n. 9, p. 622–634, May 1947. DOI: 10.1103/PhysRev.71.622. Cit. on pp. 33, 88.

54 CASTRO NETO, A. H. *et al.* The Electronic Properties of Graphene. **Reviews of Modern Physics**, American Physical Society, v. 81, n. 1, p. 109–162, Jan. 2009. DOI: 10.1103/RevModPhys.81.109. Cit. on pp. 33, 34, 36, 77, 88.

55 W, AshcroftNeil; ASHCROFT, Neil W.; MERMIN, N. David. **Solid State Physics**. Holt, Rinehart and Winston, 1976. ISBN 978-0-03-083993-1. Cit. on p. 33.

56 AKHMEROV, A. R.; BEENAKKER, C. W. J. Detection of Valley Polarization in Graphene by a Superconducting Contact. **Physical Review Letters**, American Physical Society, v. 98, n. 15, p. 157003, Apr. 2007. ISSN 0031-9007, 1079-7114. DOI: 10.1103/PhysRevLett.98.157003. Cit. on pp. 34, 37, 76, 78, 80.

57 BREY, L.; FERTIG, H. A. Electronic States of Graphene Nanoribbons Studied with the Dirac Equation. **Physical Review B**, American Physical Society, v. 73, n. 23, p. 235411, June 2006. DOI: 10.1103/PhysRevB.73.235411. Cit. on pp. 36, 80.

58 AKHMEROV, A. R.; BEENAKKER, C. W. J. Boundary Conditions for Dirac Fermions on a Terminated Honeycomb Lattice. **Physical Review B**, American Physical Society, v. 77, n. 8, p. 085423, Feb. 2008. DOI: 10.1103/PhysRevB.77.085423. Cit. on pp. 36, 54, 57, 59, 75, 76, 78, 80, 142.

59 NOVOSELOV, K. S. *et al.* Room-Temperature Quantum Hall Effect in Graphene. **Science**, American Association for the Advancement of Science, v. 315, n. 5817, p. 1379–1379, Mar. 2007. ISSN 0036-8075, 1095-9203. DOI: 10.1126/science.1137201. pmid: 17303717. Cit. on pp. 36, 88.

60 V. KLITZING, K.; DORDA, G.; PEPPER, M. New Method for High-Accuracy Determination of the Fine-Structure Constant Based on Quantized Hall Resistance. **Physical Review Letters**, American Physical Society, v. 45, n. 6, p. 494–497, Aug. 1980. DOI: 10.1103/PhysRevLett.45.494. Cit. on pp. 36, 46, 88.

61 LAUGHLIN, R. B. Quantized Hall Conductivity in Two Dimensions. **Physical Review B**, American Physical Society, v. 23, n. 10, p. 5632–5633, May 1981. DOI: 10.1103/PhysRevB.23.5632. Cit. on pp. 36, 88.

62 VON KLITZING, Klaus. The Quantized Hall Effect. **Reviews of Modern Physics**, American Physical Society, v. 58, n. 3, p. 519–531, July 1986. DOI: 10.1103/RevModPhys.58.519. Cit. on pp. 36, 46.

63 NOVOSELOV, K. S. *et al.* Two-Dimensional Gas of Massless Dirac Fermions in Graphene. **Nature**, Nature Publishing Group, v. 438, n. 7065, p. 197–200, Nov. 2005. ISSN 1476-4687. DOI: 10.1038/nature04233. Cit. on pp. 36, 88.

64 ZHANG, Yuanbo; TAN, Yan-Wen; STORMER, Horst L.; KIM, Philip. Experimental Observation of the Quantum Hall Effect and Berry's Phase in Graphene. **Nature**, Nature Publishing Group, v. 438, n. 7065, p. 201–204, Nov. 2005. ISSN 1476-4687. DOI: 10.1038/nature04235. Cit. on p. 36.

65 DATTA, Supriyo. **Electronic Transport in Mesoscopic Systems**. Cambridge: Cambridge University Press, 1995. (Cambridge Studies in Semiconductor Physics and Microelectronic Engineering). ISBN 978-0-521-59943-6. DOI: 10.1017/CBO9780511805776. Cit. on pp. 36, 46.

66 VOZMEDIANO, M. A. H.; KATSNELSON, M. I.; GUINEA, F. Gauge Fields in Graphene. **Physics Reports**, v. 496, n. 4, p. 109–148, 1 Nov. 2010. ISSN 0370-1573. DOI: 10.1016/j.physrep.2010.07.003. Cit. on pp. 37, 89, 101.

67 LÓPEZ-SANCHO, M. Pilar; BREY, Luis. Magnetic Phases in Periodically Rippled Graphene. **Physical Review B**, American Physical Society, v. 94, n. 16, p. 165430, Oct. 2016. DOI: 10.1103/PhysRevB.94.165430. Cit. on pp. 37, 89, 94, 95.

68 TINKHAM, Michael. **Introduction to Superconductivity**. 2nd Revised edition. Mineola, NY: Dover Publications, 14 June 2004. ISBN 978-0-486-43503-9. Cit. on pp. 38, 40.

69 BARDEEN, J.; COOPER, L. N.; SCHRIEFFER, J. R. Theory of Superconductivity. **Physical Review**, American Physical Society, v. 108, n. 5, p. 1175–1204, 1 Dec. 1957. DOI: 10.1103/PhysRev.108.1175. Cit. on p. 38.

70 HEIKKILÄ, Tero T. **The Physics of Nanoelectronics: Transport and Fluctuation Phenomena at Low Temperatures**. Oxford University Press. ISBN 978-0-19-174761-8. Cit. on pp. 38, 40.

71 COOPER, Leon N. Bound Electron Pairs in a Degenerate Fermi Gas. **Physical Review**, American Physical Society, v. 104, n. 4, p. 1189–1190, 15 Nov. 1956. DOI: 10.1103/PhysRev.104.1189. Cit. on p. 38.

72 SATO, Masatoshi; ANDO, Yoichi. Topological Superconductors: A Review. **Reports on Progress in Physics**, IOP Publishing, v. 80, n. 7, p. 076501, May 2017. ISSN 0034-4885. DOI: 10.1088/1361-6633/aa6ac7. Cit. on pp. 39, 52, 62, 65, 66.

73 NAZAROV, Yuli V. **Quantum Transport**. 1ª edição. Cambridge, UK ; New York: Cambridge University Press, 1 May 2009. ISBN 978-0-521-83246-5. Cit. on p. 40.

74 BLONDER, G. E.; TINKHAM, M.; KLAPWIJK, T. M. Transition from Metallic to Tunneling Regimes in Superconducting Microconstrictions: Excess Current, Charge Imbalance, and Supercurrent Conversion. **Physical Review B**, American Physical Society, v. 25, n. 7, p. 4515–4532, 1 Apr. 1982. DOI: 10.1103/PhysRevB.25.4515. Cit. on p. 41.

75 HUBBARD, John H.; WEST, Beverly H. **Differential Equations: A Dynamical Systems Approach: A Dynamical Systems Approach. Part II: Higher Dimensional Systems**. Springer Science & Business Media, 1991. ISBN 978-0-387-94377-0. Cit. on p. 43.

76 NAKAHARA, Mikio. **Geometry, Topology and Physics**. 2º edição: CRC Press, Oct. 2018. Cit. on p. 43.

77 SEIFERT, H.; THRELFALL, W. **Seifert and Threlfall: A Textbook of Topology**. Ed. by Joan S. Birman and Julian Eisner. Trans. by Michael A. Goodman and Wolfgang Heil. New York: Academic Press, 11 June 1980. 437 pp. ISBN 978-0-12-634850-7. Cit. on p. 43.

78 NIJHOLT, B. **Towards realistic numerical simulations of Majorana devices**. 2020. PhD thesis. DOI: 10.4233/UUID:6CDF1184-CE38-412D-A3A5-1A793C787E58. Cit. on p. 44.

79 ALTLAND, Alexander; ZIRNBAUER, Martin R. Nonstandard Symmetry Classes in Mesoscopic Normal-Superconducting Hybrid Structures. **Physical Review B**, American Physical Society, v. 55, n. 2, p. 1142–1161, Jan. 1997. DOI: 10.1103/PhysRevB.55.1142. Cit. on pp. 44, 64, 65.

80 BERRY, Michael Victor. Quantal Phase Factors Accompanying Adiabatic Changes. **Proceedings of the Royal Society of London. A. Mathematical and Physical Sciences**, Royal Society, v. 392, n. 1802, p. 45–57, Mar. 1984. DOI: 10.1098/rspa.1984.0023. Cit. on p. 46.

81 THOULESS, D. J.; KOHMOTO, M.; NIGHTINGALE, M. P.; DEN NIJS, M. Quantized Hall Conductance in a Two-Dimensional Periodic Potential. **Physical Review Letters**, American Physical Society, v. 49, n. 6, p. 405–408, Aug. 1982. DOI: 10.1103/PhysRevLett.49.405. Cit. on p. 47.

82 KANE, C. L.; MELE, E. J. Quantum Spin Hall Effect in Graphene. **Physical Review Letters**, American Physical Society, v. 95, n. 22, p. 226801, Nov. 2005. DOI: 10.1103/PhysRevLett.95.226801. Cit. on pp. 47, 53, 104, 108.

83 KANE, C. L.; MELE, E. J. $\mathbb{Z}_2$ Topological Order and the Quantum Spin Hall Effect. **Physical Review Letters**, American Physical Society, v. 95, n. 14, p. 146802, Sept. 2005. DOI: 10.1103/PhysRevLett.95.146802. Cit. on pp. 47, 104, 108.

84 HEERSCHE, Hubert B. *et al.* Induced Superconductivity in Graphene. **Solid State Communications**, v. 143, n. 1, p. 72–76, July 2007. ISSN 0038-1098. DOI: 10.1016/j.ssc.2007.02.044. Cit. on pp. 49, 75.

85 HEERSCHE, Hubert B. *et al.* Bipolar Supercurrent in Graphene. **Nature**, Nature Publishing Group, v. 446, n. 7131, p. 56–59, Mar. 2007. ISSN 1476-4687. DOI: 10.1038/nature05555. Cit. on pp. 49, 75.

86 LI, Jing *et al.* Superconducting Proximity Effect in a Transparent van Der Waals Superconductor-Metal Junction. **Physical Review B**, American Physical Society, v. 101, n. 19, p. 195405, 5 May 2020. DOI: 10.1103/PhysRevB.101.195405. Cit. on pp. 49, 77, 83, 85.

87 WANG, Joel I-Jan *et al.* Tunneling Spectroscopy of Graphene Nanodevices Coupled to Large-Gap Superconductors. **Physical Review B**, American Physical Society, v. 98, n. 12, p. 121411, Sept. 2018. DOI: 10.1103/PhysRevB.98.121411. Cit. on pp. 49, 75.

88 QIAO, Jia-Bin *et al.* One-Step Synthesis of van Der Waals Heterostructures of Graphene and Two-Dimensional Superconducting $\alpha$-$Mo_2C$. **Physical Review B**, American Physical Society, v. 95, n. 20, p. 201403, May 2017. DOI: 10.1103/PhysRevB.95.201403. Cit. on pp. 49, 75.

89 KE, C. T. *et al.* Anomalous Periodicity of Magnetic Interference Patterns in Encapsulated Graphene Josephson Junctions. **Physical Review Research**, American Physical Society, v. 1, n. 3, p. 033084, Nov. 2019. DOI: 10.1103/PhysRevResearch.1.033084. Cit. on pp. 49, 75.

90 CALADO, Victor E *et al.* Ballistic Josephson Junctions in Edge-Contacted Graphene. **Nature nanotechnology**, Nature Research, v. 10, n. 9, p. 761–764, 2015. DOI: 10.1038/nnano.2015.156. Cit. on pp. 49, 52, 75.

91 TITOV, M.; BEENAKKER, C. W. J. Josephson Effect in Ballistic Graphene. **Physical Review B**, American Physical Society, v. 74, n. 4, p. 041401, July 2006. DOI: 10.1103/PhysRevB.74.041401. Cit. on pp. 49, 57, 58, 75, 78, 83.

92 DU, Xu; SKACHKO, Ivan; ANDREI, Eva Y. Josephson Current and Multiple Andreev Reflections in Graphene SNS Junctions. **Physical Review B**, American Physical Society, v. 77, n. 18, p. 184507, May 2008. DOI: 10.1103/PhysRevB.77.184507. Cit. on pp. 49, 75.

93 BEENAKKER, C. W. J. Specular Andreev Reflection in Graphene. **Physical Review Letters**, American Physical Society, v. 97, n. 6, p. 067007, Aug. 2006. DOI: 10.1103/PhysRevLett.97.067007. Cit. on pp. 49, 57, 78, 83.

94 EFETOV, D. K. *et al.* Specular Interband Andreev Reflections at van Der Waals Interfaces between Graphene and NbSe 2. **Nature Physics**, Nature Publishing Group, v. 12, n. 4, p. 328–332, Apr. 2016. ISSN 1745-2481. DOI: 10.1038/nphys3583. Cit. on p. 49.

95 BHANDARI, Sagar *et al.* Imaging Andreev Reflection in Graphene. **Nano Letters**, American Chemical Society, v. 20, n. 7, p. 4890–4894, July 2020. ISSN 1530-6984. DOI: 10.1021/acs.nanolett.0c00903. Cit. on pp. 49, 75.

96 KESSLER, B. M.; GIRIT, Ç. Ö.; ZETTL, A.; BOUCHIAT, V. Tunable Superconducting Phase Transition in Metal-Decorated Graphene Sheets. **Physical Review Letters**, American Physical Society, v. 104, n. 4, p. 047001, Jan. 2010. DOI: 10.1103/PhysRevLett.104.047001. Cit. on pp. 49, 75.

97 ALLAIN, Adrien; HAN, Zheng; BOUCHIAT, Vincent. Electrical Control of the Superconducting-to-Insulating Transition in Graphene–Metal Hybrids. **Nature Materials**, Nature Publishing Group, v. 11, n. 7, p. 590–594, July 2012. ISSN 1476-4660. DOI: 10.1038/nmat3335. Cit. on pp. 49, 75.

98 SCHMIDT, Felix E. *et al.* A Ballistic Graphene Superconducting Microwave Circuit. **Nature Communications**, Nature Publishing Group, v. 9, n. 1, p. 4069, Oct. 2018. ISSN 2041-1723. DOI: 10.1038/s41467-018-06595-2. Cit. on pp. 49, 75.

99 LEE, Gil-Ho *et al.* Graphene-Based Josephson Junction Microwave Bolometer. **Nature**, Nature Publishing Group, v. 586, n. 7827, p. 42–46, Oct. 2020. ISSN 1476-4687. DOI: 10.1038/s41586-020-2752-4. Cit. on pp. 49, 75.

100 PARK, Geon-Hyoung *et al.* Propagation of Superconducting Coherence via Chiral Quantum-Hall Edge Channels. **Scientific Reports**, Nature Publishing Group, v. 7, n. 1, p. 10953, Sept. 2017. ISSN 2045-2322. DOI: 10.1038/s41598-017-11209-w. Cit. on pp. 49, 75.

101 JACKIW, R.; REBBI, C. Solitons with Fermion Number 1/2. **Physical Review D**, American Physical Society, v. 13, n. 12, p. 3398–3409, June 1976. DOI: 10.1103/PhysRevD.13.3398. Cit. on p. 49.

102 LADO, J. L.; SIGRIST, M. Two-Dimensional Topological Superconductivity with Antiferromagnetic Insulators. **Physical Review Letters**, American Physical Society, v. 121, n. 3, p. 037002, July 2018. DOI: 10.1103/PhysRevLett.121.037002. Cit. on pp. 49, 53, 142.

103 LADO, J. L.; SIGRIST, M. Solitonic In-Gap Modes in a Superconductor-Quantum Antiferromagnet Interface. **Physical Review Research**, American Physical Society, v. 2, n. 2, p. 023347, June 2020. DOI: 10.1103/PhysRevResearch.2.023347. Cit. on p. 49.

104 LUNTAMA, Senna S.; TÖRMÄ, Päivi; LADO, Jose L. Interaction-Induced Topological Superconductivity in Antiferromagnet-Superconductor Junctions. **Physical Review Research**, American Physical Society, v. 3, n. 1, p. l012021, 5 Mar. 2021. DOI: 10.1103/PhysRevResearch.3.L012021. Cit. on p. 49.

105 LEIJNSE, Martin; FLENSBERG, Karsten. Introduction to Topological Superconductivity and Majorana Fermions. **Semiconductor Science and Technology**, v. 27, n. 12, p. 124003, 2012. Cit. on p. 52.

106 BEENAKKER, C.w.j. Search for Majorana Fermions in Superconductors. **Annual Review of Condensed Matter Physics**, Annual Reviews, v. 4, n. 1, p. 113–136, Mar. 2013. ISSN 1947-5454. DOI: 10.1146/annurev-conmatphys-030212-184337. eprint: https://doi.org/10.1146/annurev-conmatphys-030212-184337. Cit. on p. 52.

107 ELLIOTT, Steven R.; FRANZ, Marcel. Colloquium: Majorana Fermions in Nuclear, Particle, and Solid-State Physics. **Reviews of Modern Physics**, American Physical Society, v. 87, n. 1, p. 137–163, Feb. 2015. DOI: 10.1103/RevModPhys.87.137. Cit. on p. 52.

108 MAJORANA Quasiparticles in Condensed Matter. **La Rivista del Nuovo Cimento**, v. 40, n. 11, p. 523–593, 30 Oct. 2017. ISSN 0393697X, 0393697X. DOI: 10.1393/ncr/i2017-10141-9. Cit. on p. 52.

109 HE, Qing Lin *et al.* Chiral Majorana Fermion Modes in a Quantum Anomalous Hall Insulator–Superconductor Structure. **Science**, American Association for the Advancement of Science, v. 357, n. 6348, p. 294–299, 2017. ISSN 0036-8075. DOI: 10.1126/science.aag2792. eprint: http://science.sciencemag.org/content/357/6348/294.full.pdf. Cit. on p. 52.

110 ZHANG, Hao *et al.* Quantized Majorana Conductance. **Nature**, Nature Publishing Group, v. 556, n. 7699, p. 74, 2018. DOI: 10.1038/nature26142. Cit. on p. 52.

111 BANERJEE, Mitali *et al.* Observation of Half-Integer Thermal Hall Conductance. **Nature**, Nature Publishing Group, p. 1, 2018. DOI: 10.1038/s41586-018-0184-1. Cit. on p. 52.

112 KASAHARA, Y *et al.* Majorana Quantization and Half-Integer Thermal Quantum Hall Effect in a Kitaev Spin Liquid. **Nature**, Nature Publishing Group, 2018. DOI: 10.1038/s41586-018-0274-0. Cit. on p. 52.

113 FU, Liang; KANE, C. L. Josephson Current and Noise at a Superconductor/Quantum-Spin-Hall-Insulator/Superconductor Junction. **Physical Review B**, American Physical Society, v. 79, n. 16, p. 161408, Apr. 2009. DOI: 10.1103/PhysRevB.79.161408. Cit. on pp. 52, 53.

114 AKHMEROV, A. R.; NILSSON, Johan; BEENAKKER, C. W. J. Electrically Detected Interferometry of Majorana Fermions in a Topological Insulator. **Physical Review Letters**, American Physical Society, v. 102, n. 21, p. 216404, May 2009. DOI: 10.1103/PhysRevLett.102.216404. Cit. on p. 52.

115 STANESCU, T D; TEWARI, S. Majorana Fermions in Semiconductor Nanowires: Fundamentals, Modeling, and Experiment. **Journal of Physics: Condensed Matter**, v. 25, n. 23, p. 233201, 2013. Cit. on p. 52.

116 DUMITRESCU, Eugene *et al.* Majorana Fermions in Chiral Topological Ferromagnetic Nanowires. **Physical Review B**, APS, v. 91, n. 9, p. 094505, 2015. DOI: 10.1103/PhysRevB.91.094505. Cit. on pp. 52, 63, 64, 68, 73, 74.

117 YOUNG, A. F. *et al.* Spin and Valley Quantum Hall Ferromagnetism in Graphene. **Nature Physics**, Springer Science and Business Media LLC, v. 8, n. 7, p. 550–556, May 2012. DOI: 10.1038/nphys2307. Cit. on pp. 52–54, 57, 88.

118 BEN SHALOM, M. *et al.* Quantum Oscillations of the Critical Current and High-Field Superconducting Proximity in Ballistic Graphene. **Nature Physics**, Nature Publishing Group, v. 12, n. 4, p. 318–322, Apr. 2016. ISSN 1745-2481. DOI: 10.1038/nphys3592. Cit. on p. 52.

119 GOERBIG, Mark O. The Quantum Hall Effect in Graphene – a Theoretical Perspective. **Comptes Rendus Physique**, v. 12, n. 4, p. 369–378, 2011. ISSN 1631-0705. DOI: 10.1016/j.crhy.2011.04.012. Cit. on p. 53.

120 BERNEVIG, B. Andrei; HUGHES, Taylor L.; ZHANG, Shou-Cheng. The Quantum Hall Effect in Graphene from a Lattice Perspective. **Solid State Communications**, v. 143, n. 1, p. 20–26, 2007. ISSN 0038-1098. DOI: 10.1016/j.ssc.2007.04.031. Cit. on p. 53.

121 LADO, J.L.; GARCÍA-MARTÍNEZ, N.; FERNÁNDEZ-ROSSIER, J. Edge States in Graphene-like Systems. **Synthetic Metals**, v. 210, p. 56–67, 2015. ISSN 0379-6779. DOI: 10.1016/j.synthmet.2015.06.026. Cit. on p. 53.

122 KHARITONOV, Maxim. Edge Excitations of the Canted Antiferromagnetic Phase of the $\nu = 0$ Quantum Hall State in Graphene: A Simplified Analysis. **Physical Review B**, American Physical Society, v. 86, n. 7, p. 075450, Aug. 2012. DOI: 10.1103/PhysRevB.86.075450. Cit. on pp. 53, 54, 57, 88.

123 BENA, Cristina. Testing the Formation of Majorana States Using Majorana Polarization. **Comptes Rendus Physique**, v. 18, n. 5, p. 349–357, 2017. ISSN 1631-0705. DOI: 10.1016/j.crhy.2017.09.005. Cit. on pp. 55, 56.

124 STICLET, Doru; BENA, Cristina; SIMON, Pascal. Spin and Majorana Polarization in Topological Superconducting Wires. **Physical Review Letters**, American Physical Society, v. 108, n. 9, p. 096802, Mar. 2012. DOI: 10.1103/PhysRevLett.108.096802. Cit. on pp. 55, 56.

125 GROTH, Christoph W; WIMMER, Michael; AKHMEROV, Anton R; WAINTAL, Xavier. Kwant: A Software Package for Quantum Transport. **New Journal of Physics**, IOP Publishing, v. 16, n. 6, p. 063065, 2014. Cit. on pp. 55, 57, 71, 77.

126 DIVINCENZO, D. P.; MELE, E. J. Self-Consistent Effective-Mass Theory for Intralayer Screening in Graphite Intercalation Compounds. **Physical Review B**, American Physical Society, v. 29, n. 4, p. 1685–1694, Feb. 1984. DOI: 10.1103/PhysRevB.29.1685. Cit. on pp. 57, 58.

127 MCCANN, Edward; FAL'KO, Vladimir I. Symmetry of Boundary Conditions of the Dirac Equation for Electrons in Carbon Nanotubes. **Journal of Physics: Condensed Matter**, v. 16, n. 13, p. 2371, 2004. Cit. on p. 59.

128 MAJORANA, Ettore. Teoria Simmetrica Dell'elettrone e Del Positrone. **Il Nuovo Cimento (1924-1942)**, Springer, v. 14, n. 4, p. 171, 1937. Cit. on p. 62.

129 READ, N.; GREEN, Dmitry. Paired States of Fermions in Two Dimensions with Breaking of Parity and Time-Reversal Symmetries and the Fractional Quantum Hall Effect. **Physical Review B**, American Physical Society, v. 61, n. 15, p. 10267–10297, 0 pp., Apr. 2000. DOI: 10.1103/PhysRevB.61.10267. Cit. on p. 62.

130 LUTCHYN, Roman M; SAU, Jay D; SARMA, S Das. Majorana Fermions and a Topological Phase Transition in Semiconductor-Superconductor Heterostructures. **Physical Review Letters**, APS, v. 105, n. 7, p. 077001, 2010. Cit. on pp. 63, 100.

131 ALICEA, Jason. Majorana Fermions in a Tunable Semiconductor Device. **Physical Review B**, APS, v. 81, n. 12, p. 125318, 2010. DOI: 10.1103/PhysRevB.81.125318. Cit. on p. 63.

132 SAU, Jay D; LUTCHYN, Roman M; TEWARI, Sumanta; SARMA, S Das. Generic New Platform for Topological Quantum Computation Using Semiconductor Heterostructures. **Physical Review Letters**, APS, v. 104, n. 4, p. 040502, 2010. DOI: 10.1103/PhysRevLett.104.040502. Cit. on p. 63.

133 GÜL, Önder *et al.* Ballistic Majorana Nanowire Devices. **Nature Nanotechnology**, Nature Publishing Group, v. 13, n. 3, p. 192–197, 3 Mar. 2018. ISSN 1748-3395. DOI: 10.1038/s41565-017-0032-8. Cit. on p. 63.

134 DAS, Anindya *et al.* Zero-Bias Peaks and Splitting in an Al-InAs Nanowire Topological Superconductor as a Signature of Majorana Fermions. **Nature Physics**, Nature Publishing Group, v. 8, n. 12, p. 887–895, 2012. Cit. on p. 63.

135 ALBRECHT, Sven Marian *et al.* Exponential Protection of Zero Modes in Majorana Islands. **Nature**, Nature Publishing Group, v. 531, n. 7593, p. 206–209, 2016. Cit. on p. 63.

136 CHEN, Jun *et al.* Experimental Phase Diagram of a One-Dimensional Topological Superconductor, 2016. arXiv: 1610.04555. Cit. on p. 63.

137 DUMITRESCU, E; TEWARI, Sumanta. Topological Properties of the Time-Reversal-Symmetric Kitaev Chain and Applications to Organic Superconductors. **Physical Review B**, APS, v. 88, n. 22, p. 220505, 2013. DOI: 10.1103/PhysRevB.88.220505. Cit. on pp. 63, 64, 68.

138 KITAEV, Alexei; LEBEDEV, Vladimir; FEIGEL'MAN, Mikhail. Periodic Table for Topological Insulators and Superconductors. In: AIP, 1. AIP Conference Proceedings. 2009. v. 1134, p. 22–30. Cit. on pp. 63–65.

139 BUDICH, Jan Carl; TRAUZETTEL, Björn. From the Adiabatic Theorem of Quantum Mechanics to Topological States of Matter. **physica status solidi (RRL)-Rapid Research Letters**, Wiley Online Library, v. 7, n. 1-2, p. 109–129, 2013. Cit. on pp. 63, 64.

140 DUMITRESCU, Eugene; STANESCU, Tudor D.; TEWARI, Sumanta. Hidden-Symmetry Decoupling of Majorana Bound States in Topological Superconductors. **Physical Review B**, American Physical Society, v. 91, n. 12, p. 121413, Mar. 2015. DOI: 10.1103/PhysRevB.91.121413. Cit. on pp. 63–66, 68, 69, 74.

141 BUDICH, Jan Carl; ARDONNE, Eddy. Topological Invariant for Generic One-Dimensional Time-Reversal-Symmetric Superconductors in Class DIII. **Physical Review B**, American Physical Society, v. 88, n. 13, p. 134523, 5 pp., Oct. 2013. DOI: 10.1103/PhysRevB.88.134523. Cit. on pp. 63, 66.

142 MANESCO, A. L. R.; WEBER, G.; RODRIGUES, D. One-Dimensional p-Wave Superconductor Toy-Model for Majorana Fermions in Multiband Semiconductor Nanowires. **IEEE Transactions on Applied Superconductivity**, v. 28, n. 4, p. 1–5, June 2018. ISSN 1558-2515. DOI: 10.1109/TASC.2018.2807361. Cit. on pp. 63, 68.

143 LUTCHYN, Roman M; STANESCU, Tudor D; SARMA, S Das. Search for Majorana Fermions in Multiband Semiconducting Nanowires. **Physical Review Letters**, APS, v. 106, n. 12, p. 127001, 2011. DOI: 10.1103/PhysRevLett.106.127001. Cit. on p. 63.

144 LIM, Jong Soo; SERRA, Llorenç; LÓPEZ, Rosa; AGUADO, Ramón. Magnetic-Field Instability of Majorana Modes in Multiband Semiconductor Wires. **Physical Review B**, APS, v. 86, n. 12, p. 121103, 2012. DOI: 10.1103/PhysRevB.86.121103. Cit. on p. 63.

145 LUTCHYN, Roman M; FISHER, Matthew PA. Interacting Topological Phases in Multiband Nanowires. **Physical Review B**, APS, v. 84, n. 21, p. 214528, 2011. DOI: 10.1103/PhysRevB.84.214528. Cit. on p. 63.

146 DEGOTTARDI, Wade; THAKURATHI, Manisha; VISHVESHWARA, Smitha; SEN, Diptiman. Majorana Fermions in Superconducting Wires: Effects of Long-Range Hopping, Broken Time-Reversal Symmetry, and Potential Landscapes. **Physical Review B**, APS, v. 88, n. 16, p. 165111, 2013. Cit. on p. 63.

147 ALECCE, Antonio; DELL'ANNA, Luca. Extended Kitaev Chain with Longer-Range Hopping and Pairing. **Physical Review B**, American Physical Society, v. 95, n. 19, p. 195160, 14 pp., May 2017. DOI: 10.1103/PhysRevB.95.195160. Cit. on p. 63.

148 LIU, Chun-Xiao; SAU, Jay D.; DAS SARMA, S. Role of Dissipation in Realistic Majorana Nanowires. **Physical Review B**, American Physical Society, v. 95, n. 5, p. 054502, 5 pp., Feb. 2017. DOI: 10.1103/PhysRevB.95.054502. Cit. on p. 63.

149 CHENG, Meng; TU, Hong-Hao. Majorana Edge States in Interacting Two-Chain Ladders of Fermions. **Physical Review B**, APS, v. 84, n. 9, p. 094503, 2011. DOI: 10.1103/PhysRevB.84.094503. Cit. on p. 63.

150 NAKAI, Ryota; RYU, Shinsei; FURUSAKI, Akira. Time-Reversal Symmetric Kitaev Model and Topological Superconductor in Two Dimensions. **Physical Review B**, APS, v. 85, n. 15, p. 155119, 2012. DOI: 10.1103/PhysRevB.85.155119. Cit. on p. 63.

151 WAKATSUKI, Ryohei; EZAWA, Motohiko; NAGAOSA, Naoto. Majorana Fermions and Multiple Topological Phase Transition in Kitaev Ladder Topological Superconductors. **Physical Review B**, APS, v. 89, n. 17, p. 174514, 2014. DOI: 10.1103/PhysRevB.89.174514. Cit. on p. 63.

152 CONTINENTINO, Mucio A; DEUS, Fernanda; PADILHA, Igor T; CALDAS, Heron. Topological Transitions in Multi-Band Superconductors. **Annals of Physics**, Elsevier, v. 348, p. 1–14, 2014. Cit. on p. 63.

153 POTTER, Andrew C; LEE, Patrick A. Majorana End States in Multiband Microstructures with Rashba Spin-Orbit Coupling. **Physical Review B**, APS, v. 83, n. 9, p. 094525, 2011. DOI: 10.1103/PhysRevB.83.094525. Cit. on p. 63.

154 MACHADO, AJS *et al.* Evidence for Topological Behavior in Superconducting Cu x ZrTe 2- y. **Physical Review B**, APS, v. 95, n. 14, p. 144505, 2017. DOI: 10.1103/PhysRevB.95.144505. Cit. on p. 63.

155 ZIRNBAUER, Martin R. Symmetry Classes, 2010. arXiv: 1001.0722. Cit. on p. 64.

156 SCHNYDER, Andreas P; RYU, Shinsei; FURUSAKI, Akira; LUDWIG, Andreas WW. Classification of Topological Insulators and Superconductors in Three Spatial Dimensions. **Physical Review B**, APS, v. 78, n. 19, p. 195125, 2008. Cit. on p. 64.

157 TEWARI, Sumanta; SAU, Jay D. Topological Invariants for Spin-Orbit Coupled Superconductor Nanowires. **Physical Review Letters**, APS, v. 109, n. 15, p. 150408, 2012. DOI: 10.1103/PhysRevLett.109.150408. Cit. on pp. 64–66.

158 SATO, Masatoshi; TANAKA, Yukio; YADA, Keiji; YOKOYAMA, Takehito. Topology of Andreev Bound States with Flat Dispersion. **Physical Review B**, APS, v. 83, n. 22, p. 224511, 2011. DOI: 10.1103/PhysRevB.83.224511. Cit. on p. 66.

159 SEDLMAYR, N; GUIGOU, M; SIMON, P; BENA, C. Majoranas with and without a 'Character': Hybridization, Braiding and Chiral Majorana Number. **Journal of Physics: Condensed Matter**, IOP Publishing, v. 27, n. 45, p. 455601, 2015. Cit. on p. 66.

160 WEINBERG, Steven. **The Quantum Theory of Fields**. Cambridge university press, 1995. v. 2. Cit. on p. 66.

161 BYCHKOV, Yu A; RASHBA, Emmanuel I. Oscillatory Effects and the Magnetic Susceptibility of Carriers in Inversion Layers. **Journal of physics C: Solid state physics**, IOP Publishing, v. 17, n. 33, p. 6039, 1984. Cit. on p. 67.

162 COLEMAN, Piers. **Introduction to Many-Body Physics**. Cambridge University Press, 2015. Cit. on p. 67.

163 FLINT, Rebecca; COLEMAN, P. Symplectic N and Time Reversal in Frustrated Magnetism. **Physical Review B**, American Physical Society, v. 79, n. 1, p. 014424, 16 pp., Jan. 2009. DOI: 10.1103/PhysRevB.79.014424. Cit. on p. 69.

164 MANESCO, Antônio L. R.; WEBER, Gabriel; RODRIGUES, Durval. Hidden Chiral Symmetries in BDI Multichannel Kitaev Chains. **Journal of Physics: Condensed Matter**, v. 30, n. 17, p. 175401, Apr. 2018. ISSN 0953-8984. DOI: 10.1088/1361-648X/aab722. Cit. on p. 74.

165 BREY, Luis; FERTIG, H. A. Edge States and the Quantized Hall Effect in Graphene. **Physical Review B**, American Physical Society, v. 73, n. 19, p. 195408, May 2006. DOI: 10.1103/PhysRevB.73.195408. Cit. on pp. 75, 80.

166 LIU, Ming-Hao *et al.* Scalable Tight-Binding Model for Graphene. **Physical Review Letters**, American Physical Society, v. 114, n. 3, p. 036601, Jan. 2015. DOI: 10.1103/PhysRevLett.114.036601. Cit. on pp. 77, 90, 107.

167 MANESCO, Antonio L. R.; FLÓR, I. M.; LIU, Chun-Xiao; AKHMEROV, Anton R. **Mechanisms of Andreev Reflection in Quantum Hall Graphene**. Zenodo, Mar. 2021. DOI: 10.5281/zenodo.4597080. Cit. on p. 78.

168 NIJHOLT, Bas; WESTON, Joseph; HOOFWIJK, Jorn; AKHMEROV, Anton. *Adaptive*: Parallel Active Learning of Mathematical Functions. Zenodo, 2019. DOI: 10.5281/zenodo.1182437. Cit. on p. 78.

169 COLOMÉS, E.; FRANZ, M. Antichiral Edge States in a Modified Haldane Nanoribbon. **Physical Review Letters**, American Physical Society, v. 120, n. 8, p. 086603, Feb. 2018. DOI: 10.1103/PhysRevLett.120.086603. Cit. on pp. 78, 92, 93, 102.

170 RAMIRES, Aline; LADO, Jose L. Electrically Tunable Gauge Fields in Tiny-Angle Twisted Bilayer Graphene. **Physical Review Letters**, American Physical Society, v. 121, n. 14, p. 146801, Oct. 2018. DOI: 10.1103/PhysRevLett.121.146801. Cit. on pp. 78, 89, 92, 93, 102.

171 NAKADA, Kyoko; FUJITA, Mitsutaka; DRESSELHAUS, Gene; DRESSELHAUS, Mildred S. Edge State in Graphene Ribbons: Nanometer Size Effect and Edge Shape Dependence. **Physical Review B**, American Physical Society, v. 54, n. 24, p. 17954–17961, Dec. 1996. DOI: 10.1103/PhysRevB.54.17954. Cit. on p. 80.

172 THOULESS, D. J. Quantization of Particle Transport. **Physical Review B**, American Physical Society, v. 27, n. 10, p. 6083–6087, May 1983. DOI: 10.1103/PhysRevB.27.6083. Cit. on p. 88.

173 STEPANOV, Petr *et al.* Long-Distance Spin Transport through a Graphene Quantum Hall Antiferromagnet. **Nature Physics**, Springer Science and Business Media LLC, v. 14, n. 9, p. 907–911, June 2018. DOI: 10.1038/s41567-018-0161-5. Cit. on p. 88.

174 AMORIM, B. *et al.* Novel Effects of Strains in Graphene and Other Two Dimensional Materials. **Physics Reports**, v. 617, p. 1–54, Mar. 2016. ISSN 0370-1573. DOI: 10.1016/j.physrep.2015.12.006. Cit. on p. 89.

175 LEVY, N. *et al.* Strain-Induced Pseudo–Magnetic Fields Greater Than 300 Tesla in Graphene Nanobubbles. **Science**, v. 329, n. 5991, p. 544–547, July 2010. ISSN 0036-8075, 1095-9203. DOI: 10.1126/science.1191700. pmid: 20671183. Cit. on p. 89.

176 MORPURGO, A. F.; GUINEA, F. Intervalley Scattering, Long-Range Disorder, and Effective Time-Reversal Symmetry Breaking in Graphene. **Physical Review Letters**, v. 97, n. 19, p. 196804, Nov. 2006. DOI: 10.1103/PhysRevLett.97.196804. Cit. on p. 89.

177 MENG, Lan *et al.* Strain-Induced One-Dimensional Landau Level Quantization in Corrugated Graphene. **Physical Review B**, v. 87, n. 20, p. 205405, May 2013. DOI: 10.1103/PhysRevB.87.205405. Cit. on pp. 89, 97.

178 GUINEA, F.; KATSNELSON, M. I.; VOZMEDIANO, M. A. H. Midgap States and Charge Inhomogeneities in Corrugated Graphene. **Physical Review B**, v. 77, n. 7, p. 075422, Feb. 2008. DOI: 10.1103/PhysRevB.77.075422. Cit. on p. 89.

179 RAMEZANI MASIR, M.; MOLDOVAN, D.; PEETERS, F.M. Pseudo Magnetic Field in Strained Graphene: Revisited. **Solid State Communications**, v. 175-176, p. 76–82, 2013. ISSN 0038-1098. DOI: 10.1016/j.ssc.2013.04.001. Cit. on pp. 89, 101.

180 SAN-JOSE, P.; GONZÁLEZ, J.; GUINEA, F. Non-Abelian Gauge Potentials in Graphene Bilayers. **Physical Review Letters**, American Physical Society, v. 108, n. 21, p. 216802, May 2012. DOI: 10.1103/PhysRevLett.108.216802. Cit. on p. 89.

181 SUÁREZ MORELL, E. *et al.* Flat Bands in Slightly Twisted Bilayer Graphene: Tight-Binding Calculations. **Physical Review B**, American Physical Society, v. 82, n. 12, p. 121407, Sept. 2010. DOI: 10.1103/PhysRevB.82.121407. Cit. on p. 89.

182 LIU, Jianpeng; LIU, Junwei; DAI, Xi. Pseudo Landau Level Representation of Twisted Bilayer Graphene: Band Topology and Implications on the Correlated Insulating Phase. **Physical Review B**, American Physical Society, v. 99, n. 15, p. 155415, Apr. 2019. DOI: 10.1103/PhysRevB.99.155415. Cit. on p. 89.

183 WOLF, T. M. R.; LADO, J. L.; BLATTER, G.; ZILBERBERG, O. Electrically Tunable Flat Bands and Magnetism in Twisted Bilayer Graphene. **Physical Review Letters**, American Physical Society, v. 123, n. 9, p. 096802, Aug. 2019. DOI: 10.1103/PhysRevLett.123.096802. Cit. on pp. 89, 90, 92, 106.

184 GONZALEZ-ARRAGA, Luis A.; LADO, J. L.; GUINEA, Francisco; SAN-JOSE, Pablo. Electrically Controllable Magnetism in Twisted Bilayer Graphene. **Physical Review Letters**, v. 119, n. 10, p. 107201, Sept. 2017. DOI: 10.1103/PhysRevLett.119.107201. Cit. on pp. 89, 90.

185 VIANA-GOMES, J.; PEREIRA, Vitor M.; PERES, N. M. R. Magnetism in Strained Graphene Dots. **Physical Review B**, v. 80, n. 24, p. 245436, Dec. 2009. DOI: 10.1103/PhysRevB.80.245436. Cit. on p. 89.

186 SHARMA, Anand; KOTOV, Valeri N.; CASTRO NETO, Antonio H. Effect of Uniaxial Strain on Ferromagnetic Instability and Formation of Localized Magnetic States on Adatoms in Graphene. **Physical Review B**, v. 87, n. 15, p. 155431, Apr. 2013. DOI: 10.1103/PhysRevB.87.155431. Cit. on p. 89.

187 CODECIDO, Emilio *et al.* Correlated Insulating and Superconducting States in Twisted Bilayer Graphene below the Magic Angle. **Science Advances**, v. 5, n. 9, eaaw9770, Sept. 2019. ISSN 2375-2548. DOI: 10.1126/sciadv.aaw9770. Cit. on p. 89.

188 TSAI, Kan-Ting *et al.* Correlated Superconducting and Insulating States in Twisted Trilayer Graphene Moire of Moire Superlattices. **arXiv e-prints**, arXiv:1912.03375, Dec. 2019. arXiv: 1912.03375 [cond-mat.mes-hall]. Cit. on p. 89.

189 LIU, Xiaomeng *et al.* Tunable Spin-Polarized Correlated States in Twisted Double Bilayer Graphene. **Nature**, Nature Publishing Group, v. 583, n. 7815, arXiv:1903.08130, p. 221–225, 7815 July 2020. ISSN 1476-4687. DOI: 10.1038/s41586-020-2458-7. Cit. on pp. 89, 101.

190 AN, Liheng *et al.* Interaction Effects and Superconductivity Signatures in Twisted Double-Bilayer $WSe_2$. **arXiv e-prints**, arXiv:1907.03966, July 2019. Cit. on p. 89.

191 REGAN, Emma C. *et al.* Mott and Generalized Wigner Crystal States in $WSe_2/WS_2$ Moiré Superlattices. **Nature**, Nature Publishing Group, v. 579, n. 7799, p. 359–363, 7799 Mar. 2020. ISSN 1476-4687. DOI: 10.1038/s41586-020-2092-4. Cit. on p. 89.

192 MILOVANOVIĆ, S. P.; ANĐELKOVIĆ, M.; COVACI, L.; PEETERS, F. M. Band Flattening in Buckled Monolayer Graphene. **Physical Review B**, American Physical Society, v. 102, n. 24, p. 245427, 28 Dec. 2020. DOI: 10.1103/PhysRevB.102.245427. Cit. on pp. 89, 91, 101.

193 MANESCO, Antonio L. R. *et al.* **Correlations in the Elastic Landau Level of a Graphene/NbSe2 van Der Waals Heterostructure**. Zenodo, Mar. 2020. DOI: 10.5281/zenodo.3829056. Cit. on p. 90.

194 SCHÜLER, M. *et al.* Optimal Hubbard Models for Materials with Nonlocal Coulomb Interactions: Graphene, Silicene, and Benzene. **Physical Review Letters**, American Physical Society, v. 111, n. 3, p. 036601, July 2013. DOI: 10.1103/PhysRevLett.111.036601. Cit. on pp. 90, 92, 96, 106.

195 CHEN, Kuang-Ting; LEE, Patrick A. Unified Formalism for Calculating Polarization, Magnetization, and More in a Periodic Insulator. **Physical Review B**, American Physical Society, v. 84, n. 20, p. 205137, Nov. 2011. DOI: 10.1103/PhysRevB.84.205137. Cit. on pp. 92, 106.

196 RAMIRES, Aline; LADO, Jose L. Impurity-Induced Triple Point Fermions in Twisted Bilayer Graphene. **Physical Review B**, American Physical Society, v. 99, n. 24, p. 245118, June 2019. DOI: 10.1103/PhysRevB.99.245118. Cit. on pp. 92, 93.

197 GEORGI, Alexander *et al.* Tuning the Pseudospin Polarization of Graphene by a Pseudomagnetic Field. **Nano Letters**, v. 17, n. 4, p. 2240–2245, 2017. DOI: 10.1021/acs.nanolett.6b04870. eprint: https://doi.org/10.1021/acs.nanolett.6b04870. Cit. on pp. 94, 95.

198 LIEB, Elliott H. Two Theorems on the Hubbard Model. **Physical Review Letters**, American Physical Society, v. 62, n. 10, p. 1201–1204, Mar. 1989. DOI: 10.1103/PhysRevLett.62.1201. Cit. on p. 94.

199 GANI, Yohanes S.; WALTER, Eric J.; ROSSI, Enrico. Proximity-Induced Spin-Orbit Splitting in Graphene Nanoribbons on Transition-Metal Dichalcogenides. **Physical Review B**, American Physical Society, v. 101, n. 19, p. 195416, 11 May 2020. DOI: 10.1103/PhysRevB.101.195416. Cit. on p. 97.

200 MANESCO, Antonio L. R.; LADO, Jose L. **Correlation-induced valley topology in buckled graphene superlattices**. Zenodo, Apr. 2021. DOI: 10.5281/zenodo.4685133. Cit. on p. 100.

201 WU, Fengcheng; LOVORN, Timothy; TUTUC, Emanuel; MACDONALD, A. H. Hubbard Model Physics in Transition Metal Dichalcogenide Moiré Bands. **Physical Review Letters**, American Physical Society, v. 121, n. 2, p. 026402, 10 July 2018. DOI: 10.1103/PhysRevLett.121.026402. Cit. on p. 100.

202 CHEN, Po-Yen *et al.* Tunable Moiré Superlattice of Artificially Twisted Monolayers. **Advanced Materials**, v. 31, n. 37, p. 1901077, 2019. ISSN 1521-4095. DOI: 10.1002/adma.201901077. Cit. on p. 100.

203 LADO, Jose L.; LILJEROTH, Peter. Designer Quantum Matter in van Der Waals Heterostructures, 23 Feb. 2021. arXiv: 2102.11779 [cond-mat]. Cit. on p. 100.

204 ANDREI, Eva Y. *et al.* The Marvels of Moiré Materials. **Nature Reviews Materials**, Nature Publishing Group, v. 6, n. 3, p. 201–206, 3 Mar. 2021. ISSN 2058-8437. DOI: 10.1038/s41578-021-00284-1. Cit. on pp. 100, 101.

205 ZHANG, Hao; LIU, Dong E.; WIMMER, Michael; KOUWENHOVEN, Leo P. Next Steps of Quantum Transport in Majorana Nanowire Devices. **Nature Communications**, Nature Publishing Group, v. 10, n. 1, p. 5128, 1 12 Nov. 2019. ISSN 2041-1723. DOI: 10.1038/s41467-019-13133-1. Cit. on p. 100.

206 KEZILEBIEKE, Shawulienu *et al.* Topological superconductivity in a van der Waals heterostructure. **Nature**, Nature Publishing Group, v. 588, n. 7838, p. 424–428, 2020. Cit. on p. 100.

207 OREG, Yuval; REFAEL, Gil; VON OPPEN, Felix. Helical Liquids and Majorana Bound States in Quantum Wires. **Physical Review Letters**, American Physical Society, v. 105, n. 17, p. 177002, 20 Oct. 2010. DOI: 10.1103/PhysRevLett.105.177002. Cit. on p. 100.

208 FU, Liang; KANE, C. L. Superconducting Proximity Effect and Majorana Fermions at the Surface of a Topological Insulator. **Physical Review Letters**, American Physical Society, v. 100, n. 9, p. 096407, 6 Mar. 2008. DOI: 10.1103/PhysRevLett.100.096407. Cit. on p. 100.

209 SONG, Zhida *et al.* All Magic Angles in Twisted Bilayer Graphene Are Topological. **Physical Review Letters**, American Physical Society, v. 123, n. 3, p. 036401, 16 July 2019. DOI: 10.1103/PhysRevLett.123.036401. Cit. on p. 101.

210 XIE, Fang; SONG, Zhida; LIAN, Biao; BERNEVIG, B. Andrei. Topology-Bounded Superfluid Weight in Twisted Bilayer Graphene. **Physical Review Letters**, American Physical Society, v. 124, n. 16, p. 167002, 24 Apr. 2020. DOI: 10.1103/PhysRevLett.124.167002. Cit. on p. 101.

211 DA LIAO, Yuan *et al.* Correlation-Induced Insulating Topological Phases at Charge Neutrality in Twisted Bilayer Graphene. **Physical Review X**, American Physical Society, v. 11, n. 1, p. 011014, 22 Jan. 2021. DOI: 10.1103/PhysRevX.11.011014. Cit. on p. 101.

212 CHOI, Youngjoon *et al.* Correlation-Driven Topological Phases in Magic-Angle Twisted Bilayer Graphene. **Nature**, Nature Publishing Group, v. 589, n. 7843, p. 536–541, 7843 Jan. 2021. ISSN 1476-4687. DOI: 10.1038/s41586-020-03159-7. Cit. on p. 101.

213 KAUPPILA, V. J.; AIKEBAIER, F.; HEIKKILÄ, T. T. Flat-Band Superconductivity in Strained Dirac Materials. **Physical Review B**, American Physical Society, v. 93, n. 21, p. 214505, 13 June 2016. DOI: 10.1103/PhysRevB.93.214505. Cit. on p. 101.

214 KOPNIN, N. B.; HEIKKILÄ, T. T.; VOLOVIK, G. E. High-Temperature Surface Superconductivity in Topological Flat-Band Systems. **Physical Review B**, American Physical Society, v. 83, n. 22, p. 220503, 8 June 2011. DOI: 10.1103/PhysRevB.83.220503. Cit. on p. 101.

215 TANG, Evelyn; FU, Liang. Strain-Induced Partially Flat Band, Helical Snake States and Interface Superconductivity in Topological Crystalline Insulators. **Nature Physics**, Nature Publishing Group, v. 10, n. 12, p. 964–969, 12 Dec. 2014. ISSN 1745-2481. DOI: 10.1038/nphys3109. Cit. on p. 101.

216 GANI, Yohanes S.; STEINBERG, Hadar; ROSSI, Enrico. Superconductivity in Twisted Graphene $NbSe_2$ Heterostructures. **Physical Review B**, American Physical Society, v. 99, n. 23, p. 235404, June 2019. DOI: 10.1103/PhysRevB.99.235404. Cit. on p. 101.

217 SHEN, Cheng *et al.* Correlated States in Twisted Double Bilayer Graphene. **Nature Physics**, Nature Publishing Group, v. 16, n. 5, p. 520–525, 5 May 2020. ISSN 1745-2481. DOI: 10.1038/s41567-020-0825-9. Cit. on p. 101.

218 PARK, Jeong Min *et al.* Tunable Strongly Coupled Superconductivity in Magic-Angle Twisted Trilayer Graphene. **Nature**, Nature Publishing Group, v. 590, n. 7845, p. 249–255, 7845 Feb. 2021. ISSN 1476-4687. DOI: 10.1038/s41586-021-03192-0. Cit. on p. 101.

219 CAO, Yuan *et al.* Large Pauli Limit Violation and Reentrant Superconductivity in Magic-Angle Twisted Trilayer Graphene, 22 Mar. 2021. arXiv: 2103.12083 [cond-mat]. Cit. on p. 101.

220 BUKHARAEV, A. A.; ZVEZDIN, A. K.; PYATAKOV, A. P.; FETISOV, Y. K. Straintronics: A New Trend in Micro- and Nanoelectronics and Materials Science. **Physics-Uspekhi**, IOP Publishing, v. 61, n. 12, p. 1175, 1 Dec. 2018. ISSN 1063-7869. DOI: 10.3367/UFNe.2018.01.038279. Cit. on p. 101.

221 JIANG, Yuhang *et al.* Visualizing Strain-Induced Pseudomagnetic Fields in Graphene through an hBN Magnifying Glass. **Nano Letters**, American Chemical Society, v. 17, n. 5, p. 2839–2843, May 2017. ISSN 1530-6984. DOI: 10.1021/acs.nanolett.6b05228. Cit. on p. 101.

222 LOW, Tony; GUINEA, F. Strain-Induced Pseudomagnetic Field for Novel Graphene Electronics. **Nano Letters**, American Chemical Society, v. 10, n. 9, p. 3551–3554, Sept. 2010. ISSN 1530-6984. DOI: 10.1021/nl1018063. Cit. on p. 101.

223 PELTONEN, Teemu J.; HEIKKILÄ, Tero T. Flat-Band Superconductivity in Periodically Strained Graphene: Mean-Field and Berezinskii–Kosterlitz–Thouless Transition. **Journal of Physics: Condensed Matter**, IOP Publishing, v. 32, n. 36, p. 365603, June 2020. ISSN 0953-8984. DOI: 10.1088/1361-648X/ab8b9d. Cit. on p. 101.

224 BAO, Wenzhong *et al.* Controlled Ripple Texturing of Suspended Graphene and Ultrathin Graphite Membranes. **Nature Nanotechnology**, Nature Publishing Group, v. 4, n. 9, p. 562–566, 9 Sept. 2009. ISSN 1748-3395. DOI: 10.1038/nnano.2009.191. Cit. on p. 101.

225 CAI, S. *et al.* Periodic Patterns and Energy States of Buckled Films on Compliant Substrates. **Journal of the Mechanics and Physics of Solids**, v. 59, n. 5, p. 1094–1114, 1 May 2011. ISSN 0022-5096. DOI: 10.1016/j.jmps.2011.02.001. Cit. on p. 101.

226 CERDA, E.; MAHADEVAN, L. Geometry and Physics of Wrinkling. **Physical Review Letters**, American Physical Society, v. 90, n. 7, p. 074302, 19 Feb. 2003. DOI: 10.1103/PhysRevLett.90.074302. Cit. on p. 101.

227 LOPEZ-BEZANILLA, Alejandro; LADO, J. L. Electrical Band Flattening, Valley Flux, and Superconductivity in Twisted Trilayer Graphene. **Physical Review Research**, American Physical Society, v. 2, n. 3, p. 033357, 3 Sept. 2020. DOI: 10.1103/PhysRevResearch.2.033357. Cit. on p. 102.

228 VARJAS, Dániel; ROSDAHL, Tómas Ö; AKHMEROV, Anton R. Qsymm: Algorithmic Symmetry Finding and Symmetric Hamiltonian Generation. **New Journal of Physics**, IOP Publishing, v. 20, n. 9, p. 093026, Sept. 2018. ISSN 1367-2630. DOI: 10.1088/1367-2630/aadf67. Cit. on p. 103.

229 UNTYING the Insulating and Superconducting Orders in Magic-Angle Graphene | Nature. Cit. on p. 105.

230 PIZARRO, J. M. *et al.* Internal Screening and Dielectric Engineering in Magic-Angle Twisted Bilayer Graphene. **Physical Review B**, American Physical Society, v. 100, n. 16, p. 161102, 3 Oct. 2019. DOI: 10.1103/PhysRevB.100.161102. Cit. on p. 105.

231 RÖSNER, M.; LADO, J. L. Inducing a Many-Body Topological State of Matter through Coulomb-Engineered Local Interactions. **Physical Review Research**, American Physical Society, v. 3, n. 1, p. 013265, 19 Mar. 2021. DOI: 10.1103/PhysRevResearch.3.013265. Cit. on p. 105.

232 STEINKE, C.; WEHLING, T. O.; RÖSNER, M. Coulomb-Engineered Heterojunctions and Dynamical Screening in Transition Metal Dichalcogenide Monolayers. **Physical Review B**, American Physical Society, v. 102, n. 11, p. 115111, 8 Sept. 2020. DOI: 10.1103/PhysRevB.102.115111. Cit. on p. 105.

# Appendix

# APPENDIX A – Low-energy model at the antiferromagnetic quantum Hall/superconductor interface

## A.1 Gamma matrices

The Γ-matrices appearing in (7.2) are defined as:

$$\Gamma_0 := \tau_3 \otimes \rho_0 \otimes s_0 \otimes \sigma_0, \tag{A.1}$$
$$\Gamma_1 := \tau_3 \otimes \rho_0 \otimes s_1 \otimes \sigma_0, \tag{A.2}$$
$$\Gamma_2 := \tau_3 \otimes \rho_0 \otimes s_2 \otimes \sigma_0, \tag{A.3}$$
$$\Gamma_3 := \tau_0 \otimes \rho_3 \otimes s_3 \otimes \sigma_1, \tag{A.4}$$
$$\Gamma_4 := \tau_0 \otimes \rho_0 \otimes s_0 \otimes \sigma_3, \tag{A.5}$$
$$\Gamma_5 := \tau_1 \otimes \rho_0 \otimes s_0 \otimes \sigma_0, \tag{A.6}$$

where $\{\tau_\nu\}$ corresponds to electron-hole, $\{\rho_\nu\}$ to valley, $\{s_\nu\}$ to sublattice and $\{\sigma_\nu\}$ to spin degrees of freedom, respectively. The index $\nu = 0$ corresponds to the identity and $\nu = 1, 2, 3$, to the three Pauli matrices in the usual representation.

## A.2 Interface modes

The construction of a basis for the solutions of quantum Hall antiferromagnetic graphene/superconductor junctions outlined in section 7.2 leads to the following set of eigenspinors $\{\psi_{\kappa\eta}\}$, $\kappa, \eta = \pm$, in which the upper indices $<$ and $>$ indicate the regions $y < 0$ and $y > 0$, respectively. Here, to avoid cluttering, we introduce the functions:

$$\phi_1(B, m, y) = \frac{2me^{\frac{1}{2}y\sqrt{B^2y^2+4m^2}}}{\sqrt{By\left(By - \sqrt{B^2y^2+4m^2}\right) + 4m^2}}, \tag{A.7}$$
$$\phi_2(\Delta, \mu, y) = e^{-\Delta y}\sin(\mu y), \tag{A.8}$$
$$\phi_3(\Delta, \mu, y) = e^{-\Delta y}\cos(\mu y), \tag{A.9}$$

so that the eigenspinor basis can be written as

$$\psi^{<}_{++}(y) = \frac{1}{\mathcal{N}} \begin{pmatrix} 0 \\ 0 \\ 0 \\ 0 \\ 0 \\ \phi_1(B,m,y) \\ -\phi_1(B,m,y) \\ 0 \\ 0 \\ 0 \\ 0 \\ 0 \\ \phi_1(B,m,y) \\ 0 \\ 0 \\ \phi_1(B,m,y) \end{pmatrix}, \quad \psi^{>}_{++}(y) = \frac{1}{\mathcal{N}} \begin{pmatrix} 0 \\ 0 \\ 0 \\ 0 \\ -\phi_2(\Delta,\mu,y) \\ \phi_3(\Delta,\mu,y) \\ -\phi_3(\Delta,\mu,y) \\ -\phi_2(\Delta,\mu,y) \\ 0 \\ 0 \\ 0 \\ 0 \\ \phi_3(\Delta,\mu,y) \\ \phi_2(\Delta,\mu,y) \\ -\phi_2(\Delta,\mu,y) \\ \phi_3(\Delta,\mu,y) \end{pmatrix}, \tag{A.10}$$

$$\psi^{<}_{+-}(y) = \frac{1}{\mathcal{N}} \begin{pmatrix} 0 \\ 0 \\ 0 \\ 0 \\ \phi_1(B,m,y) \\ 0 \\ 0 \\ -\phi_1(B,m,y) \\ 0 \\ 0 \\ 0 \\ 0 \\ 0 \\ \phi_1(B,m,y) \\ \phi_1(B,m,y) \\ 0 \end{pmatrix}, \quad \psi^{>}_{+-}(y) = \frac{1}{\mathcal{N}} \begin{pmatrix} 0 \\ 0 \\ 0 \\ 0 \\ \phi_3(\Delta,\mu,y) \\ -\phi_2(\Delta,\mu,y) \\ -\phi_2(\Delta,\mu,y) \\ -\phi_3(\Delta,\mu,y) \\ 0 \\ 0 \\ 0 \\ 0 \\ \phi_2(\Delta,\mu,y) \\ \phi_3(\Delta,\mu,y) \\ \phi_3(\Delta,\mu,y) \\ -\phi_2(\Delta,\mu,y) \end{pmatrix}, \tag{A.11}$$

$$\psi^{<}_{-+}(y) = \frac{1}{\mathcal{N}} \begin{pmatrix} 0 \\ \phi_1(B,m,y) \\ \phi_1(B,m,y) \\ 0 \\ 0 \\ 0 \\ 0 \\ 0 \\ -\phi_1(B,m,y) \\ 0 \\ 0 \\ \phi_1(B,m,y) \\ 0 \\ 0 \\ 0 \\ 0 \end{pmatrix}, \quad \psi^{>}_{-+}(y) = \frac{1}{\mathcal{N}} \begin{pmatrix} \phi_2(\Delta,\mu,y) \\ \phi_3(\Delta,\mu,y) \\ \phi_3(\Delta,\mu,y) \\ -\phi_2(\Delta,\mu,y) \\ 0 \\ 0 \\ 0 \\ 0 \\ -\phi_3(\Delta,\mu,y) \\ \phi_2(\Delta,\mu,y) \\ \phi_2(\Delta,\mu,y) \\ \phi_3(\Delta,\mu,y) \\ 0 \\ 0 \\ 0 \\ 0 \end{pmatrix}, \tag{A.12}$$

$$\psi^{<}_{--}(y) = \frac{1}{\mathcal{N}} \begin{pmatrix} \phi_1(B,m,y) \\ 0 \\ 0 \\ \phi_1(B,m,y) \\ 0 \\ 0 \\ 0 \\ 0 \\ 0 \\ -\phi_1(B,m,y) \\ \phi_1(B,m,y) \\ 0 \\ 0 \\ 0 \\ 0 \\ 0 \end{pmatrix}, \quad \psi^{>}_{--}(y) = \frac{1}{\mathcal{N}} \begin{pmatrix} \phi_3(\Delta,\mu,y) \\ \phi_2(\Delta,\mu,y) \\ -\phi_2(\Delta,\mu,y) \\ \phi_3(\Delta,\mu,y) \\ 0 \\ 0 \\ 0 \\ 0 \\ \phi_2(\Delta,\mu,y) \\ -\phi_3(\Delta,\mu,y) \\ \phi_3(\Delta,\mu,y) \\ \phi_2(\Delta,\mu,y) \\ 0 \\ 0 \\ 0 \\ 0 \end{pmatrix}. \tag{A.13}$$

We end this appendix with some important observations regarding the spinor structure of the above basis. First, we note that in the QHAF region the well known identification of valley and sublattice degrees of freedom at the zeroth Landau level still holds, as well as the well defined spin polarization of these degrees of freedom.

Indeed, this suggests that $\kappa$ is related to valley polarization, whereas $\eta$ is related to the helicity of the modes. On the superconducting side, although both spin polarizations are present, they are described by orthogonal functions. Thus, exactly at the interface, corresponding to $\theta = \pi$, only the chiral propagating modes remain. Finally, the presence of superconductivity adds the charge-conjugation symmetry. So that by changing the canting angle, the chiral superconducting modes become gapped and the system can be regarded as an one-dimensional topological superconductor, as the effective Hamiltonian (7.15) suggests.

# APPENDIX B – Low-energy model at the quantum Hall/superconductor interface

To derive the low-energy effective model presented in Sec. 9.4, we start with the valley-symmetric Dirac-Bogoliubov-de Gennes Hamiltonian[58] for graphene. We consider an infinite system along the $y$-axis, for which the $x < 0$ region has a finite orbital magnetic field and $x > 0$ has a finite superconducting order parameter (this is the $k \cdot p$ version Eq. 9.2). Therefore, we have:

$$\begin{aligned} H &= \hbar v \tau_z \otimes [-i\rho_0\sigma_x\partial_x + (k\rho_0 + k_0\rho_z) \otimes \sigma_y] - \mu\tau_z \otimes \rho_0 \otimes \sigma_0 \\ &\quad + \tau_0 \otimes \rho_0 \otimes v\mathbf{A}(x) \cdot \sigma + \Delta(x)\tau_x \otimes \rho_0 \otimes \sigma_0, \qquad \text{(B.1)} \\ \mathbf{A}(x) &= (0, -Bx)\Theta(x) \ , \quad \Delta(x) = \Delta\Theta(x), \qquad \text{(B.2)} \end{aligned}$$

where the $\rho$, $\sigma$, and $\tau$ Pauli matrices act on valley, sublattice, and electron-hole spaces; $k$ is the momentum along the $y$-direction; $k_0$ is the Dirac nodes momentum for an arbitrary nanoribbon orientation; $\mathbf{A}$ is the gauge field; $\Delta$ is the superconducting order parameter; $\mu$ is the chemical potential; $v$ is the Fermi velocity; and $\Theta(x)$ is the Heaviside step function. We also simplify the problem by taking $\mu$ to be constant over the entire system.

We now compute the effective hamiltonian using first order in perturbation theory[43,44,102]. The perturbation is

$$H_{\text{pert}} = \hbar v \left(k\rho_0 + k_0\rho_z\right) \otimes \sigma_y, \qquad \text{(B.3)}$$

and the unperturbed term is

$$H_0 = H - H_{\text{pert}}. \qquad \text{(B.4)}$$

Thus, the effective hamiltonian is obtained by computing

$$(H_{\text{eff}})_{ij} := \langle\psi_i| H_{\text{pert}} |\psi_j\rangle \, , \qquad \text{(B.5)}$$

where $\{\psi_i\}$ are the zero-energy solutions of $H_0$.

In order to find $\{\psi_i\}$, we solve

$$\begin{aligned} \partial_x\psi &= m(x)\psi, \qquad \text{(B.6)} \\ m(x) &= \frac{i\Gamma_1^{-1}}{\hbar v} \left[eBx\Theta(x)\Gamma_4 + \mu\Gamma_0 - \Delta\Theta(x)\Gamma_3\right], \qquad \text{(B.7)} \end{aligned}$$

where we used Γ-matrices defined as:

$$\Gamma_0 := \tau_z \otimes \rho_0 \otimes \sigma_0, \tag{B.8}$$

$$\Gamma_1 := \tau_z \otimes \rho_0 \otimes \sigma_x, \tag{B.9}$$

$$\Gamma_2 := \tau_z \otimes \rho_0 \otimes \sigma_y, \tag{B.10}$$

$$\Gamma_3 := \tau_x \otimes \rho_0 \otimes \sigma_0, \tag{B.11}$$

$$\Gamma_4 := \tau_0 \otimes \rho_0 \otimes \sigma_y, \tag{B.12}$$

$$\Gamma_5 := \tau_z \otimes \rho_z \otimes \sigma_y; \tag{B.13}$$

and fixed the Landau gauge $A_x = 0$, $A_y = -Bx$. Thus,

$$\psi(x) = \psi_i(x) e^{\lambda_i(x)}, \tag{B.14}$$

where $\psi_\alpha(x)$ and $\lambda_\alpha(x)$ are the eigenvectors and eigenvalues of

$$M(x) = \int_0^x d\xi \; m(\xi). \tag{B.15}$$

We then have

$$\psi_i = \frac{1}{\mathcal{N}} \left( \psi_i^{x<0} \Theta(-x) + \psi_i^{x>0} \Theta(x) \right), \quad i = 1, 2, \tag{B.16}$$

where $\mathcal{N}$ is the normalization constant,

$$\psi_1^{x<0} = \begin{pmatrix} g(x) \\ i \\ 0 \\ 0 \\ ig(x) \\ 1 \\ 0 \\ 0 \end{pmatrix} \alpha(x) \;, \quad \psi_1^{x>0} = \begin{pmatrix} i \\ i \\ 0 \\ 0 \\ 1 \\ 1 \\ 0 \\ 0 \end{pmatrix} \beta(x), \tag{B.17}$$

and

$$\psi_2^{x<0} = \begin{pmatrix} 0 \\ 0 \\ g(x) \\ i \\ 0 \\ 0 \\ i \\ g(x) \end{pmatrix} \alpha(x) \;, \quad \psi_2^{x>0} = \begin{pmatrix} 0 \\ 0 \\ i \\ i \\ 0 \\ 0 \\ 1 \\ 1 \end{pmatrix} \beta(x), \tag{B.18}$$

with

$$g(x) = -\frac{2\mu x}{Bex^2 - 2\left(B^2e^2x^2/4 - \mu^2\right)^{1/2}|x|}, \tag{B.19}$$

$$\alpha(x) = e^{-\frac{\left(B^2e^2x^2/4-\mu^2\right)^{1/2}|x|}{\hbar v_F}}, \tag{B.20}$$

$$\beta(x) = e^{-\frac{x(\Delta - i\mu)}{\hbar v_F}}. \tag{B.21}$$

It is easy to see that $\psi_1$ is a linear combination of an electron state at the valley $K$ with a hole state at valley $K'$, while $\psi_2$ is the opposite. Using Eq. B.5, it is straightforward to obtain Eq. 9.8. Finally, the intervalley scattering term from Eq. 9.9 is obtained by adding $\omega\tau_0 \otimes \rho_x \otimes \sigma_0$ to Eq. B.3.

# APPENDIX C – List of publications

## C.1 Manuscripts related to the thesis

1. Antonio L. R. Manesco, G. Weber, and D. Rodrigues Jr., *Effective model for Majorana modes in graphene*, Phys. Rev. B **100**, 125411 (2019). **[Chapter 7]**

2. Antonio L. R. Manesco, G. Weber, and D. Rodrigues Jr., *Hidden chiral symmetries in BDI multichannel Kitaev chains*, J. Phys.: Condens. Matter **30** 175401 (2018). **[Chapter 8]**

3. Antonio L. R. Manesco, I. M. Flór, C.-X. Liu, and A. R. Akhmerov, *Mechanisms of Andreev reflection in quantum Hall graphene*, arXiv:2103.06722. **[Chapter 9]**

4. Antonio L. R. Manesco, J. L. Lado, Eduardo V. S. Ribeiro, G. Weber, and D. Rodrigues Jr., *Correlations in the elastic Landau level of spontaneously buckled graphene*, 2D Mater. **8** 015011 (2021). **[Chapter 10]**

5. Antonio L. R. Manesco, J. L. Lado, *Correlation-induced valley topology in buckled graphene superlattices*, arXiv:2104.00573. **[Chapter 11]**

## C.2 Other publications

1. B.S.de Lima, R.R.de Cassia, F.B.Santos, L.E.Correa, T.W.Grant, Antonio L. R. Manesco, G.W.Martins, L.T.F.Eleno, M.S.Torikachvili, A.J.S.Machado, *Properties and superconductivity in* Ti-*doped* $NiTe_2$ *single crystals*, Solid State Communications **283** (2018).

2. Antonio L. R. Manesco, G. Weber, and D. Rodrigues Jr., *One-Dimensional p-Wave Superconductor Toy-Model for Majorana Fermions in Multiband Semiconductor Nanowires*, IEEE Transactions on Applied Superconductivity **28**, 4 (2018).

3. A. Bhattacharyya, P. P. Ferreira, F. B. Santos, D. T. Adroja, J. S. Lord, L. E. Correa, A. J. S. Machado, Antonio L. R. Manesco, and L T. F. Eleno, *Two-band superconductivity with unconventional pairing symmetry in* $HfV_2Ga_4$, Phys. Rev. Research **2**, 022001(R) (2020).

4. P. P. Ferreira, A. L. R. Manesco, T. T. Dorini, L. E. Correa, G. Weber, A. J. S. Machado, and L. T. F. Eleno *Strain engineering the topological type-II Dirac semimetal* $NiTe_2$, Phys. Rev. B **103**, 125134 (2021).

5. Chun-Xiao Liu, Sergej Schuwalow, Yu Liu, Kostas Vilkelis, Antonio L. R. Manesco, P. Krogstrup, Michael Wimmer, *Electronic properties of* InAs/EuS/Al *hybrid nanowires*, arXiv:2011.06567.